FINAL REPORT

A Self-Sustaining Solar-Bio-Nano Based Wastewater Treatment System for Forward Operating Bases

SERDP Project ER-2215

JUNE 2017

Wei Liao
Ilsoon Lee
Abraham Engeda
Michigan State University

SERDP
DOD • EPA • DOE

Page Intentionally Left Blank

REPORT DOCUMENTATION PAGE

Form Approved
OMB No. 0704-0188

Public reporting burden for this collection of information is estimated to average 1 hour per response, including the time for reviewing instructions, searching existing data sources, gathering and maintaining the data needed, and completing and reviewing this collection of information. Send comments regarding this burden estimate or any other aspect of this collection of information, including suggestions for reducing this burden to Department of Defense, Washington Headquarters Services, Directorate for Information Operations and Reports (0704-0188), 1215 Jefferson Davis Highway, Suite 1204, Arlington, VA 22202-4302. Respondents should be aware that notwithstanding any other provision of law, no person shall be subject to any penalty for failing to comply with a collection of information if it does not display a currently valid OMB control number. **PLEASE DO NOT RETURN YOUR FORM TO THE ABOVE ADDRESS.**

1. REPORT DATE *(DD-MM-YYYY)* 06-21-2017	2. REPORT TYPE Final report	3. DATES COVERED *(From - To)* 2/2012-8/2017

4. TITLE AND SUBTITLE A self-sustaining solar-bio-nano based wastewater treatment system for forward operating bases	5a. CONTRACT NUMBER
	5b. GRANT NUMBER
	5c. PROGRAM ELEMENT NUMBER
6. AUTHOR(S) Wei Liao	5d. PROJECT NUMBER
	5e. TASK NUMBER
	5f. WORK UNIT NUMBER

7. PERFORMING ORGANIZATION NAME(S) AND ADDRESS(ES) 202 A.W. Farrall Hall 524 South Shaw lane, room 202 East Lansing, MI 48824	8. PERFORMING ORGANIZATION REPORT NUMBER

9. SPONSORING / MONITORING AGENCY NAME(S) AND ADDRESS(ES) Strategic Environmental Research and Development Program 4800 Mark Center Drive, Suite 17D03 Alexandria, VA 22350	10. SPONSOR/MONITOR'S ACRONYM(S) SERDP
	11. SPONSOR/MONITOR'S REPORT NUMBER(S) ER-2215

12. DISTRIBUTION / AVAILABILITY STATEMENT

Unlimited

13. SUPPLEMENTARY NOTES

14. ABSTRACT
The goal of this project was to integrate solar, biological, and nano technologies into wastewater treatment concept to create a novel small-scale wastewater treatment system that can significantly reduce mass of the wastewater, and simultaneously generate potable water for FOBs. Combining solar energy collection and biological methane generation provides sufficient and stable energy for small size wastewater treatment operations (fixed film anaerobic digestion, water reclamation, and nano-filtration of water purification), and overcomes the disadvantages of individual technologies such as unsteady energy flow for solar power generation, low efficiency of conventional anaerobic digestion, and higher energy requirement of water purification.

15. SUBJECT TERMS

16. SECURITY CLASSIFICATION OF:			17. LIMITATION OF ABSTRACT	18. NUMBER OF PAGES	19a. NAME OF RESPONSIBLE PERSON
a. REPORT UU	b. ABSTRACT UU	c. THIS PAGE UU	UU	128	19b. TELEPHONE NUMBER *(include area code)*

Standard Form 298 (Rev. 8-98)
Prescribed by ANSI Std. Z39.18

Page Intentionally Left Blank

Page Intentionally Left Blank

Contents

Abstract

Objectives:

The wastewater treatment is a critical but expensive component for forward operating bases (FOBs). Development of a self-sustaining wastewater treatment is urgently needed to sustain the FOBs. The goal of this project was to integrate solar, biological, and membrane technologies into wastewater treatment concept to create an energy-neutral small-scale wastewater treatment system that can significantly reduce mass of the wastewater, and simultaneously generate portable water for FOBs. The studied system includes four unit operations: solar energy generation, anaerobic digestion, electrocoagulation, and membrane filtration. Six specific objectives were carried out to develop the system: 1) designing a new solar-bio-hybrid power generation unit; 2) optimizing lab-scale upflow fixed-film anaerobic digestion on blackwater and food wastes; 3) studying electrocoagulation to reclaim the water; 4) investigating nano-filtration on potable water generation from the EC solution; 5) establishing a pilot scale, self-sustaining system and evaluating its performance; and 6) conducting a detailed technical and economic analysis on the system.

Technical approach:

Individual units in the integrated system was first investigated at bench scale to obtain the parameters for the system design and integration. Solar thermal and solar electricity approaches were studied to combine with methane from AD to power the entire system. An upflow fixed-film anaerobic digestion system was studied and designed to improve the efficiency of blackwater and food waste treatment in terms of reducing the footprint of digester, enhancing solid reduction, improving biogas production, and removing pathogens. The methane gas from the digester was studied to be used as a biochemical storage of solar energy to compensate unsteady solar heat and generate more energy. Electrocoagulation as a simple, efficient electric-chemical process was then studied to post-treat the effluent from the digester and reclaim the water. The electrocoagulation was designed to accommodate availability and amount of on-site energy sources (solar and methane energy) as well as the wastewater quality and quantity. A study of developing an anti-fouling nano-filtration was then conducted to turn the reclaimed water into potable water. Built up on the research outcomes from the studies on individual unit operations, a pilot scale system was then fabricated. Consequently, the system performance was evaluated and the detailed technical and economic analysis were conducted.

Results:

Two new solar thermal receivers using Fresnel lens as the collector of solar irradiation were concluded to be used to convert solar energy into high-quality thermal energy that is combined with biogas energy to efficiently and stably provide the required energy and power the treatment system. A high-efficiency upflow fixed-film digestion was developed to handle mixture of blackwater and food wastes, which had the methane productivity of 414 L/kg TS loading and the TS reduction of 71%. The EC unit can remove approximately 99% of the TS in the AD effluent, and remove the majority of total coliform. The combination of nano-filtration and reverse-osmosis filtration further turned the reclaimed water into clean water for potable uses. The technical and economic analysis further concluded that combining solar energy collection and biological methane generation provides sufficient and stable energy for small size wastewater treatment operations (fixed film anaerobic digestion, water reclamation, and nano-filtration of water purification), and overcomes the disadvantages of individual technologies such

as unsteady energy flow for solar power generation, low efficiency of conventional anaerobic digestion, and higher energy requirement of water purification.

Benefits:

The research outcomes of this project clearly demonstrated a self-sustaining system that is not only a waste management tool but also an on-site renewable energy generation unit. Essentially, the technology developed by this project will advance military bases for their waste treatment and energy utilization, and significantly improve the sustainability of all FOBs, if fully deployed. In addition, the integrated solar-bio-nano concept also has a great potential to be applied by a wide range of waste treatment systems from agricultural wastewater to municipal wastewater treatment. The use of such novel technology will dramatically change the status of wastewater treatment. It will eventually turn the wastewater from an environmental liability into a public and private asset.

1. OBJECTIVES

The wastewater treatment is a critical but expensive component for forward operating bases (FOBs). Development of a self-sustained and scalable wastewater treatment system is urgently needed to sustain the FOBs. This project integrated solar, biological, and nano technologies and created a novel self-sustainable and scalable wastewater management system that can significantly reduce the mass of wastewater, and simultaneously generate portable water for FOBs (Figure 1). The studied system includes four unit operations of solar-bio-hybrid energy generation, upflow fixed film anaerobic digestion, electrocoagulation of water reclamation, and nano-facilitated filtration. Combining solar energy collection and biological methane generation provides sufficient and stable energy for wastewater treatment operations (anaerobic digestion, electrocoagulation, and nano-facilitated filtration), and overcome the disadvantages of individual technologies such as unsteady energy flow for solar power generation, low conversion efficiency of mesophilic anaerobic digestion, and higher energy requirement of anaerobic/aerobic treatments and water purification. The integrated system creates a scalable and environmental-/energy-sound solution to treat blackwater and food wastes at FOBs.
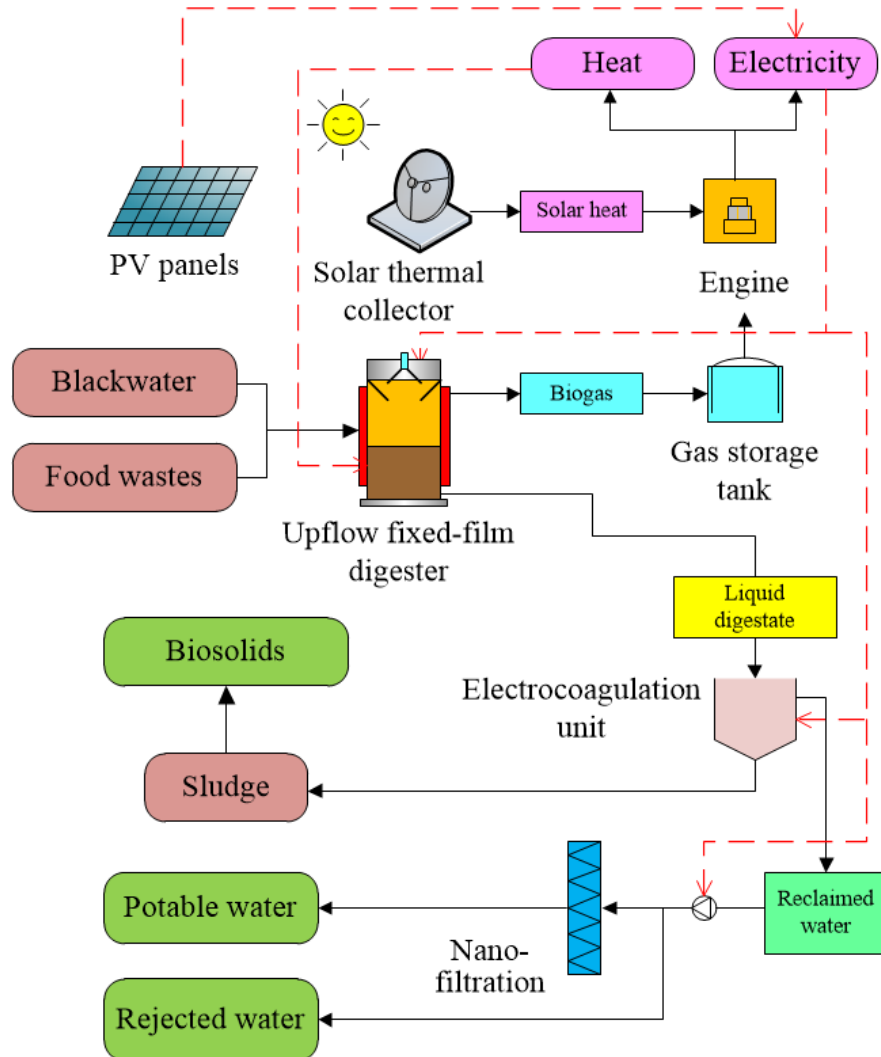

Figure 1. Self-sustaining solar-bio-nano based waste treatment system

1

Six specific objectives were correspondingly carried out: 1) designing a novel solar-bio-hybrid power generation unit on solar and methane energy; 2) investigating Upflow fixed film digestion on mixed blackwater and food wastes; 3) studying electrocoagulation to reclaim water; 4) investigate the nano-filtration on portable water generation; 5) establish a small pilot-scale system and evaluate performance of the integrated system; and 6) conduct a detailed technical and economic analysis on the system and devise strategies toward market transition. The studied concept first uses the solar-bio-hybrid power generation unit to convert solar and methane energy into electricity and heat. The electricity is used to power pumps, grinder, centrifuge, and control panel in the integrated system to satisfy operational requirements. The heat is mainly used to maintain the temperature of the anaerobic digester to produce methane gas and reduce total solids. The high efficient upflow fixed film digestion significantly reduces the footprint of the integrated system. In addition, anaerobic digester also plays an important role of storing solar energy (heat) into a high heating value and steady-flow biochemical energy source – methane. A methane biogas storage tank serves as the fuel storage to compensate unsteady solar heat and generate more energy. The liquid effluent from the digester is treated by a novel electrocoagulation process to simultaneously clean up the bigas, and remove residual organic compounds to prepare reclaimed water for the filtration. An anti-fouling nano-filtration unit then converts the reclaimed water into potable water. The proposed research effort addresses all five requirements in the Statement of Need (SON) of this solicitation, and fits well with the SERDP goals as it will significantly reduce the process costs and environmental risks, and sustain military operations.

2. BACKGROUND

Water is one of most important sustainment commodities on the battlefield. It has been reported that the largest shipment of supplies to military bases oversea has been to deliver water [1]. Fourteen trucks are needed to deliver bottle waters to a battalion-sized FOB (approximately 600 soldiers) on a weekly basis [2]. It costs up to $50 per gallon water used at FOBs, most of the cost is attributed to secure the transportation [2]. It has been estimated that around 35 gallon water per soldier per day including drinking water and non-portable water are consumed [2], and the same amount of wastewater are generated. The wastewater management strategies are varied according to FOB size, general operational standards, contractor services, and location. The methods currently used by FOBs are burn-out latrines, chemical latrines, sewerage lagoons, septic system and leach fields etc. [2]. The treatment of the wastewater is a significant burden to all of FOBs. Thus, developing energy-neutral on-site wastewater treatment solutions to reuse the water is a key to sustain the FOBs.

Anaerobic digestion (AD) is an existing natural and biological conversion process that has been proven effective on converting wet organic wastes into biogas capable of producing clean electricity while also alleviating many of the environmental concerns associated with the wastes. There is a wide variety of digestion configurations for treatment of different waste streams, such as plug-flow reactor for high solid concentration streams (animal manure), Continuous Stirred Tank Reactor (CSTR) for municipal sludge, and Upflow Anaerobic Sludge Blanket (UASB) reactor for food wastes etc. Among these digestion configurations, UASB is the preferred method that is able to handle dilute wastewater streams in an energy positive manner. UASB has unique features of less sludge production, more robustness (resistant to toxic compounds such as xenophobic and recalcitrant compounds), less operation and maintenance requirement, small space requirements, efficient Chemical Oxygen Demand (COD)/Biological Oxygen Demand (BOD) reduction, and potential electricity/heat generation [3-5]. Thus, considering the nature of wastewater available on the FOBs (less solid content, relatively low COD and high BOD) and the operational requirements of FOBs (scalable, efficient, and easy to use), UASB is one of the best fits for this particular case. However, due to the fast feeding rate, one of disadvantages of UASB digestion, particularly for small systems, is that more energy is required for heating influent and maintaining reactor temperature. It leads to a negative energy balance. Therefore, a secondary energy source is needed to power the UASB digestion. Solar energy, as one of most abundant renewable energy sources available on-site FOBs, can be an excellent candidate to be combined with the digestion operation.

Several solar conversion technologies to generate electricity and heat have been developed in the past several decades, such as, photovoltaics, flat panel/evacuated-tube solar thermal collector, parabolic trough system, power tower system, dish solar system, and Fresnel reflector etc. [6]. Among them, flat panel/evacuated-tube solar thermal collector has been studied to combine with anaerobic digester to provide energy for wastewater treatment [7-11]. However, since the evacuated-tube solar thermal collector is not a concentrating solar collector, it is only capable of providing low concentration energy (up to 150°C), and the use of such energy is correspondingly limited to heating the digesters. Other solar conversion technologies have not been systematically explored on the combination with anaerobic treatment of wastewater streams to date. Integrating advanced solar power and AD systems leads to a novel wastewater treatment concept that not only is suitable for the scalable military operations such as FOBs, but also changes wastewater treatment operations at large from conventional sole wastewater treatment

systems to the future dual wastewater utilization/energy generation systems. In addition, anaerobic digestion in the combined solar-AD system has another important function that biogas generated from AD could serve as a biochemical thermal sink to store solar energy. Thus, in order to fully take advantages of both solar and biogas energy, a solar-bio hybrid energy conversion system was studied by this project to integrated concentrated solar collection and PV panels with anaerobic digestion to generate electricity and heat for the wastewater treatment.

In spite of advantages of combination of solar energy collection and AD to generate energy and treat wastewater, the effluent from the AD still has relatively high levels of BOD, COD, and nutrients (nitrogen and phosphorus). It needs to be further treated in order to generate potable water. Physical and chemical methods such as sedimentation, flocculation, coagulation, ozone, and activated carbon etc. followed by reverse osmosis (RO) are often used to reclaim water from the effluent [12, 13]. However, additional chemicals and less efficiency of these methods prevent them from adoption by FOBs at large. Compared to those conventional physical and chemical treatment methods, electrocoagulation (EC) technology, with advantages of shorter retention time, better removal of smaller particles, without the addition of coagulation-inducing reagents, and minimum secondary chemical contamination [14], represents a superior process to reclaim water from various organic waste streams. EC technology applies direct current electrolytic process and the flocculent separation to coagulate, precipitate, and float solids and pollutants. Metal electrodes in EC unit are made of iron or aluminum or other metals [15]. During the electrocoagulation reaction, current destabilizes electrostatically suspended solids that further react with cationic species from the anode metal to form precipitated or floated metal oxides and hydroxides [15]. EC technology has been used to treat AD effluent and other wastewater. It has been reported that EC process has very high efficiency to remove total solids, turbidity, and COD [16]. Bellebia et al demonstrated that EC can remove up to 75% and 99% of COD and turbidity, respectively, from paper mill effluent [17]. Mollah et al presented a 80% removal of total solids from slaughterhouse wastewater using EC [18]. Factors such as current density, retention time, initial pH, electrode distance, salt concentration, and electrode type have significant influences on EC performance. Among them, pH is the most important one [19-21]. pH during the EC process is gradually increased due to the increase of hydroxyl ions from cathodes. It has been reported that high pH is disadvantageous in solids and nutrients removal during EC [22, 23]. Controlling pH during EC process could be a simple and effective way to enhance the separation performance and improve energy efficiency. On the other hand, biogas from AD contains several by-products such as H_2S and CO_2 besides the main compound of methane [24]. The existence of these by-products adversely influences biogas utilization for electricity generation since some of they are corrosive to engines and combustors. H_2S is one of the most corrosive compounds in the biogas, which is converted into SO_2 and H_2SO_4 damaging gas-handling equipment during the biogas combustion. Many efforts have been made to remove H_2S and other by-products from biogas. Ethylenediaminetetraacetic acid (EDTA) coupled Fe^{3+} solution has been used to adsorb H_2S in biogas [25]. Metal ions such as Cu^{2+}, Zn^{2+} and Fe^{3+} were applied to precipitate sulfate-based compounds [26]. Activated carbon was studied to absorb H_2S in biogas [27-29]. Other chemical abatement and biological absorption have also been reported as effective methods to remove H_2S [30-33]. However, most of these approaches either require additional chemicals or need complicated systems to support, which make it economically and environmentally difficult to implement them. Considering both facts of biogas with relatively high H_2S content and EC treated AD effluent with high pH and metal ion level, mixing these two streams could facilitate EC treatment of AD effluent and simultaneously clean up biogas.

The reclaimed water from aerobic treatment needs to be further treated to remove remained microbes and impurities (such as P, N, and Na/K ions) to generate the potable water. Membrane technology has been widely applied to purify water. However, the filtration efficiency and membrane fouling are the main obstacles that the current membrane technologies encounter. Recent advances in nanotechnology have demonstrated that nanomaterials can significantly improve the membrane performance on generating portable water from reclaimed water [34-36]. Therefore, combining high rate aerobic clarification and nano-filtration technology provides a new route to design scalable and efficient processes to remove organic and inorganic compounds in the effluent for portable water production.

The newly developed nanomaterials and nanotechnology tools enable the synthesis of novel polymers and ceramics, as well as polymer-inorganic composites to manufacture higher performance membranes with increased permeability, selectivity, and resistance to fouling. A variety of different functional nanoparticles such as silver nanoparticles and bimetallic nanoparticles of Fe/Ni, Fe/Pb, and zero-valent iron have been investigated [37-44]. Fe/Ni and Fe/Pb biometallic nanoparticles have been incorporated into polymer-inorganic porous composite membranes and applied to the reductive degradation of halogenated organic solvents [40, 41]. Cui et al. demonstrated the silver nanowire based membrane along with carbon nanotubes and cotton has the capability of high speed electric sterilization of water [43]. However, one of key issues of using nano-membrane to purify the portable water is the unanticipated health effect by some nanomaterials such as nanotube and nano-metals. The toxic potential of engineered nanomaterials for human health and the environment has to be considered. Thus, this project will only use proved environmentally friendly nano-materials such as nano graphite to fulfill the design and fabrication of the proposed nano-filtration system.

Self-cleaning or fouling mitigation is another challenge for membrane application in water purification systems. It has been reported that TiO_2 nanoparticles assembled on polymeric membrane surface not only enhanced the pollutant degradation on the nano-membrane but also improved the antifouling properties of the membrane [37, 45]. In addition, the fouling mitigation of nano-membranes can also be ameliorated by combining nanoparticles with other chemical/physical processes such as ozonation [46, 47], rotating filtration [48], and intermittent electric field pulses [49, 50]. Karnik et al. presented that ozonation of a lake water prior to filtration of nano-membrane maintained 95% of filtration permeate flux more than 16 hours compared to 2 hours without ozonation [47], which indicated that the ozonation significantly facilitated the removal of organic foulants on the membrane surface. The ozonation has advantages of eliminating odors, producing no toxic side products, and increasing suspended organic matter reduction, though, corrosive effects on steel and some oxidized polymers, and high energy consumption are the barriers to apply this technology on small-scale systems. Rotating filtration system as another anti-fouling technology has been developed as part of the life supporting system for space stations [48]. Lueptow et al. has reported a rotating RO unit (using centrifugal force to remove deposits on the membrane) that has a higher portable water recovery of 90% compared to 25% for typical vortex flow RO systems [51], while the rotating reverse osmosis system needs a complicated mechanic structure to support the rotation, and still has the fouling problem and requires a relatively high operational pressure (more than 500 psi) [52]. It has also been reported that pulsed electric discharge as a Physical Water Treatment (PWT) method can effectively remove deposits from the filter membrane [49, 50]. For instance, a plasma discharge was applied on a membrane to treat calcium and sodium ion rich wastewater, the pressure drop can be reduced to the initial value at the clean state of the membrane, and the

life span of the membrane filter was significantly extended [49]. However, high-energy consumption for the pulsed electric discharge limited wide applications of such technology. Considering the operational conditions of FOBs and the requirement of a self-cleaning and anti-fouling scalable filtration system, combining pulsed electric discharge with either rotating or vortex flow nano-membrane filtration could be a solution for FOBs to enhance filtration efficiency, extend membrane life, and reduce energy consumption. Therefore, the effects of vortex flow and centrifugal force (rotating filter) on electrically discharged nano-membrane will be investigated by this project, and consequently a novel RO unit using safe and environmental friendly nano-materials will be developed to efficiently remove organic and inorganic impurities and produce potable water on-site of FOBs.

3. MATERIALS AND METHODS
3.1 Designing a novel solar-bio-hybrid power generation unit on solar and methane energy
3.1.1 Designing and implementing a foldable solar heat collector
3.1.1.1 Design of a bench-scale foldable Fresnel solar thermal collector
### 3.1.1.1.1 Foldable collector structure

A bench-scale two-module foldable Fresnel solar thermal collector has been designed and constructed to carry out the study (Figure 2c). A supportive platform is fixed on the bench (⑨ in Figure 2a &b) to support the thermal collector, which is slowly moved according to the topocentric azimuth angle (measure from the north vector, clockwise). In order to fold the collector, two mechanical actuators (model TB055 PBC Linear Co. Roscoe, IL) are used to move the lens, which are horizontally and vertically positioned on the platform (⑤ and ⑥ in Figure 2 a &b). Two rotary pivots with screw pins (for locking purpose) are installed, one is located at the joint of vertical and horizontal actuators, and the other is at the joint of the receiver holder and the supportive platform (Figure 2b). During the operation of solar thermal collection (Figure 2 a&c), a Fresnel lens (50 grooves per inch, diameter of 18.25 inches, focal length of 24 inches, index of refraction of 1.49, transmittance of 0.92) is placed in the carriage of the vertical actuator (⑥ in Figure 2 a&b). The lens rotates according to the zenith angle (measured from vertical direction opposite to the apparent gravitational force). The receiver is fixed on the supportive platform.

(a)   (b)
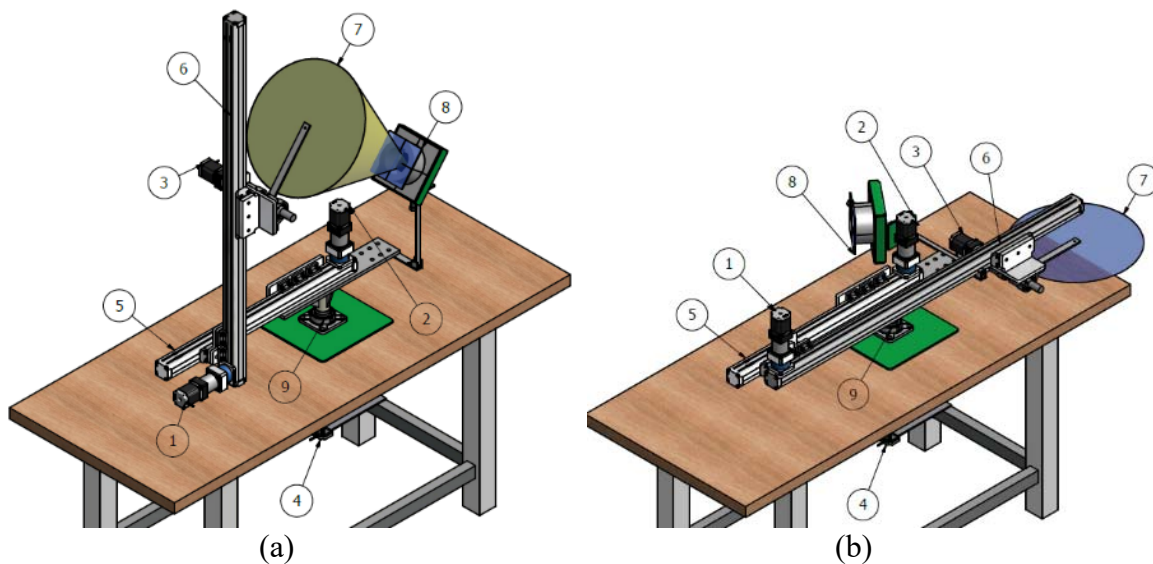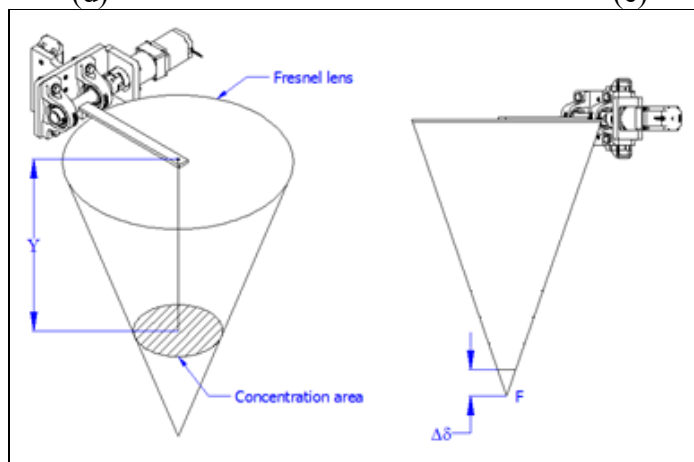
(c)
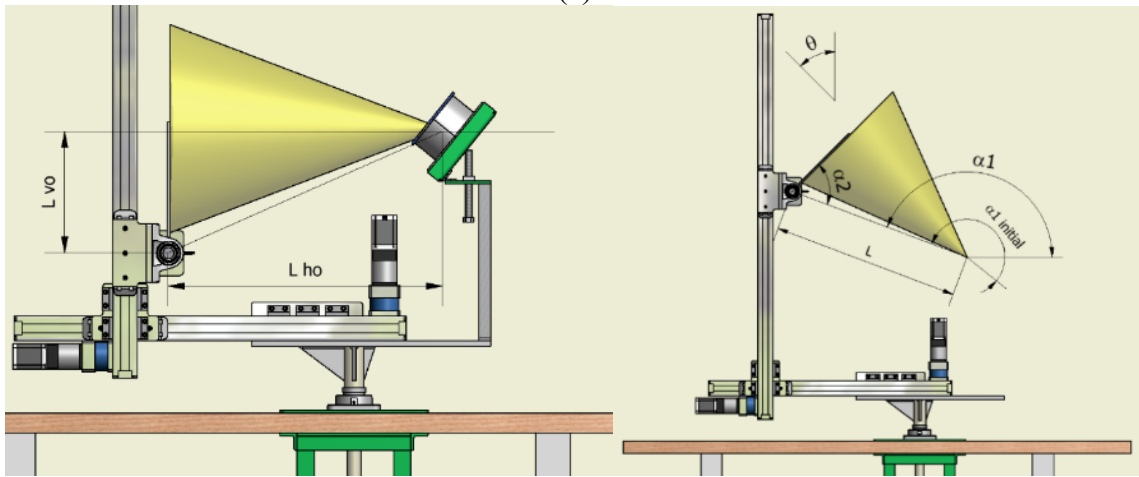
(d)

(e)

(f)

Figure 2. Bench-scale two-module foldable Fresnel solar thermal collector*

(a). CAD drawing of the solar thermal collector in working mode; (b). CAD drawing of the solar thermal collector in folding mode; (c). The bench-scale solar thermal collector; (d) Initial positon of the solar thermal collector; (e) Zenith angle and lens adjustment at mid-position; (f) Concentration ratio for temperature measurement.

 *: ① Stepper motor for vertical adjustment of the lens (gearbox 15:1); ② Stepper motor for horizontal adjustment of the lens (gearbox 15:1); ③Stepper motor for zenith angle adjustment (gearbox 70:1); ④ Stepper motor for azimuth angle adjustment (gearbox 70:1); ⑤ Horizontal linear actuator (700 mm stroke); ⑥ Foldable vertical linear actuator (1280 mm stroke); ⑦ Fresnel lens (24 in focal length); ⑧ Receiver for solar radiation; ⑨ Supportive platform.

In order to align the lens towards sun and maintain the fixed focal distance between the Fresnel lens and receiver, three automatic movements are required: 1) the lens rotated according to the zenith angle; 2) the platform rotated according to azimuth angle; and 3) horizontal and vertical displacement movements to align the focal point into the heating surface (circular movement around the receiver). These movements are achieved by actuators and gearboxes. The actuators used for the solar collector unit have a position accuracy of less than 0.05 mm between repeated movements. The gearboxes with 15:1 ratio (23VL015 NEMA 23 Planetary Gearhead) are used to adjust horizontal and vertical displacement movements. The gearboxes with 70:1 ratio (23VL070 NEMA 23 Planetary Gearhead) are for lens rotation and platform rotation. The resolutions are 0.00885 mm/step and 0.025 degree/step for linear displacement and rotation, respectively. In this particular study, steel plates are used as the thermal absorbers. Considering the shape and size of the steel plates, the receiver holder has to be adjusted to be paralleled with the lens. This movement is manually achieved. A nut-screw is installed on the receiver holder to adjust inclination of the receiver (10° to 75° respect to the horizontal level) and make it parallel with the lens (⑧ in Figure 2 a&b). A protractor (Empire polycast magnetic protractor, model #36) with a resolution of 1° is used to measure the angle. The receiver inclination is adjusted each two minutes.

3.1.1.1.2 Thermal absorbers for temperature profile at the focal area

In order to conclude temperature profile at the focal area of the collector unit, a thermal receiver was specially designed to collect solar radiation for this study (Figure 3). The receiver includes a metallic cylindrical column (65mm high and 92 mm diameter), a square thermal glass (size of 158x158 mm, thickness of 6.35mm, transmittance of 0.9) covering the top of the column (Figure 3a). Three layers (10 mm each) of Pyrogel XT (an insulation material with the thermal conductivity of 90 mW·m^{-1}·K^{-1} at 650 °C) are placed at the bottom of the column. The absorbers are fixed on the top of the Pyrogel XT layers. The absorbers are mild steel plates with different sizes (63.5x63.5 mm (2.5x2.5 in), 50.8x50.8 mm (2x2 in), and 38.1x38.1 mm (1.5x1.5 in) (Figure 3c). In addition, two layers of Pyrogel XT are used to cover the side of the metallic column to prevent excess heat loss.
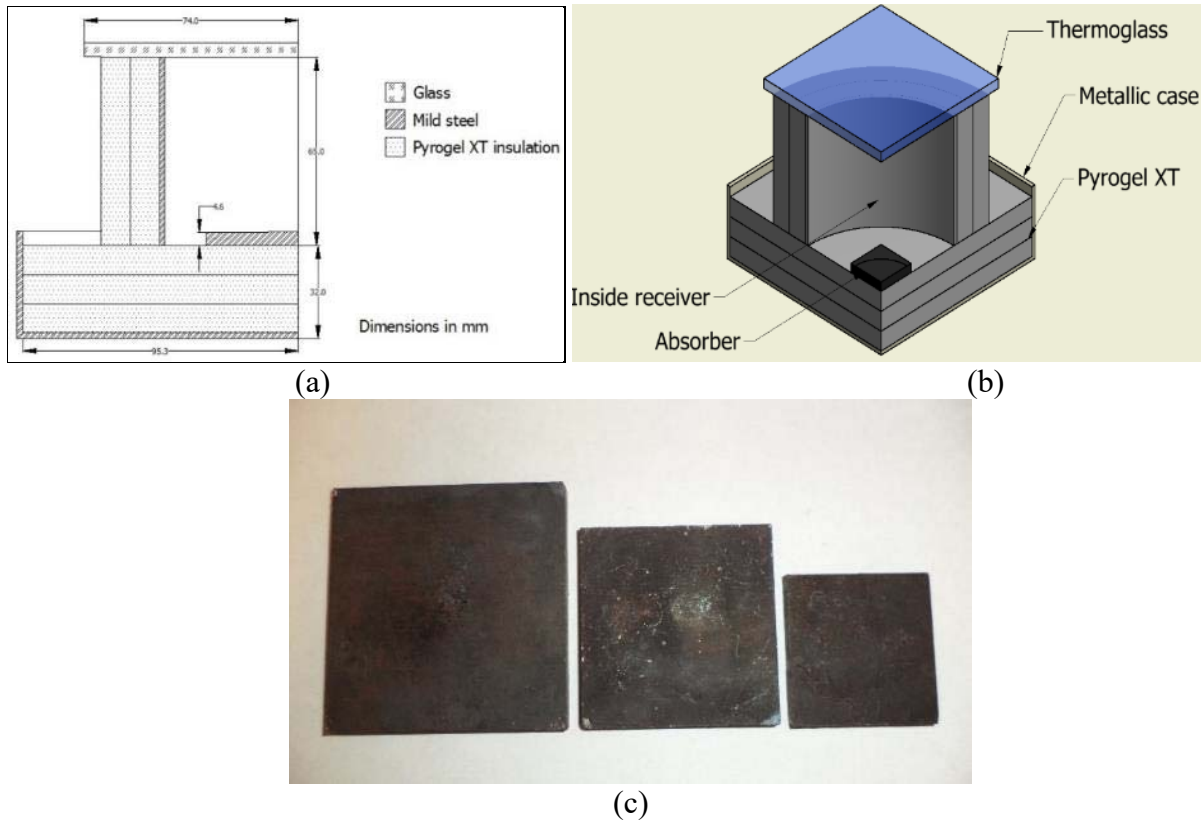
(a)

(b)

(c)

Figure 3. The receiver and metallic absorbers
(a). Dimensions of the receiver (quarter size); (b). Geometric model of the receiver (one-quarter size); (c). Metallic absorbers with three different sizes (2.5x2.5 in, 2x2 in, and 1.5x1.5 in)

3.1.1.1.3 Instruments for solar tracking

Four stepper motors (NEMA 23, 20000 steps per revolution in increments of 100 steps, 24 VDC) are implemented to control linear displacement and rotation of the Fresnel lens collector. The stepper motors are powered by four power supplies (model PS150A24, input 120 VAC, output 24 VDC, 150 W) via the drives (model ST5-Si-NN) that have been programed using the software Si Programmer™ (Figure 4). The stepper motors are connected to the drives using bipolar parallel connection. A hub (model SiNet-Hub 444) transmits the control signals to

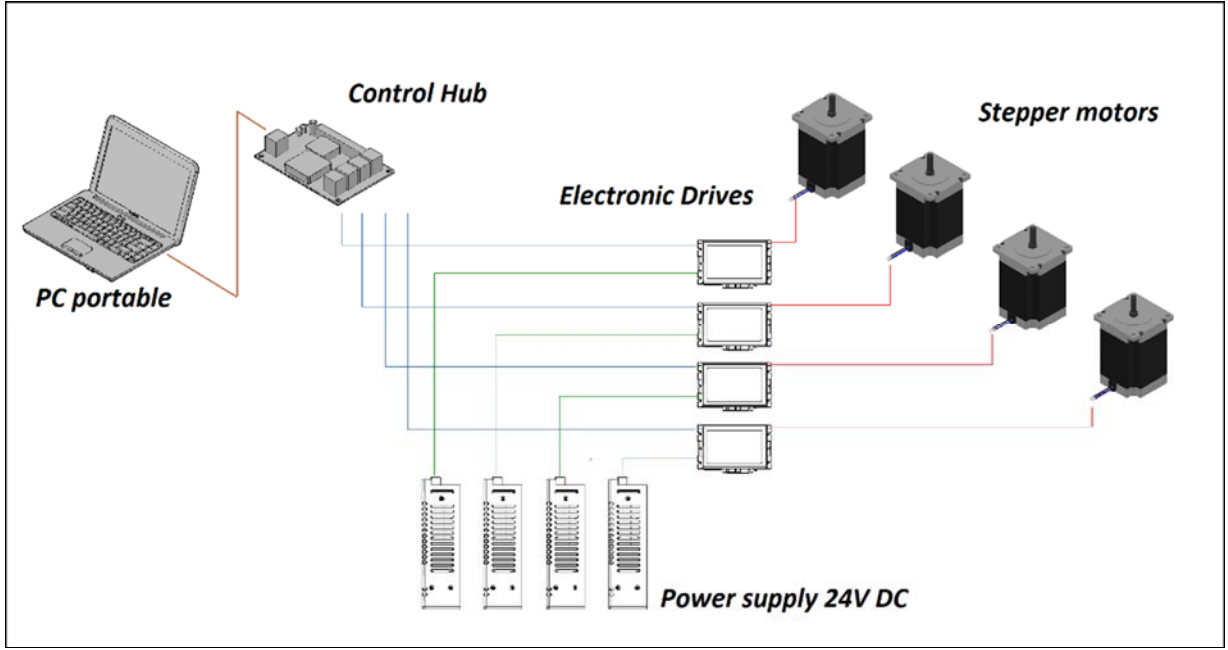the drives via RJ 11 connection. A RJ11-RS232 connector is used to connect the control hub to a computer.

Figure 4. Hardware for the control system

3.1.1.2 Solar tracking model and control mechanism

An astronomical algorithm [53] was programed in Matlab® 2011a (MathWorks, Natick, MA) to calculate the position of the Sun (the code of the Matlab® function is in the supplemental material). LabVIEW 2011 (National Instruments Co, Austin, TX) was used to run the Matlab® function to track the position of the Sun, and also control the stepper motors to move the Fresnel lens solar thermal collector (Figure 5). A virtual clock provides time parameters to the algorithm (processes 1, 2 and 3 in Fig. 4).

The displacement of linear actuators is calculated based on the following equations in the Matlab® function.

$$L_h = L_{h0} - L \cdot \cos\left(\alpha^o_1 - \frac{\pi}{2} + \theta \right) \tag{1}$$

$$L_v = L_{v0} - L \cdot \sin\left(\alpha^o_1 - \frac{\pi}{2} + \theta \right) \tag{2}$$

Where L_h and L_v are the horizontal and vertical displacement of the lens (mm), L_{h0} and L_{v0} are the horizontal and vertical distance from the focal point to the rotational point of the lens in the initial position (mm), L is the distance between the focal point and the rotational point of the lens, α^o_1 is the angle for the location of L in the initial position (rad), and θ is the topocentric zenith angle for sun's position (rad) (Figure 2 d&e).

The displacement and rotation of the lens are then converted to steps by the LabVIEW using the following equations to control the movement of the stepper motors 1-2 and 3-4 (corresponding gearboxes have ratios of 1:15 and 1:70, respectively) (Figure 5).

$$S_h = L_h \cdot \frac{1}{R} \cdot \frac{15}{1} \cdot \frac{20\,000}{1} \qquad\qquad S_v = L_v \cdot \frac{1}{R} \cdot \frac{15}{1} \cdot \frac{20\,000}{1} \tag{3}$$

11

$$S_\theta = (\theta - \theta_o) \cdot \frac{1}{360} \cdot \frac{70}{1} \cdot \frac{20\,000}{1} \qquad\qquad S_\gamma = (\gamma - \gamma_o) \cdot \frac{1}{360} \cdot \frac{70}{1} \cdot \frac{20\,000}{1} \qquad (4)$$

Where S_h and S_v are the number of steps for the motors 1 and 2 (for the horizontal and vertical adjustment, respectively), R is the linear displacement per actuator-shaft revolution (0.04 rev/mm), S_θ and S_γ are the number of steps for motors 3 and 4 (for the zenith and azimuth adjustment, respectively), θ_o and γ_o are topocentric angles for the initial position ($\theta_o = 90°$, $\gamma_o = 0°$), θ and γ are the zenith and azimuth angles for the position of the Sun.

The speed of the stepper motors is set at 5 rev/second. According to the sun position in East Lansing, MI, a filter code is included to limit the movement range of the step motors 3 and 4, so that the movements of azimuth and zenith angles are 90° to 270° and 0° to 90°, respectively (process 4 in Figure 5).

During the operation, the sequence of actions is set up as: azimuth angle rotation, horizontal displacement, vertical displacement, zenith angle rotation, and receiver inclination adjustment. SCL language is used to send commands to the motors. Acceleration and deceleration of the movements are set 25 rev·s⁻². A delay of 1.5 seconds between the motor movement commands is included to avoid data saturation in the control hub. The continuous loop (Figure 5) is repeated each 60 seconds. The labVIEW codes for the two axis solar tracking system are provided in the supplemental material.
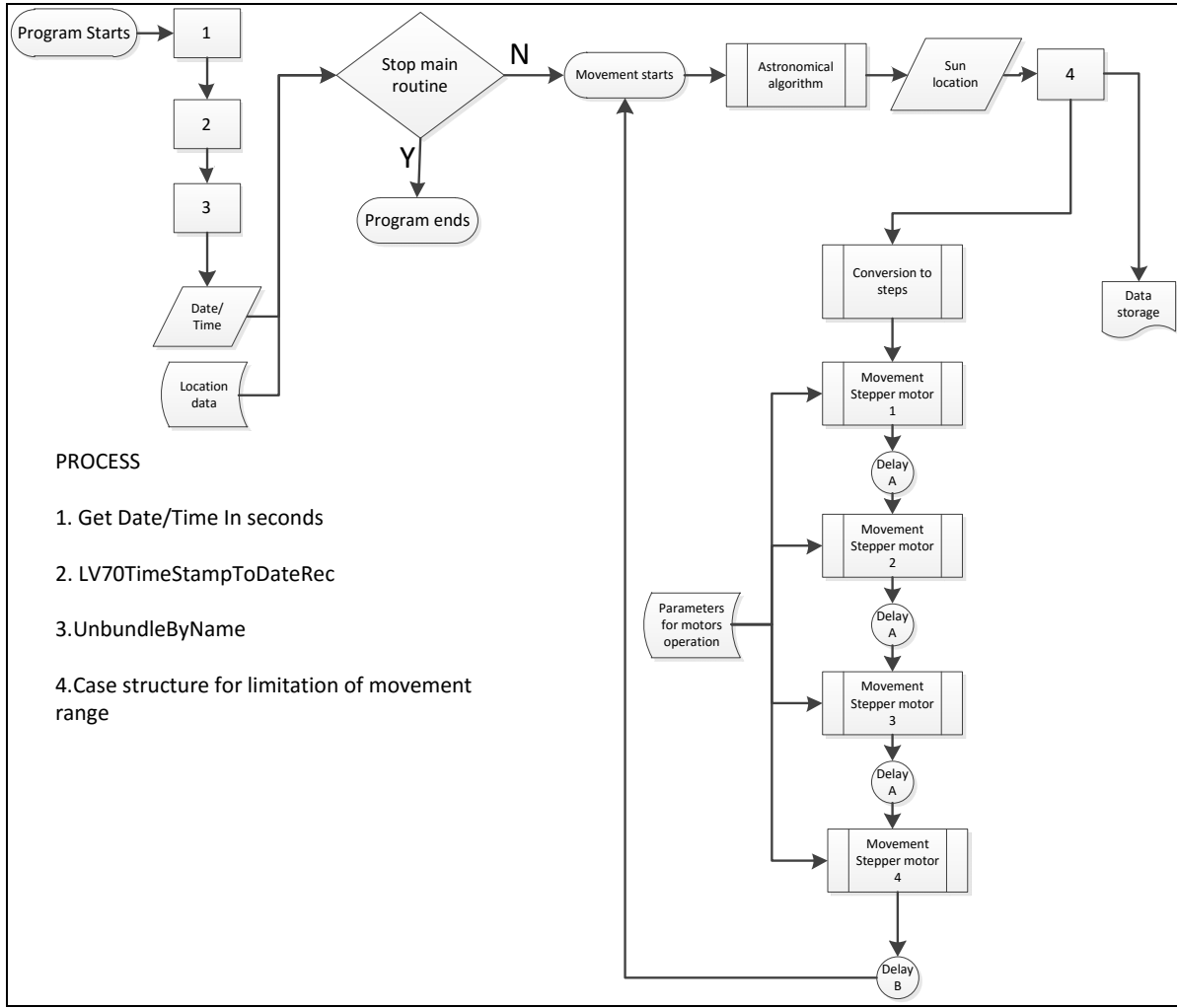
Figure 5. Flowchart for tracking control using LabVIEW

3.1.1.3 FEM simulation of temperature profiles of the receiver

The temperature distribution is governed by the heat diffusion equation for a steady state analysis:

$$\frac{\partial}{\partial x}\left(\frac{\partial T_i(x,y,z)}{\partial x}\right) + \frac{\partial}{\partial y}\left(\frac{\partial T_i(x,y,z)}{\partial y}\right) + \frac{\partial}{\partial z}\left(\frac{\partial T_i(x,y,z)}{\partial z}\right) = 0 \quad for\ \Omega_i \tag{5}$$

Where T_i is the temperature for compartment Ω_i, $i = 1 \dots n$; and n is the number of compartments in the receiver. The external conditions for the boundary value include: heat inflow (eq. 6), outflow for convection (eq. 7), and outflow for combined convection and radiation (eq. 8).

$$-k_i \cdot \left.\frac{\partial T_i(x,y,z)}{\partial x}\right]_{\Gamma_l} = q_o'' \quad for\ \Gamma_l \tag{6}$$

$$-k_i \cdot \left.\frac{\partial T_i(x,y,z)}{\partial x}\right]_{\Gamma_m} = h\big(T_\infty - T_i(x,y,z)]_{\Gamma_m}\big) \quad for\ \Gamma_m \tag{7}$$

13

$$-k_i \cdot \frac{\partial T_i(x,y,z)}{\partial x}\bigg]_{\Gamma_n} = h\big(T_\infty - T_i(x,y,z)]_{\Gamma_m}\big) + \sigma\varepsilon\big(T_{sur}^4 - T_i(x,y,z)]_{\Gamma_m}^4\big) \quad for \ \Gamma_n \tag{8}$$

Where k is the thermal conductivity of the material i, q_o'' is the heat inflow on the absorber, h is the convection film coefficient, T_∞ is the ambient temperature at a surface; Γ_l, Γ_m, and Γ_n are specific surfaces where each external boundary condition is located. For interfaces between compartments (perfect contact between surfaces), the temperatures must be the same, and fluxes crossing the interface must be equal [54]. The following equations give the internal boundary conditions for these cases, respectively.

$$T_i(x,y,z)]_{\Gamma_p} = T_{ii}(x,y,z)]_{\Gamma_p} \quad for \ \Gamma_p \tag{9}$$

$$-k_i \cdot \frac{\partial T_i(x,y,z)}{\partial x}\bigg]_{\Gamma_p} = -k_{ii} \cdot \frac{\partial T_{ii}(x,y,z)}{\partial x}\bigg]_{\Gamma_p} \quad for \ \Gamma_p \tag{10}$$

Where indexes i and ii are for two neighbored compartments, and Γ_p is the surface that the compartments are in contact.

The temperature profiles of the absorbers under different concentration ratios (CR) and absorber areas were simulated using finite element methods (FEM). ANSYS® 14.5 (ANSYS, Inc. Canonsburg, PA) was used to perform the analysis. The energy input for the FEM model is the solar radiation values collected at East Lansing, MI. The geometric model of the receiver and absorbers for the FEM model is presented in Figures 3b and c. Temperature inside the receiver was measured and taken as the input for the simulation. The heat inflow received by the absorber is described as:

$$q_o'' = \dot{Q}_{solar} \cdot \tau_l \cdot \tau_g \cdot \alpha_m \cdot A_l \tag{11}$$

Where $\dot{Q}_{solar}$ is the heat flux from solar radiation measure by pyranometer, τ_l and τ_g are the transmittance of the lens and the thermal glass, respectively, α_m is the absorbance of the metallic plate, and A_l is the area of the lens. Transmittances are obtained from technical specifications from the metallic absorber manufacturer ($\tau_l = 0.92$ and $\tau_g = 0.90$). Absorbance is assumed to be equal to the emittance (ϵ_m) of mild steel. It has been reported that ϵ_m ranges from 0.3 for clean and polish surface to 0.8 for oxidized surface [55]. For this study, since the absorber surface is neither polished nor totally oxidized (Figure 3c), ϵ_m is set at 0.5. Other parameters for the FEM simulation are listed in Table 1.

Table 1. Parameters used in FEM simulation

Concentration ratio (CR)	256			576			1000		
Absorber	1.5x1.5	2x2	2.5x2.5	1.5x1.5	2x2	2.5x2.5	1.5x1.5	2x2	2.5x2.5
$\dot{Q}$ Heat flow (W)	11.06	11.78	11.87	10.87	11.63	11.36	10.77	11.65	11.71
Ambient temperature (°C)					20				
Emissivity of the absorber					0.5				
External convection (W/m²·°C)					8				

14

Inside receiver convection (W/m²·°C)	10

3.1.1.4 Data collection

The distance "Y" between the lens and the absorber is adjusted from the focal length of 609.6 mm to 582.34 mm and 590.09 mm to achieve concentration ratios of 256 and 576, respectively (Figure 2f). Temperature at the center of the absorber was measured by a thermocouple type K that is connected to a CR800 Data Acquisition System (DAQ) (Campbell Scientific, Inc. Logan, UT). A FLIR E60 thermal camera (FLIR Systems, Boston, MA) with a resolution of 320×240 pixels and thermal sensibility of less than $0.045°C$ is also used to verify temperature profile of thermal absorbers. Solar radiation is measured using a LI 200 pyranometer (LI-COR, Lincoln, NE) that is also connected to the DAQ. Temperature inside the receiver (Figure 3) was measured using a thermocouple type K connected to a multimeter MN35 (Extech Instruments), which was registered manually each 10 minutes. The LabVIEW recorded the movement of the collector every 60 seconds.

3.1.1.5 Statistical analysis

One-sample t-test was used to compare the measured temperature and simulated temperature from the FEM model. The confidence interval of the mean is set at 90%, and the corresponding p-value is 0.1. The t value is determined by the following equation.

$$t = |\frac{\overline{T} - T_0}{\frac{s}{\sqrt{n}}}| \tag{12}$$

Where t is the t-value, T_0 is the simulated temperature, $\overline{T}$ is the average temperature from multiple measurements. s is the sample standard deviation of the temperature measurements. n is the number of measurements.

3.1.2 Designing new small-scale solar thermal receivers (quarterly report, 10/2015 7/2015, 1/2016, 7/2016)

Two new receiver designs consisting of cavity and conical solar thermal absorbers were designed for small-scale solar thermal collection (Figure 6). Transferring thermal energy in small-scale systems is always accompanied by the issue of how to use a small heat transfer area to heat a relatively large amount of working fluid to the targeted temperature. In addition, energy loss to the ambient environment is another problem that significantly reduces the thermal efficiency of such receiver units. In order to address these issues, the objective is to increase the contact time of the working fluid with the heat source to overcome the disadvantage of the small heat transfer area, and to apply a vacuum to reduce heat losses significantly, so that the thermal efficiency of small solar receivers can be significantly improved.

Based on this idea, the new receivers were housed in a vacuum chamber with a quartz thermal-glass (Novatec 825F, with a thickness of 9.525 mm (0.375 in)) at the top, a heat exchanger sitting in the vacuum chamber, and thermal insulation (Pyrogel XT) to cover the entire chamber. The vacuum chamber was sealed with O-rings (Parker S455-70) to maintain the inner pressure at -0.84 bar abs (25 inHg).

In order to address the issue of a small transfer area, the contact time of the working fluid with the absorber of the receiver needs to be extended. The conical absorber has a single fluid path so that the working fluid enters the absorber from its bottom and leaves from its top (Figure 7a). Since the conical shape of the absorber provides an effective heat transfer area, the heat transfer area is significantly increased. The cavity absorber has a spiral cave in the receiver. The working fluid pumping through the cavity absorber has multiple flow paths. The residence time of the working fluid is also increased. In the spiral cavity, the working fluid enters the absorber from the bottom of the chamber, reaches the center of the heating area, rotates in the spiral shape, and exits at one side of the receiver. During the process, the working fluid needs to travel along several parallel paths to extend the residence time and improve the efficiency.

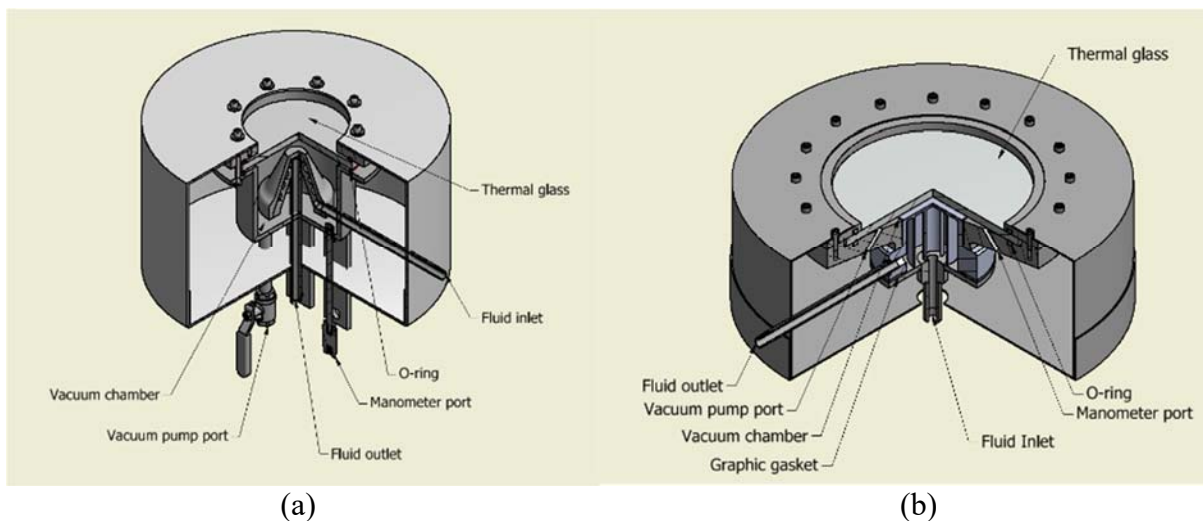
(a)   (b)

Figure 6. Solar receivers: (a) with conical absorber; (b) with cavity absorber
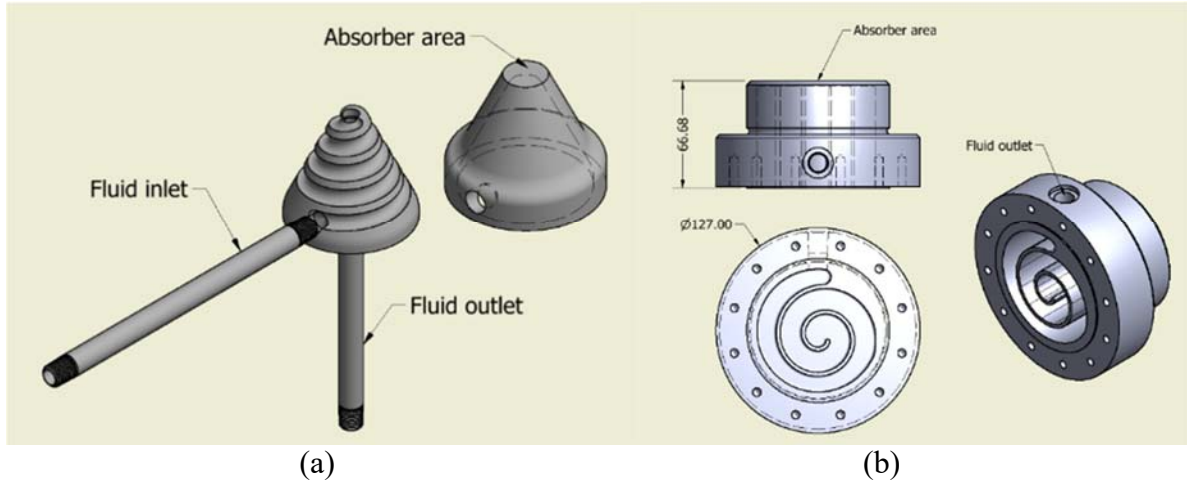
Figure 7. Heat absorbers: (a) conical absorber; (b) cavity absorber

The geometric characteristics of both absorbers are listed in Table 2. The inner volumes of the conical and cavity absorbers (single flow path and multiple flow paths) were 16,527 mm^3 and 229,645 mm^3, respectively. For volumetric flows of 11,507 mm^3/s and 5,753 mm^3/s, the residence times for the conical absorber were 1.44 s and 2.88 s, respectively; while those for the cavity absorber were 19.96 s and 39.92 s, respectively. The dimensions of the two receivers are shown in Figure 8. The receiver size was selected based on a solar collection area of 1 m^2. A refractive Fresnel lens was used as the solar thermal concentrator for this study.

Table 2. Design parameters for the absorbers

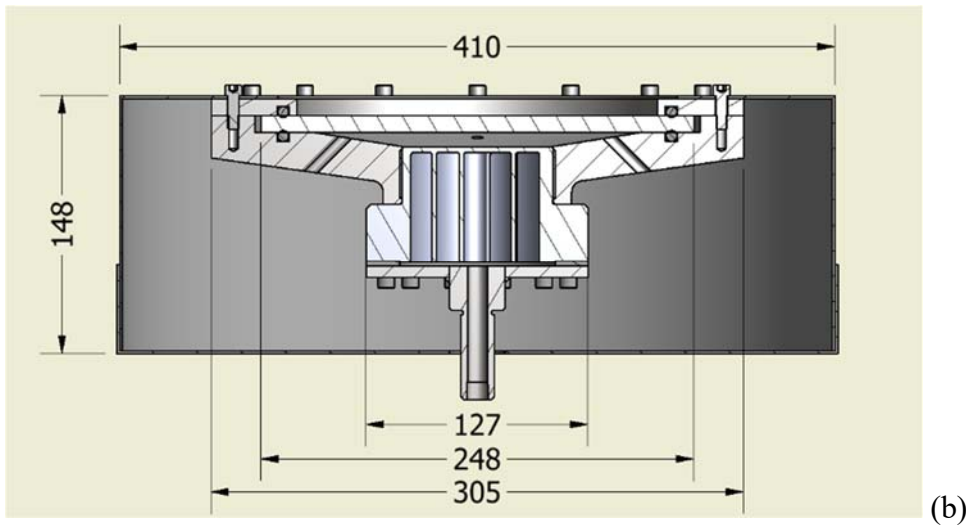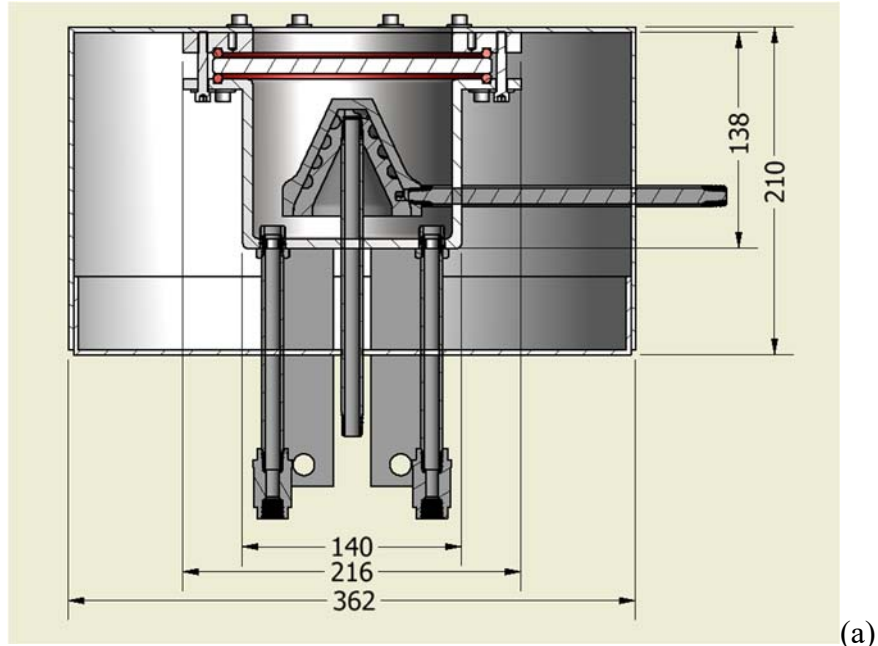| Receiver type	Fluid contact area (mm^2)	Volume (mm^3)	Fluid volumetric flow (mm^3/s)	Residence time (s)
Conical absorber	11,426	16,527	11,507	1.44
			5,753	2.88
Cavity absorber	59,001	229,645	11,507	19.96
			5,753	39.92

Figure 8. Dimensions of the solar receivers (in mm): (a) with conical absorber; (b) with cavity absorber

Based on the design, the solar receivers were installed on the aluminum frame, moved by a gearbox connected to brushless motors (Figure 9). Tracking system consists of a control module, with the NREL solar position algorithm, power supply, two drivers, and magnetic limit switches for position control. The resolution of movement is given by:

$$r = \frac{360}{P \cdot R_1 \cdot R_2}$$

Where r is the resolution of the azimuth and zenith angles (degree), P is the number of pulses per revolution, R_1 (1:236) and R_2 (1:62) are the reduction ratio of the planetary gears and worm gear, respectively. The receiver and lens configuration can be adjusted with a resolution of

18

±0.012° for altitude and zenithal position. This resolution permits, with an interval of movement of 30 seconds, an accurate position of the lens to concentrate the sun radiation in the heating surface (concentration ratio of 500).
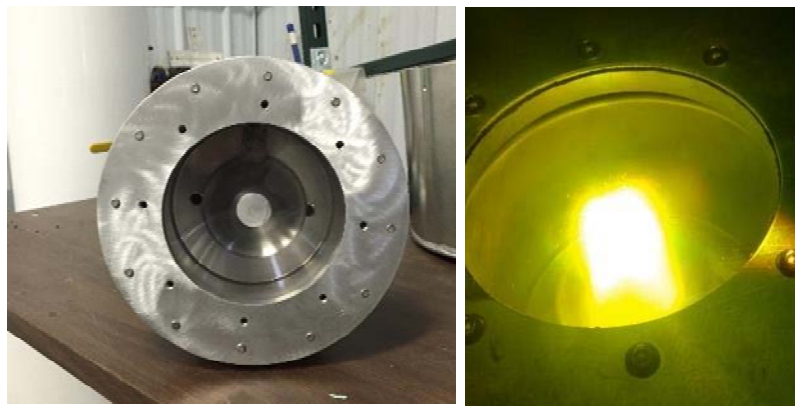

Figure 9. Solar receivers with conical absorber and cavity absorber. (a) Conical absorber; (b) Solar receiver with conical absorber in action; (c) cavity absorber; (d) Solar receiver with cavity absorber

3.1.3 Comparison of Brayton and Rankine cycles for small-scale solar-bio-hybrid power generation at different locations

In order to develop small-scale solar–bio hybrid power generation, 30 kW power generation systems, including three unit operations consisting of AD, solar thermal collector, and engines were comprehensively analyzed in this paper. Biomethane from anaerobic digestion and thermal energy from solar collection were used as the energy sources to power engines to generate electricity and heat. Gas and steam turbines as engine units were compared to determine the most suitable for the studied solar–bio hybrid system. The net capacity factor (the ratio of the energy output to the total energy generation of the system in a given time duration) and solar and biogas utilization factors (the percentage of each energy source used to generate the electrical energy) were used as parameters to evaluate the energy generation and optimize the system configuration.

Thermodynamic models were established to analyze the solar–bio hybrid systems consisting of gas and steam turbines (Figure 10). The biomethane production for the studied systems was based on a biomethane plant using thermophilic anaerobic digestion on a mixture feed of dairy manure and food wastes (90:10 ratio, 5% total solids) [56]. The anaerobic digestion with a culture temperature of 50 °C and a hydraulic retention time (HRT) of 20 days produced 0.38 m^3 methane per m^3 digestion solution per day (the low heating value of methane is 34 MJ/m^3 [57]). The steam turbine includes a condenser to recycle the water in a closed-loop circuit (Figure 10a). The gas turbine uses a regenerator to transfer energy from the exhaust gases into the compressed air in an open-loop air circuit (Figure 10c). Both systems contain water heat storage to collect energy from the thermodynamic cycle for the heat demand of the anaerobic digester (to maintain the digestion temperature and heat the influent). The solar–bio hybrid power generation systems (which include a secondary heat source of solar energy) have slightly more complicated configurations than the turbine power generation systems. Molten salt is used as the solar thermal storage [58].
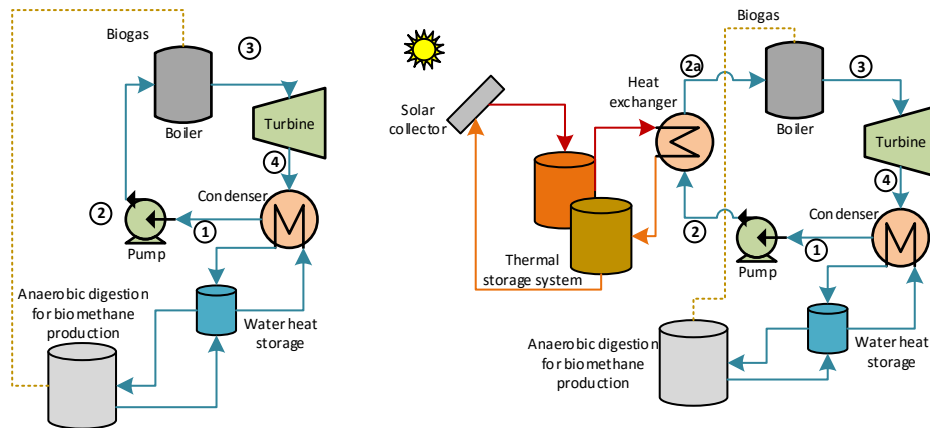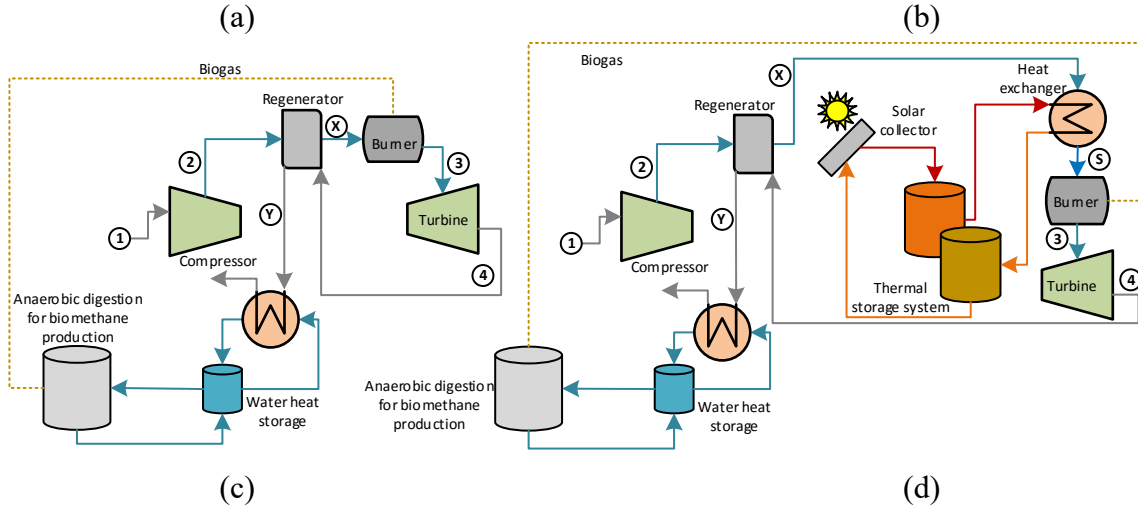
Figure 10. Schematics of the studied solar–bio hybrid power generation systems*
*: (a) the biomethane steam turbine; (b) the solar–bio hybrid power system with steam turbine; (c) the biomethane gas turbine; (d) the solar–bio hybrid power system with gas turbine.

In the solar–bio hybrid system with steam turbine, a heat exchanger was implemented to use the heat from the solar thermal storage to heat the working fluid prior to entering the biomethane boiler. The boiler further heats the working fluid to generate superheated steam to power the steam turbine (Figure 10b). The solar–bio hybrid system with gas turbine uses the heat from the solar thermal storage to raise the temperature of the hot air from the regenerator in the heat exchanger. This is done before the air is mixed with biomethane fuel in the burner to generate heat for the gas turbine (Figure 10d). The analyses were based on a constant electricity generation of 30 kW for all studied systems. The operational parameters of the thermodynamic models are listed in Table 3.

Table 3. Operational parameters of 30 kW steam and gas turbines*

System	Parameter	Unit	Value
Steam turbine (30 kW)	Water mass flow	kg/s	0.0807
	Steam inlet pressure (turbine)	bar	10
	Condenser pressure	bar	0.2
	Steam inlet temperature (turbine)	°C	200
Gas turbine (30 kW)	Air mass flow	kg/s	0.31
	Air inlet temperature (turbine)	K	1,113
	Compression ratio	-	3.2

| Air inlet temperature (compressor) | K | 300 |
| Air temperature after expansion | K | 912 |

*: The parameters are from commercial steam and gas engines *[59, 60]*.

The Rankine cycle was used to simulate the performance of the biomethane steam turbine. The working fluid consisting of water is pumped into the boiler that is maintained at constant pressure (Figure 10a and b). The power consumption of the pump and the enthalpies at points 2 and 4 in Figure 10 a and b are calculated by

$$w_P = v_\iota \cdot (P_i - P_o) \cdot 100/\eta_p \tag{13}$$
$$h_2 = h_1 + w_P \tag{14}$$
$$h_T = h_3 - \frac{W_s}{\dot{m}_{H_2O}} \tag{15}$$

where w_P is the pump work (kJ/kg_water); η_p is the pump efficiency (set at 0.65); v_ι is the specific volume (m³/kg); P_i and P_o are the inlet and outlet pressures in the turbine; h is the enthalpy at given temperature and pressure conditions (kJ/kg_water); W_s is the gross power generated (shaft work (30 kW), pump power ($w_P \cdot \dot{m}_{H_2O}$), and vacuum pump (0.5 kW)); and $\dot{m}_{H_2O}$ is the steam requirement (0.0807 kg/s). The fuel efficiency of the system is calculated based on the fluid properties at the inlets and outlets of the turbine and pump:

$$\eta_F = \frac{(h_3 - h_{4a})}{(h_3 - h_2)} \tag{16}$$

where $(h_3 - h_{4a})$ is the work performed in the turbine (kJ/kg_water). The enthalpy at condenser conditions (h_4) is calculated considering an isentropic turbine efficiency. To satisfy the required temperature and pressure of the feedwater for the selected 30 kW steam engine, the heat input Q_F and the heat extracted Q_H of the system are calculated as follows:

$$Q_F = \frac{\dot{m}_{H_2O} \cdot (h_3 - h_2)}{\eta_b} \tag{17}$$
$$Q_H = \dot{m}_{H_2O} \cdot (h_4 - h_1) \cdot \eta_c \tag{18}$$

where η_b is boiler efficiency (set at 0.85); and η_c is the condenser efficiency (heat sink) (set at 0.85). The simulation results for the steam turbine are presented in Table 4. The enthalpies at points 1, 2, and 3 (Figure 10) were 243.03 kJ/kg_water, 244.57 kJ/kg_water, and 2828.3 kJ/kg_water, respectively (Table 3). The temperatures at points 2 and 4a were 58.23 °C and 103.54 °C, respectively. The corresponding heat input and heat extraction were 245.33 kW and 134.61 kW, respectively. The thermal efficiency calculated for this particular equipment under the working parameters showed that 14.69% of the biomethane fuel was transformed into shaft work for electricity generation, and 54.87% of the biomethane fuel was turned into heat.

Table 4. Simulation results of a 30 kW steam turbine

Parameter	Unit	Simulation results
P_o	bar _abs_	0.2
w_P	kJ/kg_water	1.53

h_1	kJ/kg$_{water}$	243.03
h_2	kJ/kg$_{water}$	244.57
T_1	°C	58.06
T_2	°C	58.23
h_3	kJ/kg$_{water}$	2,828.30
h_4	kJ/kg$_{water}$	2,205.2
T_4	°C	60.06
η_T	-	0.1469
Q_F	kW	245.33
Q_H	kW	134.61

In the solar–bio hybrid steam power system (Figure 10b), the solar thermal energy reduces the amount of heat required by the boiler, and consequently decreases the biomethane consumption. The solar thermal energy (Q_{solar}) heats the water and generates a mixture of saturated steam and liquid at 99.60 °C. The boiler then converts the rest of the liquid into saturated steam and superheats the steam to satisfy the required temperature and pressure by the turbine (200 °C at 10 bar abs). The enthalpy of the mixture after the solar heating is:

$$h_{2a} = \frac{Q_{solar}}{\dot{m}_{H_2O}} + h_2 \tag{19}$$

The heat added in the boiler (only required if Q_{solar} is lower than Q_F) is calculated by

$$Q_{bs} = \frac{\dot{m}_{H_2O} \cdot (h_3 - h_{2a})}{\eta_b} \tag{20}$$

where η_b is the boiler efficiency. As for the gas turbine, the Brayton cycle was used to simulate the turbine performance. The temperature (T_2^G) after the compressor (point 2 in Figure 10 c and d) was calculated by

$$T_2^G = T_1^G \cdot \left(1 + \frac{1}{\varepsilon_c} \cdot (r_P^\alpha - 1)\right) \tag{21}$$

$$\alpha = \frac{\gamma - 1}{\gamma} \tag{22}$$

where r_p is the pressure ratio between the inlet and outlet in the compressor; α is a constant; γ is the ratio between the specific heat at constant pressure and the specific heat at constant volume; and ε_c is the compressor efficiency ($\varepsilon_c = 0.82$). The temperature after the regenerator (Point X in Figure 10 c and d) is given by

$$T_x^G = T_4^G \cdot \varepsilon_R + T_2^G \cdot (1 - \varepsilon_R) \tag{23}$$

where ε_R is the regenerator efficiency ($\varepsilon_R = 0.78$). The heat input to the burner ($Q_F{}^G$) is calculated by

$$Q_F{}^G = \dot{m}_{air} \cdot \frac{Cp_3 \cdot (T_3^G - T_x^G)}{\varepsilon_{HC}} \tag{24}$$

where Cp_3 is the specific heat at $\frac{T_3^G + T_x^G}{2}$ [kJ/kg·K]; and ε_{HC} is the burner efficiency ($\varepsilon_{HC} = 0.98$). The temperature of the exhaust gases after the regenerator (Point Y in Figure 10 c and d) is given by

$$T_y^G = T_2^G \cdot \varepsilon_R + T_4^G \cdot (1 - \varepsilon_R) \tag{25}$$

The fuel efficiency for the gas turbine is:

$$\eta_F^G = \frac{W_s}{Q_F{}^G} \tag{26}$$

The heat extracted from the exhaust gases ($Q_H{}^G$) is calculated by

$$Q_H{}^G = \dot{m}_{air} \cdot Cp_{3a} \cdot (T_y^G - T_F^G) \cdot \varepsilon_L \tag{27}$$

where Cp_{3a} is the specific heat at $\frac{T_y^G + T_1^G}{2}$ [kJ/kg·K]; T_F^G is the temperature of the exhaust gases (assumed as 85 °C); and ε_L is the efficiency of the heat exchanger and set at 0.75.

The simulation results for the gas turbine analysis are listed in Table 5. For a constant air inlet temperature, the heat input and heat extracted was 109.83 kW and 45.50 kW, respectively. The compression increased the air temperature from 300 K at point 1 to 444.58 K at point 2. The regenerator further increased the air temperature to 806.83 K at point X before the air was mixed with biomethane in the burner. The gas turbine unit uses 27.32% of the biomethane for the shaft work of electricity generation, and 41.43% of the biomethane to generate heat.

Table 5. Operational parameters of a 30 kW gas turbine

Parameter	Unit	Simulation results
η_F^G	-	0.273
T_2^G	K	444.5
T_x^G	K	806.83
T_y^G	K	549.75
$Q_F{}^G$	kW	109.83
$Q_H{}^G$	kW	45.50

With the addition of solar thermal energy (Figure 10 d), the heat demand of the biomethane burner is also reduced. The temperature after the solar collector is calculated as follows:

$$T_S^G = T_x^G + \frac{Q_{solar}}{\dot{m}_{air} \cdot Cp_{2a}} \tag{28}$$

where Cp_{2a} is the specific heat at $\frac{T_x^G + T_3^G}{2}$ [kJ/kg·K]. In addition, due to seasonal and geographical variation of solar radiation, the location of the studied systems has a great impact on their performance. The direct normal irradiance (DNI) and ambient temperature decrease with

24

an increase in latitude. Therefore, the two locations of Lansing (MI) and Phoenix (AZ) in the United States, which have significant temperature differences and solar radiation, were selected for this study. Figure 11 represents solar radiation and ambient temperature during a year for both locations [61, 62].
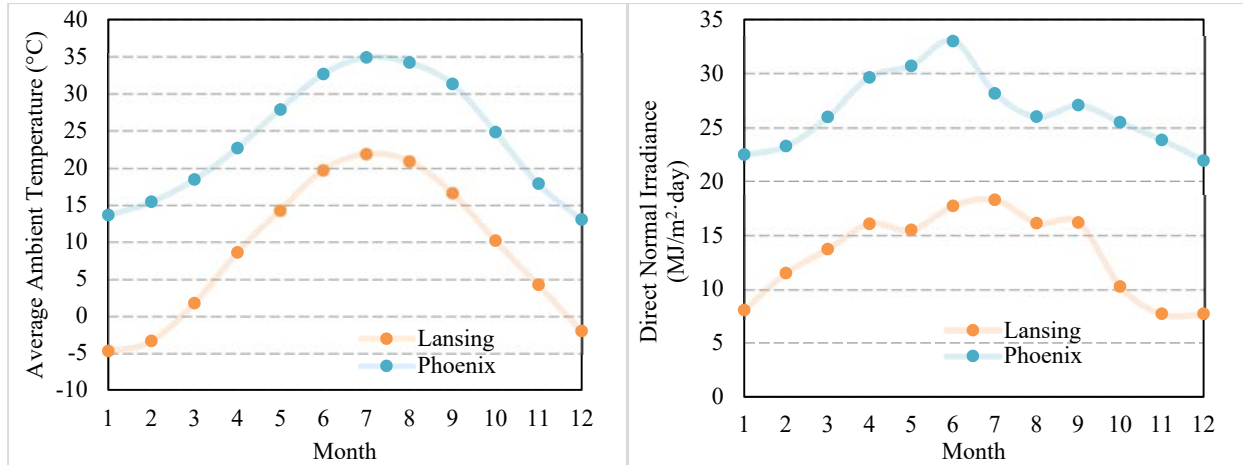

Figure 11. Monthly average temperature and DNI for Lansing and Phoenix

3.2 Optimizing lab-scale upflow fixed-film anaerobic digestion on blackwater and food wastes

3.2.1 Designing and implementing a lab-scale upflow fixed-film anaerobic digestion

Due to the relatively dilute waste stream, an upflow fixed film type digester using plastic Pall rings as supportive medium was applied (Figure 12). The main body of the digester is made of 3" OD clear PVC pipe; each digester has 1 L of working volume for liquid digestate and approximately 0.5 L of headspace for biogas. The plastic Pall rings (1 inch diameter) were introduced to prevent the accumulation of foam formed during digestion as well as to increase the surface area for anaerobic microbes to attach and grow. The biogas produced is exported through an outlet on the top of the digester. A water-displacement gas meter is used to measure biogas daily production. Given the small working volume, the bench scale digester is fed manually once or twice per day, depending on the hydraulic retention time (HRT).
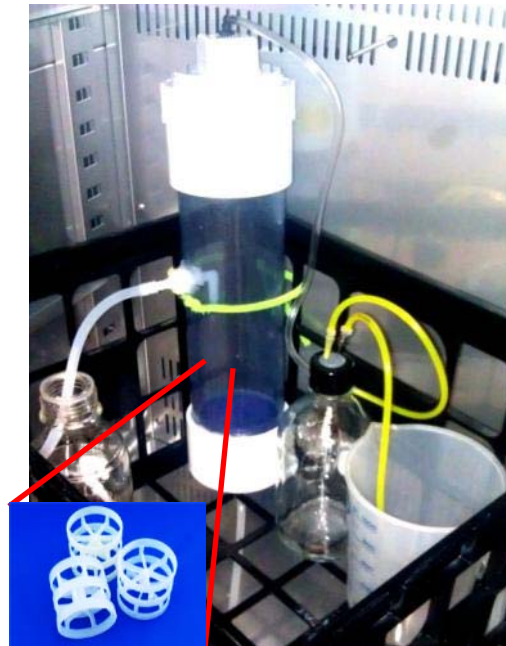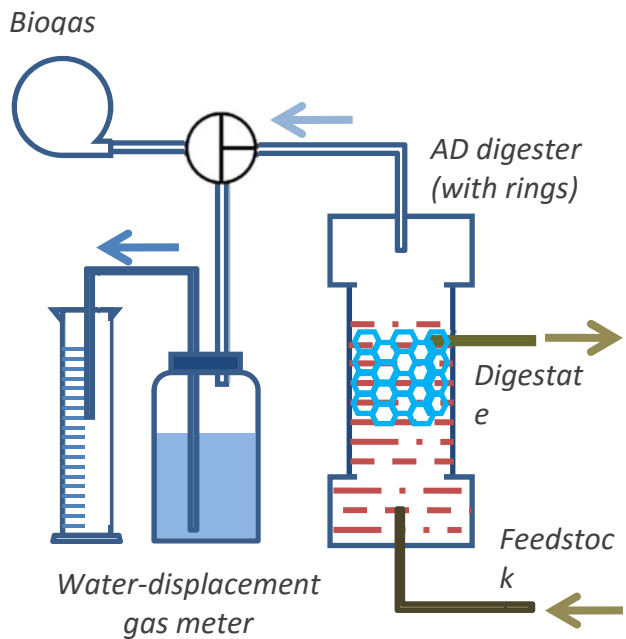
(a)   (b)
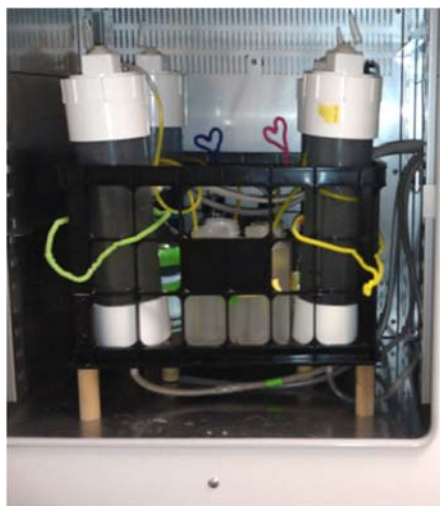
(c)
Figure 12. Upflow fixed film anaerobic digester system
(a) Flow diagram of the fixed film anaerobic digestion system. (b) The digester with Pall rings.
(c) The fixed film digesters

3.2.2 Evaluating the anaerobic digestion on mixed feedstock

In order to optimize anaerobic digestion of food waste and domestic wastewater, and maximize solid reduction and biogas production, the effects of feedstock concentration, hydraulic retention time (HRT), and temperature were investigated by a completely randomized design (CRD). Given the high oil content and low buffer capacity of the food waste, three feedstock concentrations of 1, 3 and 5% total solids (TS) were studied in this research. Compared to other anaerobic digester design, the upflow fixed film system principally requires shorter HRT because of the accumulation of microbes in the digester, therefore, three short HRTs of 4, 6 and 8 days were chosen for this experiment. In addition, temperature has a big impact on AD. Two culture temperatures of 35°C (mesophilic) and 50°C (thermophilic) were studied as well in this task.

3.3 Studying electrocoagulation to reclaim water
3.3.1 Studying the effects of electrocoagulation on the AD effluent treatment
3.3.1.1 Preparation of the liquid AD effluent
　　AD effluent was obtained from a commercial anaerobic digester in the Anaerobic Digestion Research and Education Center (ADREC) at Michigan State University (MSU). The AD effluent was first filtered with a 200-mesh sieve to remove large-sized chunks. The filtrate was collected and then diluted with water to an initial total solid (TS) of approximately 1% (w/w). The diluted filtrate as the liquid AD effluent for this study was collected and stored at 4 °C. The characteristics of the liquid AD effluent were listed in Table 6.

Table 6 Characteristics of AD liquid effluent

Parameters	Value
pH	7.5-8.0
TS (w/w %)	0.90 ± 0.03^a
TSS (mg L^{-1})	4125^b
TDS (mg L^{-1})	2035^b
TOC (mg L^{-1})	2332^b
Color absorbance (527.5 nm)	0.718^b
Conductivity (μs cm^{-1})	4740.7^b
COD (mg L^{-1})	9140 ± 140^a
TP (mg L^{-1})	340 ± 17.3^a
TN (mg L^{-1})	1233 ± 101^a

a: Data represent the average of three replicates with standard deviation.
b: Data represent the average of two replicates.

3.3.1.2 Experimental setup
　　A combined EC and biogas pumping unit was established to carry out the study. The liquid AD effluent was first treated by an EC, the liquid portion from the 1st EC treatment was separated and bubbled by raw biogas, and then a 2nd EC was applied on the biogas treated liquid to reclaim the water (Figure 13). Another combined EC process without biogas pumping was also conducted as the control.

(a)

(b)

(c)
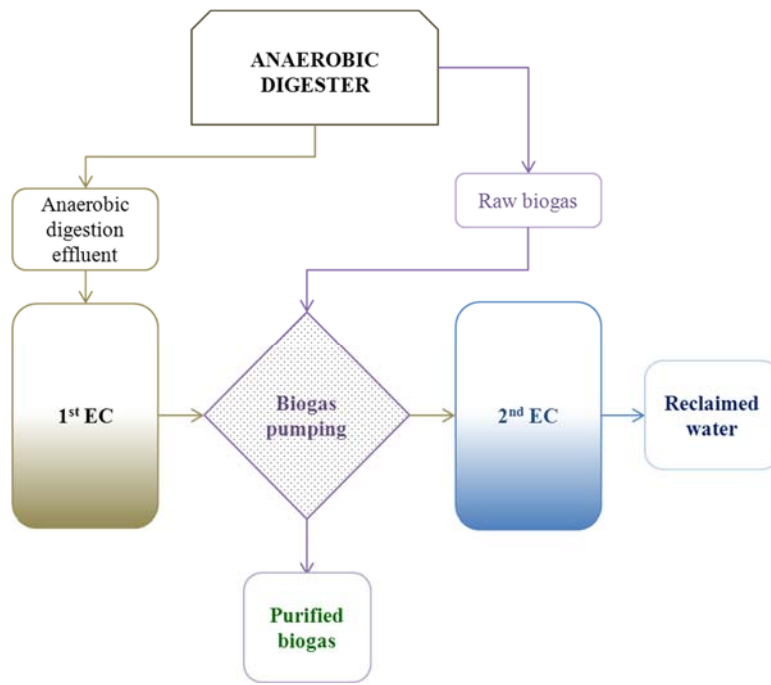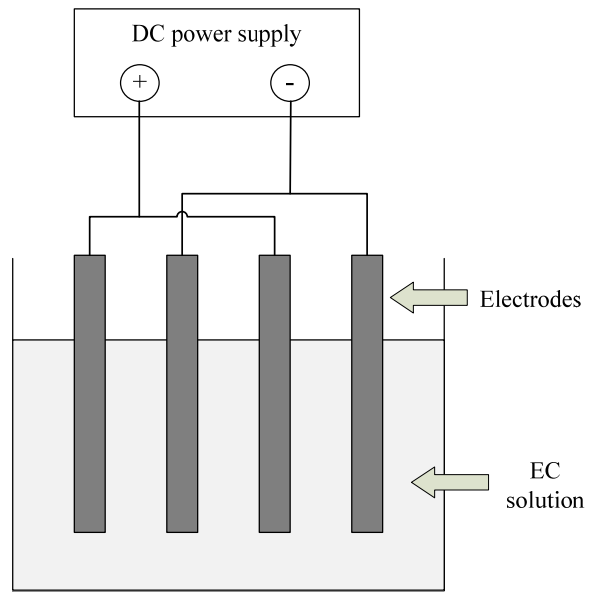
Figure 13 Demonstration of EC treatment and biogas pumping process.
(a) Flowchart of EC and biogas pumping process. (b) Schematic of the EC unit. (c) Schematic of the biogas pumping unit

3.3.1.3   EC setup and operation

DC power supply (XPOWER™ 30V 3A) was selected to provide electricity. Two pairs of steel CRS 1018 were used as electrodes for both anodes and cathodes (Figure 13(b)). Three different effective electrode surface areas of 62 cm^2, 134 cm^2 and 210 cm^2 were tested. Rec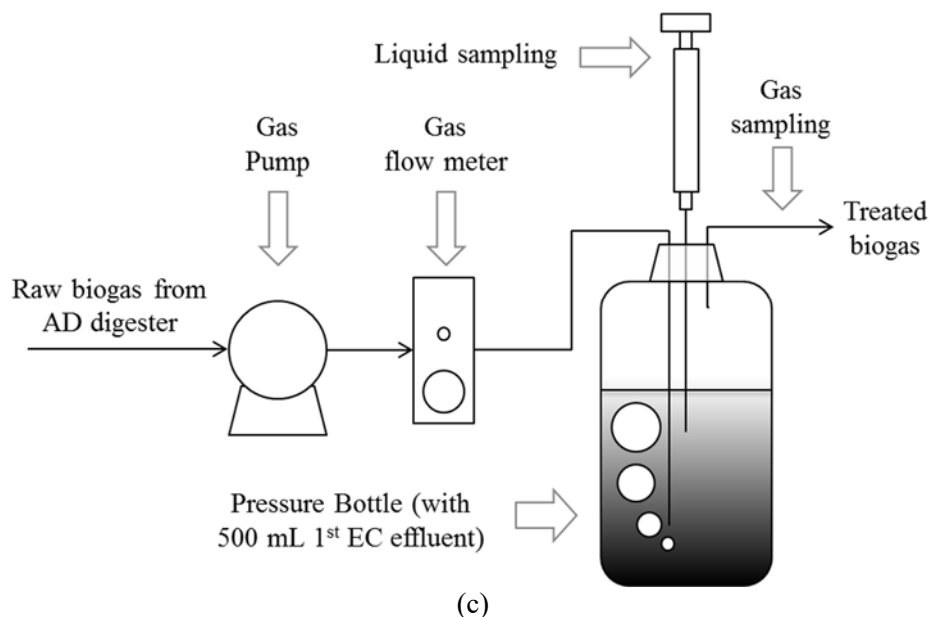tangular glass containers (effective volume of 500 mL) were adopted as reactors. PVC holders were placed on the top of the beakers to hold electrodes in the reactors with 1 cm distance between electrodes. The electrodes were connected with power supply and with each other in parallel pattern.

Five hundred milliliter of the liquid AD effluent was used for individual EC runs. Voltage and power consumption were monitored throughout EC operation via a Kill A Watt ™ power monitor. The pH was also measured with Fisher ™ Scientific pH meter. The EC treated liquid was separated into three phases of top foaming layer, middle supernatant, and bottom solid layer. Post-EC treatments described as follow were conducted differently for 1st EC and 2nd EC. Post 1st EC treatment: Three layers were clearly separated after the 1st EC treatment. The middle part was siphoned out and stored at 4 °C.

Post 2nd EC treatment: Since the middle supernatant was overlapped with the thicker top foaming layer and bottom solid layer, a mixing and settling process was applied after the 2nd EC. After 30 min settlement, the clear supernatant was collected for nutrient analysis and removal efficiency evaluation.

3.3.1.4   Biogas pumping setup and operation

500 ml of collected supernatant (middle part) from the 1st EC was used as the solution. Raw biogas was bubbled into the solution via a pump (Gast™), and the flow rate was controlled at 1 vvm (volume gas/volume treated liquid/minutes, the corresponding flow is 0.5 L/min) by an air flow meter from VWR ™. The gas flow correction factor of the air flow meter to measure biogas flow is 1.0067, which is calculated based on the specific biogas gravity (1.011) at the

30

operational conditions of 35°C and 5 inches water pressure. A gas outlet on the top of the bottle and a luer-lock 12'' gauge 20 needle submerged in the solution were installed for releasing biogas and taking biogas and liquid samples, respectively (Figure 13(c)). Bubble size was around 1 mm of diameter (based on the observation from pumping the biogas into the tap water). Liquid samples were taken every 10 min for pH measurement. Airbags were used to take gas samples. H_2S concentrations in the original biogas and treated biogas were monitored during the pumping process.

3.3.1.5 Experimental design

A complete random design (CRD) was applied to optimize the 1st EC treatment. Three factors of current strength (I), retention time (RT), and electrode surface area (SA) were studied to conclude removal efficiencies of TS, COD and turbidity. Three levels of individual factors were tested: 0.5A, 1A, and 2A for I; 20, 40, and 60 min for RT; and 62, 134, and 210 cm^2 (A, B, C) for SA.

For the 2nd EC treatment, a CRD was again used to study the effects of the experimental conditions on water reclamation. Three levels of I (0.5A, 1A, and 2A) and two levels of RT (20 and 40 minutes) with a fixed SR of 62 cm^2 were tested; TS, COD, TP, and TN were measured to evaluate the performance of the 2nd EC.

3.3.1.6 Mass balance analysis

In order to evaluate the performance of the studied EC processes, mass balance on total iron, total nitrogen, total phosphorus, sulfur, and water was conducted on the preferred conditions of the EC processes with biogas pumping (BP) and no biogas pumping (NBP). Since water reclamation is a target of this study, liquid recovery was used to present how much water can be reclaimed by the preferred processes. The liquid recovery is defined as: liquid recovery (%) = volume of the reclaimed water after the treatment (ml) / volume of the original solution before the treatment (ml) x 100%.

3.3.1.7 Analytical methods

TS content was measured according to the dry weight method. COD, total phosphorus (TP) and total nitrogen (TN) were analyzed via HACH ™ standard methods [63]. Turbidity was measured by the EPA standard method [64]. The total iron concentration was analyzed by HACH™ standard metal prep set TNT™ 890. The sulfide ion concentration in the solution was tested by USEPA 4500-S2-D Methylyne Blue Method using a standard kit from HACH™. Ionic conductivities of liquid samples were measured using conductivity probe (Vernier Software & Technology, US). Total carbon (TC) and inorganic carbon (IC) were measured by a Shimadzu TOC-VCPN Total Organic Carbon Analyzer (Columbia, MD, USA). Total organic carbon (TOC) was calculated using TC to subtract IC. Total suspended solid (TSS) and total dissolved solid (TDS) were analyzed based on the following procedure: The solution was naturally settled for 30 min; Specific volume for different solution (25 mL for EC treated effluent and 10 mL for AD effluent) was filtered through a glass fiber filter with pore size of 0.7 μm and diameter of 25 mm (EMD Millipore, Germany); Filtrate and retained solid on the filter were then dried at 105°C overnight to obtain TSS and TDS, respectively. The color of lipid samples (AD effluent and EC treated water) was measured at the wavelength of 527.5 nm that was the representative visible

wavelength for the effluents obtained from a light absorbance profiling test on Shimadzu UV-1800 spectrophotometer (Fig. S5).

Methane (CH_4), carbon dioxide (CO_2), and hydrogen sulfide (H_2S) contents in the biogas samples were measured using an SRI 8610C gas chromatography system. Hydrogen (H_2) and Helium (H_e) were used as a carrier gas with pressure set at 21 psi. The system was equipped with a thermal conductivity detector and kept at a constant temperature of 150 °C. The injection volume was 5 mL with 100 µL used for analysis. Ammonia (NH_3) and other trace gas components were identified using Agilent 6890/5973 GC/MS and CTC Combi PAL at the Michigan State University Mass Spectrometry and Metabolomics Core Facility. 100 µL gas sample with split ratio of 100:1 was injected into Agilent GS-GasPro® column (30 m, 0.32 mm, 7 inch cage). The separation of gas compounds was achieved using the temperature profile: 40°C for 2.8 min, 40°C min^{-1} to 260°C, and 260°C for 5 min. Gas compounds were identified by comparing their m/z values with the ChemStation database.

3.3.1.8 Statistical analysis

General linear model (GLM) analysis using the Statistical Analysis System program 9.3 (SAS Institute, Inc. Cary, NC) was conducted to investigate the effect of reaction conditions on EC. I, RT, and SA were taken as parameters. Analysis of variance (ANOVA) and pair-wise comparisons were used to interpret the data and draw conclusions.

3.3.2   Designing and implementing a bench-scale electrocoagulation unit

Based on the lab-scale experiments, a 40 L bench-scale EC reactor was designed and implemented for evaluation of EC treatment on AD effluent, which would provide valuable data for further scale up to deal with large quantity of AD effluent.

The EC vessel dimension is demonstrated in Figure 14. The flange cap is a 24" diameter by 1" thick cylinder cut out of 48" x 48" schedule 40 PVC sheet and secured to a flanged base. The flange base has an outer 24" diameter by 1" thick cut-out and has an additional center cut out of 18.7" that fits flush with the inside of standard 20" schedule 40 PVC pipe. The adjacent 20" diameter circle in the cap is sunk 0.50" into the 1" thick disk which fit flush around body of 40" long 20" diameter schedule 40 PVC pipe. The bench-scale EC reactor was presented in Figure 15.
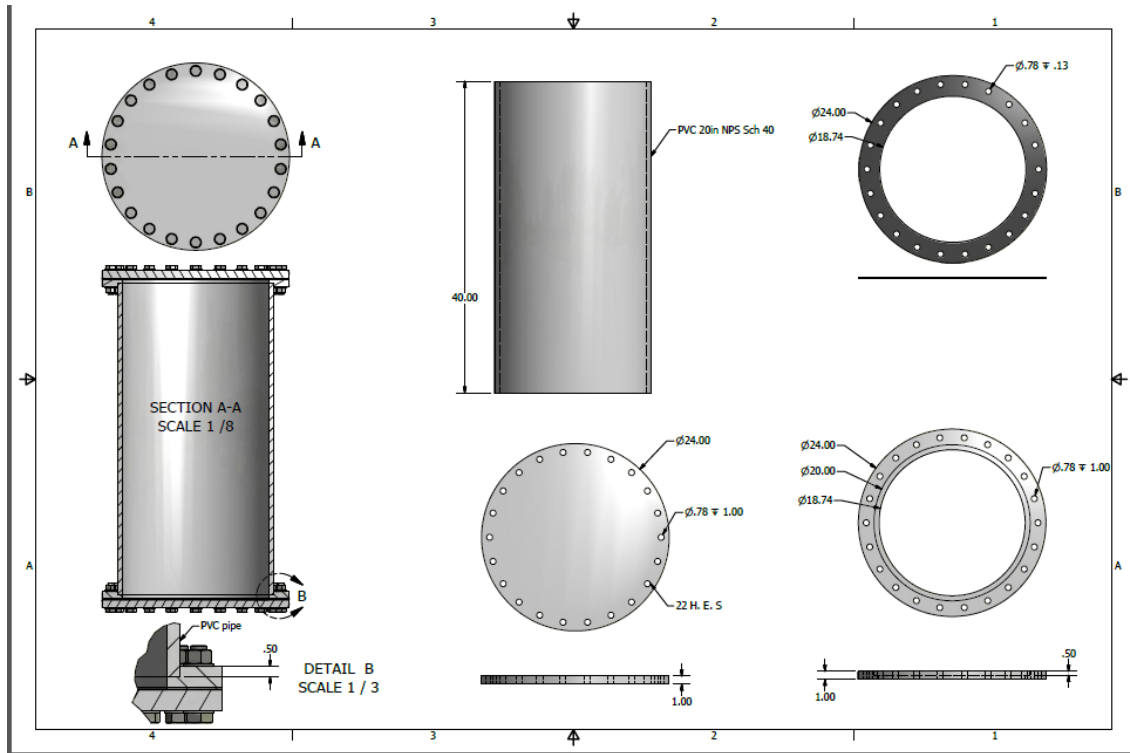
Figure 14. Overview of design for EC vessel

(a)   (b)

Figure 15. The bench-scale EC unit
(a). The pilot EC unit; (b). The cathodes of the unit

3.4 Investigating nano-filtration on potable water generation from the EC solution
3.4.1 EC solution

AD effluent was obtained from a 2500 m^3 completely stirred tank reactor (CSTR) in the Anaerobic Digestion Research and Education Center (ADREC) at Michigan State University. A two-stage EC treatment was then carried out as described in a previous study [65]. Current level of 2A was applied to two sets of electrodes with anodic surface area of 62 cm^2, effective volume of 0.5 L and retention time of 60 minutes. The middle layer with relatively less turbidity was siphoned out as the feed for the second stage of EC, which applied same electricity conditions for another 40 minutes. Solutions were centrifuged at 236 g for 10 minutes before being used for the membrane filtration experiments.

The TS measurement was done using the dry weight method. COD, TN and TP measurements were done using HACH^{TM} standards methods [66]. Total Carbon (TC) and Inorganic Carbon (IC) were measured using Shimadzu TOC-VCPN Total Organic Carbon Analyzer (Columbia, MD, US). Total Organic Carbon (TOC) was measured by subtracting the IC value from TC.

3.4.2   Preparing the membranes using layer-by-layer technique
3.4.2.1 Materials and filtration set-up

Poly(diallyl dimethyl ammonium chloride) (PDAC) (MW 100,000-200,000, 20 wt% in water), poly(styrene sulfonic acid sodium salt) (SPS) (MW 70,000), poly(allylamine hydrochloride) (PAH) (MW 900,000) and poly(acrylic acid sodium salt) (PAA) (MW 15,000, 35 wt% in water) were purchased from Sigma Aldrich. 2-(N-Morpholino) ethanesulfonic acid (MES) Buffer was also purchased from Sigma Aldrich. N-(3-Dimethylaminopropyl)-N′-ethylcarbodiimide hydrochloride (EDC) was from Fisher Scientific. Sodium chloride and potassium chloride crystals were procured from Avantor Performance Chemicals (Center Valley, PA). Three commercial membranes, NF 270, NF 90 and BW 30 from Dow Filmtec (Midland, MI) were used as the base membranes for this study. Among them, NF 270 and NF 90 are nanofiltration membranes, and BW 30 is a reverse osmosis membrane. All aqueous solutions were prepared using deionized (DI) water (>18.2 MΩ) supplied by a Barnstead Nanopure Diamond-UV purification unit equipped with a UV source and a final 0.2 μm filter. Unless specified all procedures were carried out at room temperature.

The HP 4750 stirred dead end cell (Sterlitech, Kent, WA) was connected to a nitrogen cylinder which acted as the pressure reservoir. The net volumetric capacity of the setup was around 300 ml. The unit was placed on a magnetic stirring plate. The filtrate was collected in a measuring cylinder. The flux was measured by the volume of water collected over a certain period of time. The effective membrane area for this setup was 14.6 cm^2.

3.4.2.2 Preparation of polyelectrolyte solutions and LbL assembly technique

Membrane preparation: The bare NF 270 membranes were stored in DI water prior to the LbL deposition. The permeate sides of the membranes were covered to prevent deposition of polyelectrolytes. The LbL deposition process was carried out using a Carl Zeiss Slide Stainer which employs a robotic arm to move the sample to different solution baths. For all polyelectrolytes, the concentration was maintained at 10 mM. PDAC and SPS were prepared in 0.5M NaCl solution. For the PAH/PAA multilayer assembly, the pH of PAH and PAA were adjusted to 8.5 and 3.5, respectively, using 1M HCl/1M NaOH. The dipping time in each polyelectrolyte solution was set to 10 mins. After each polyelectrolyte dipping step, the

substrates were rinsed with DI water three times consecutively (2 mins, 2 mins and 1 min). Following the deposition of one complete bilayer, the sample was sonicated for 2 mins in an ultrasonicator bath. The procedure was repeated till the desired number of bilayers was deposited. After LbL deposition, the membranes were soaked overnight in DI water.

Crosslinking of PAH and PAA with EDC: The EDC solution was prepared in a 50 mM MES Buffer solution at a concentration of 50 mg/ml and pH of 5.5. Following the deposition of PAH/PAA multilayers on the membrane surface using the aforementioned LbL protocol, the modified membrane was dipped in the EDC solution using the slide stainer for 60 minutes under continuous agitation. In order to remove the excess EDC, the samples were rinsed with DI water thrice for 15 minutes each time, followed by 5 minutes of sonication.

Dead end filtration protocol: The membranes were stored in DI water at least for 12 hours prior to usage. All membranes were first compacted by running pure DI water across them at a pressure of 10 bar. After two hours of compaction, the flux reached a steady state and was gravimetrically measured. Prior to using the wastewater, the latter was pre-filtered using a 0.22 μm Millipore filter. The pre-filtered wastewater was then filtered through the membranes under a pressure of 5 bar till the permeate volume reached 50 ml. The solution flux was calculated based on the time taken to filter 50 ml permeate across the membrane.

3.4.2.3 Membrane characterization

Measurement of streaming potential: The surface charge of the membranes were measured using the Brookhaven EKA Electro-kinetic analyzer (BI-EKA, Brookhaven Instrument Corp., Holtsville, NY) equipped with a rectangular cell and a clamp cell. A poly (methyl methacrylate) (PMMA) substrate was used as the reference. All streaming potential measurements were carried out by using 1mM potassium chloride (KCl) as the electrolyte. The bypass lines and the cell were rinsed with KCl solution after being rinsed with DI water several times. At least three replicates were used for each of the membranes that were tested for streaming potential. In order to measure the membrane surface charge as a function of pH, the streaming potential tests were carried out with KCl solution at three different pH conditions (3, 7 and 9). The system was thoroughly rinsed with DI water between different pH conditions.

Measurement of thickness: The thickness of the PEM films was measured using a Dektak surface Profiler. Both types of PEM films were deposited on glass slides for the measurement. In order to reconfirm the values obtained from the profilometry tests, we used the J.A Woollam M-44 Ellipsometer. The PEM films were deposited on gold coated glass slides (VWR International, US). Prior to the LbL deposition, the gold-coated glass slides as well as the plain glass slides were treated with O_2 plasma for 20 minutes using a Harrick plasma cleaner (Harrick Scientific Corporation, Broading Ossining, NY) at 30 W RF power under 100 millitorr vacuum pressure. Immediately after the plasma treatment, the substrates were put in the slide stainer for the LbL surface modification, following the same protocol as described earlier. The model for generic films was used for the ellipsometry measurements, assuming a refractive index of 1.5. The thickness was determined along several spots on the substrate and at least three replicates of each type of PEM film were used to get an average value.

3.4.2.4 Membrane characterization

Student t-test, using a comparison-wise type I error of 0.05, was applied on the experimental data to compute significant differences between membranes regarding COD reduction and membrane permeability.

3.5 Establishing a small pilot-scale, self-sustaining system

The pilot-scale system was designed and implemented at the MSU Anaerobic Digestion Research and Education Center (ADREC) in East Lansing, MI. The system includes PV panels, Fresnel concentrated solar thermal collector with conical absorber, two upflow fixed film anaerobic digesters, an electrocoagulation (EC) unit, a nano-facilitated reverse osmosis unit, battery storage, power control unit, and system control interface (Fig. 16).

Figure 16. The self-sustaining pilot-scale system

A. 40 ft container (A1: outside of the container; A2: inside of the container); B. 700 L anaerobic digesters; C. Control room; D. Fresnel solar thermal collectors (12 one m^2 lenses); E. 250 L EC reactor; F. 5 L/min nano-facilitate RO unit; G. 300 L water tank; H. 2 kW centrifuge; I. Control panel; J. 2 kW heater; K. 1.5 kw gas engine; L. PV panels (23 m^2); M. feeding and receiving unit; N. power control; O. biogas storage; P. battery

The PV panels converted solar radiation into electricity to satisfy the electricity need of the system. Solar thermal collector and biogas heat are used to provide heat to the digesters as well as generate electricity (the electricity generation from biogas is in an intermittent mode). The digesters handles a mixture of food wastes and black water. The effluent from the digesters (AD effluent) is treated by the EC unit to reclaim the water. The EC solution (after EC treatment) is then centrifuged to remove the solids. The supernatant after the centrifuge is filtered by the nano-facilitated reverse osmosis unit to generate clean water. The design parameters for individual unit operation are presented in Table 7. The detailed individual unit operations are described as follow.

Table 7. Design parameters of individual unit operations

Parameters	Value
1. Anaerobic digestion operation	
Digester type [b]	Up-flow fixed-film
Feedstocks [a]	Black water & food wastes
Total Solid in the feed (TS) (%)	1-3
Digester size (L)	600
Retention time (days)	4-20
Digestion temperature (C)	35-50
2. ECF operation	
Current (A)	20
Voltage (V)	10
Reaction time (hours)	0.5-5
Operation volume (L)	240
3. Centrifuge	
Power (kW)	2
Speed (rpm)	3,000
Flow rate (L/minutes)	20
Time (minutes)	10
4. Nano-facilitated RO unit	
Ultra-filtration pressure (psi)	5
Nano- and RO pressure (psi)	45
Flow rate (L/minute)	5
Pump power (kW)	0.06
5. PV panels	
Type	235W panel & 60 cells per panel
Size of PV panel (m2/each)	1.62
Number of PV panel (unit)	14
6. Gas engine	
Fuel	Biogas
Power output (kW)	1.8
7. Electricity storage	
Battery	CDTrue 12-170FG
Battery size	12v, 170 aH

No. of battery	16
8. Power control	
Outback Radian GS4048A	4000 VA

a. The food wastes is from the MSU cafeteria. The black water is from East Lansing wastewater treatment plant. The data are the average of two replicates.
b. There are two reactor. Each of them has an effective volume of 300 L.

3.5.1 The anaerobic digestion unit operation

The digestion operation includes two units of feeding and digestion (Figure 16 B and M). 100 L vessel with a grinding pump inside is used to receive food waste and black water, and to feed the upflow digesters. Level sensors are installed to automatically control the feeding volume.

Two high-efficiency fixed-film anaerobic digesters (300 L effective volume each) have been designed and manufactured (Figure 16 B, and Figure 17). This configuration significantly enhances the accumulation of microbial biomass (using Pall rings between Screens #1 and #2 to retain the biomass), and consequently improves the performance of the digestion. A heating coil is installed inside the reactor to maintain the required digestion temperature.
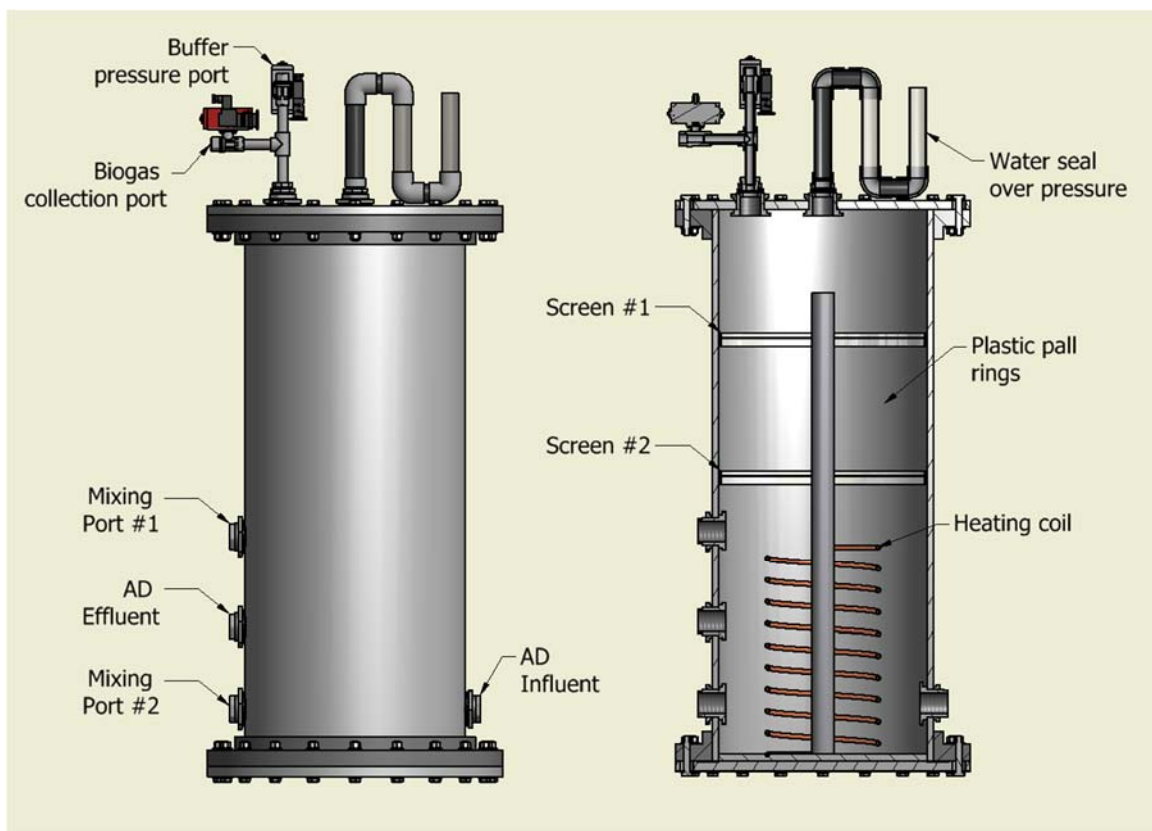

Figure 17. Design of the upflow fixed-film anaerobic digester

3.5.2 The water clarification unit operation

Electro-coagulation and membrane filtration are combined to further treat the AD effluent and generate the clean water (Figure 16 E, F, G, H). The AD effluent from the digesters

enters into the EC reactor to remove TS, COD, and phosphorus. The EC reactor consists of six metallic pipes (mild steel anodes) as the anodes to provide the ions, and a cylindrical metallic sheet (with a thickness of 3 mm) as the cathode completes the DC circuit for the electrochemical reaction (Figure 18). On the lid, a port is installed for biogas pumping. The After the EC treatment, the whole solution is centrifuged to separate supernatant from the settled solids. The supernatant (EC solution) is stored in the water tank (Figure 16 G). The EC solution is further cleaned up by a modified nano/ultra/RO membrane filtration unit (Figure 16 M). A commercial hosing is used to host the membranes. Based on the lab-scale experiments, four membrane filters (one coarse fiber pre-filter, one ultra-filtration, one nano-filter, and an RO filter) are implemented to convert the EC solution into the clean water.
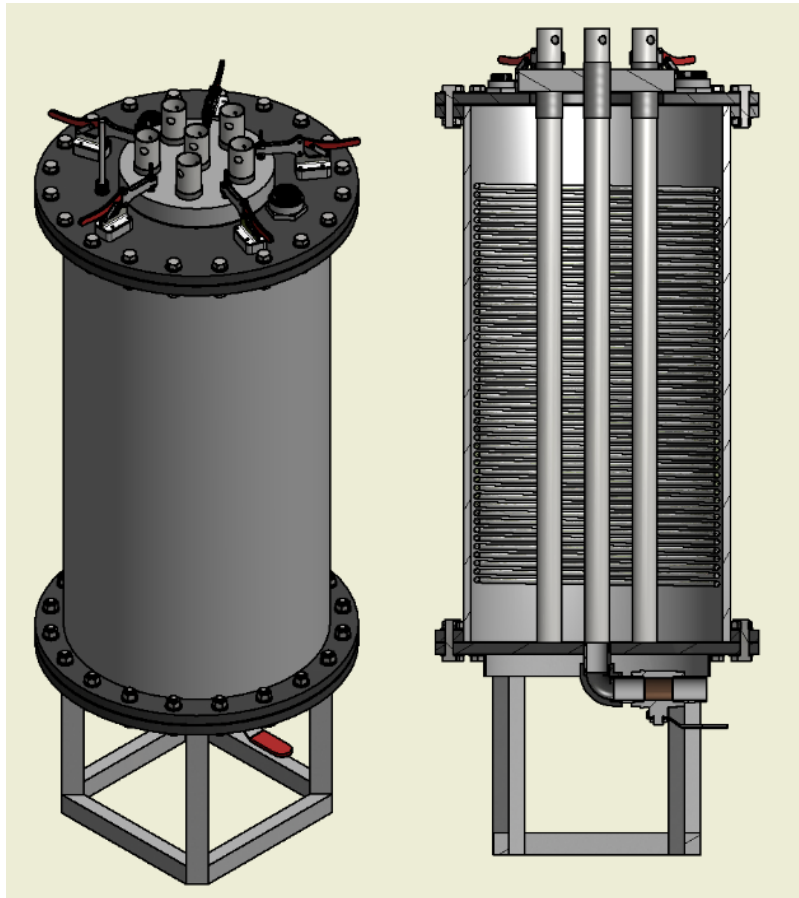

Figure 18. Electro-coagulation reactor for water clarification

3.5.3   Heat and electricity generation unit operation

The heat and electricity generation unit operation integrates both solar (PV and solar thermal) and biogas power generation. The photovoltaic unit includes 14 SolarWorld SW235 mono PV panels (total 23 m^3) and generates 4 kW electricity under reference conditions (cell temperature of 25 °C and a power of 1000 W/m^2). The concentrated solar thermal unit includes one Fresnel lenses (with an area of 1 m^2 each), a two-way kinematic gearbox, and a solar tracking control unit. The Fresnel lenses collect energy and use the conical absorber to transfer it to a heat exchanger. Synthetic oil (Dowtherm A) is used as the transfer media. The solar receiver is installed on the aluminum frame, moved by the gearbox connected to brushless motors. The

tracking unit includes a control module using the NREL solar position algorithm, a power supply, two drivers, and magnetic limit switches (for limiting movement of the lenses).

The biogas produced from the digestion is stored in a biogas storage bag (as the fuel storage) to support a 2 kw hot water heater and a 1.5 kw engine (the electricity generated from the engine compensates unsteady solar radiation). Both solar thermal (from Fresnel lens) and biogas energy are used by the pilot system to generate the heat to satisfy the temperature requirement of the digestion. PV panels are used to generate electricity to power the pumps, centrifuge, DC power supply, and control panel to satisfy operational requirements. Extra electricity generated from PV panels and 1.5 kw engine are stored in a battery bank to be used at night and other time without solar radiation. The battery bank consists of 16 CDTrue batteries (12 v and 170 Ah each). Outback Radian 4048 is used to do DC-to-AC conversion and manage the energy uses.

3.5.4   The control unit

The self-sustaining system is a fully automatic unit. The control unit include an Allen-Bradley CompactLogix Programmable Language Controller with data logging and remote access capability, an ten inch touch screen human machine interface (HMI), and an workstation. The functions of the control unit is listed in Table 8. The piping and instrumentation diagram (P&ID) is demonstrated in Figure 19. The control unit controls the system operation via 14 automatic valves, 4 hot water pumps, 5 slurry pumps, 1 grinding pump, 4 level sensors, 2 biogas flowmeters, 4 water flowmeters, and 14 thermocouples. The operational data (temperature, flows, pumping time, and power usage and storage) are automatically recorded in a time interval of 30 seconds, and saved as a .csv file. The interfaces of the system includes liquid overview, hot water overview, gas overview, feed sequence, EC sequence, trend, and calibration (Figure 20). The liquid overview shows the overall mass transfer in the pilot system. It includes a parameter set up for the mixing of the digesters. The hot water overview provides the temperature of digesters and hot water tank, and flow rates of heating transfer fluids. The gas overview presents the biogas flows from digesters and biogas storage. Feed sequence is used to set up the feeding schedule. EC sequence is for setting up the parameters for EC treatment. Trend shows the data of the key parameters. Calibration is for calibration of thermocouples. The entire system is remotely controlled by laptops or portable electronic devices.

Table 8. Key functions of the control unit

Control modules	Key functions
1. NEMA 12 enclose	• Housing for the switches
2. PLC with data logging and remote access capability	• Allen-Bradley CompactLogix • Ethernet communication for HMI and remote access • RS-232 ASCII communication for biogas flow meters • 32 Analog Inputs • 16 Digital Inputs • 48 Digital Outputs • Expandable I/O (local or remote via Ethernet)
3. Ten inch touch screen HMI interface	• Allen-Bradley Panelview Plus 6 • 'Soft' buttons for all manual/off/auto functionality • Alarming and alarm history • Data logging with on-screen trending

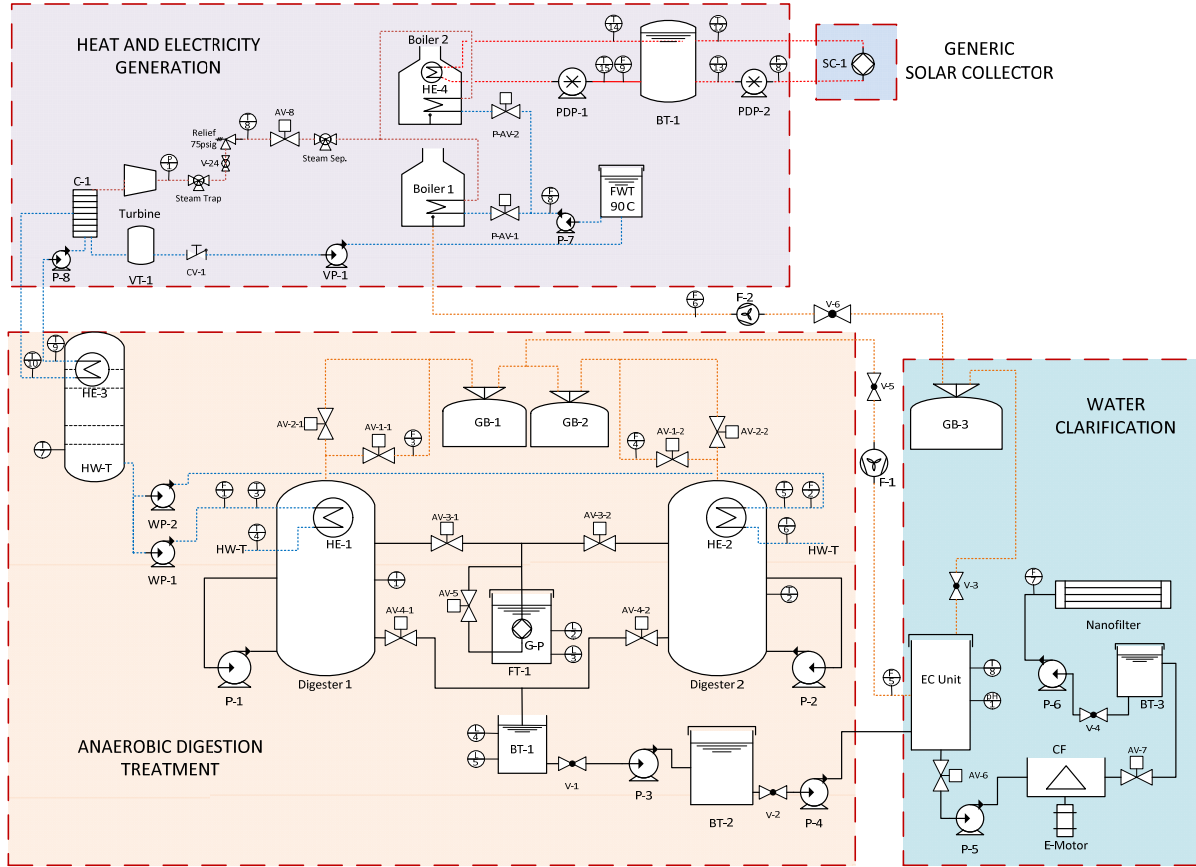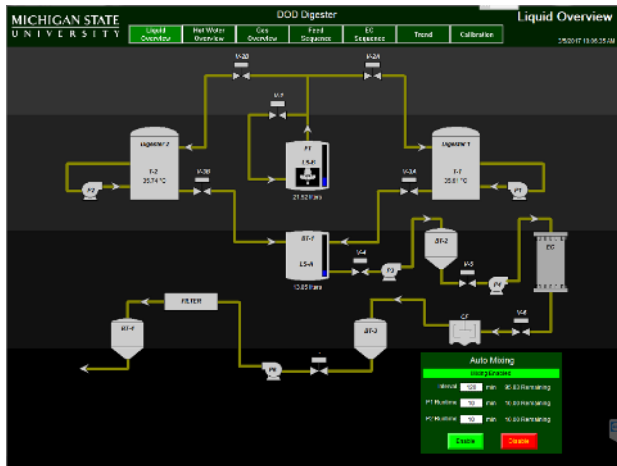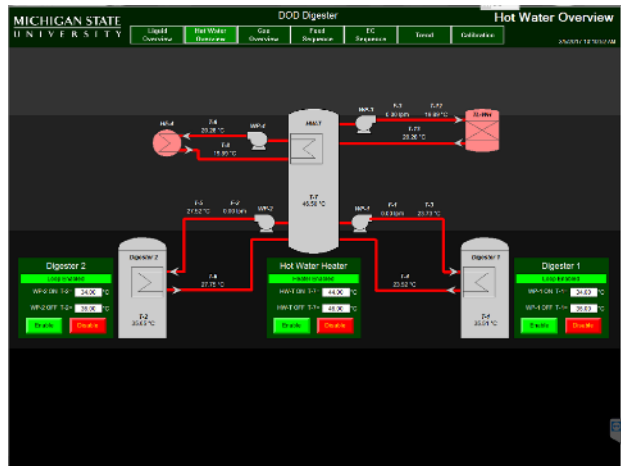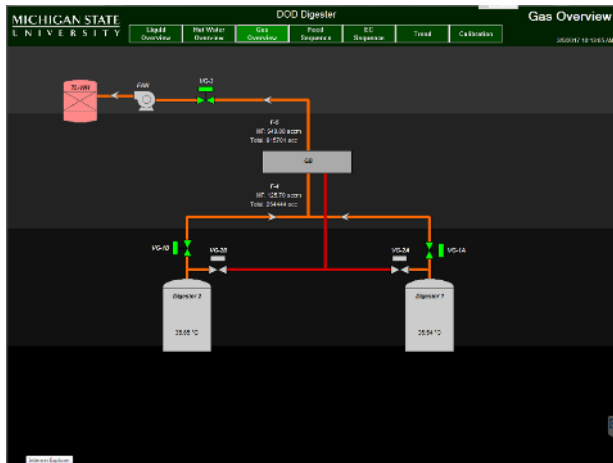|	- Data export to .CSV files - Remote screen control via VNC - Remote file access via FTP

Figure 19. Piping and instrumentation diagram (P&ID) of the system

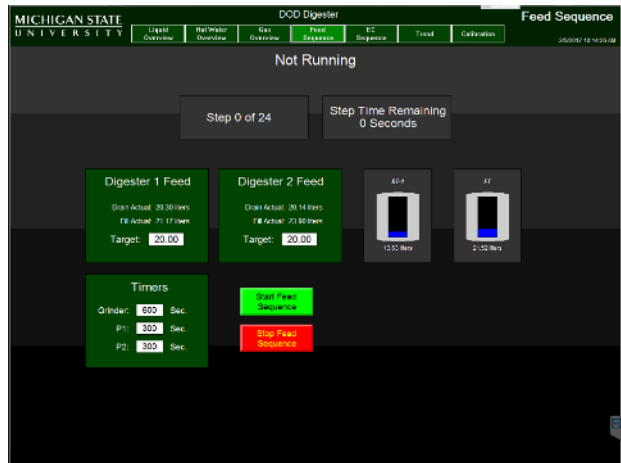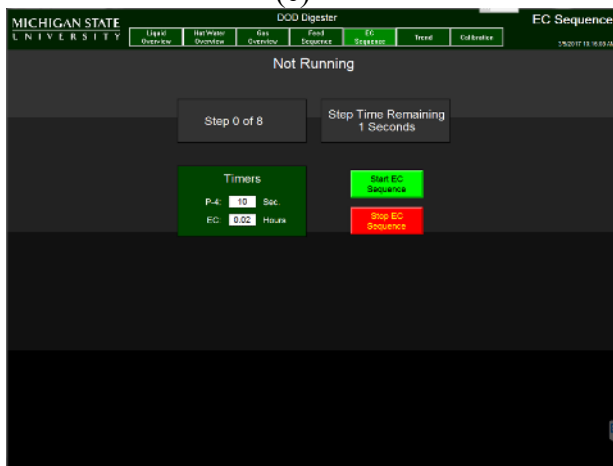(a)   (b)
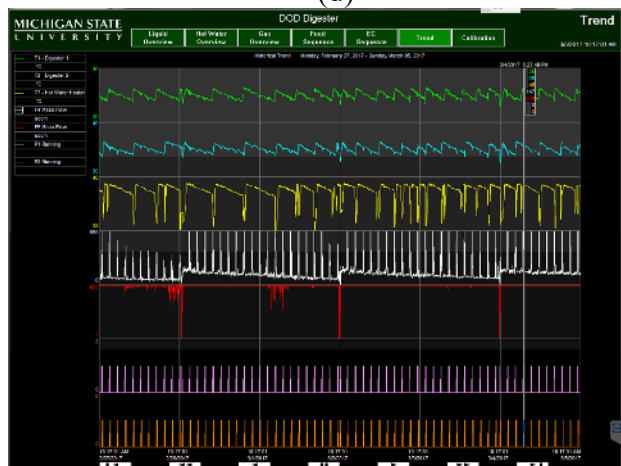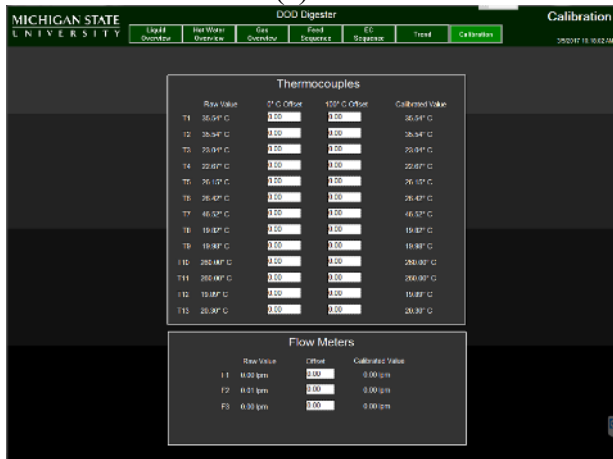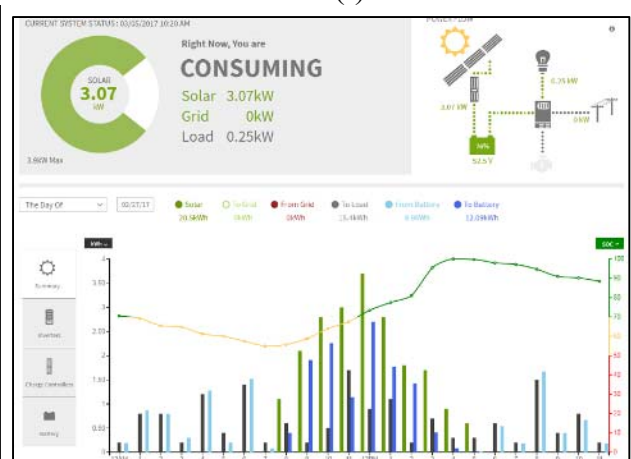
(c)

(d)

(e)

(f)

(g)

(h)

Figure 20. Interface of the control system: (a) Liquid overview; (b) Hot water overview; (c) Gas overview; (d) Feed sequence; (e) EC sequence; (f) Data trend; (g) Calibration; (h) Energy management

3.6 Conducting a detailed technical and economic analysis on the system

The data generated from the pilot operation were used to conduct a technical and economic analysis on the system. Mass and energy balance analyses were carried out based on an expeditionary contingency base with a nominal size of 150 personnel. The base generates 160 kg per day food wastes with a moisture content of 70%. The base also generate 3,000 L black water per day (20 L per soldier per day). The TS of the mixture of food wastes and black water is 1.5%. The system for 150 personnel contingency base is scaled according to the established pilot unit, and includes three operation units of solar energy collection, anaerobic digestion, and water reclamation. Two combinations of unit operations were analyzed for different treatment purposes: **1) PV-AD-EC-aeration for non-potable water generation; and 2) PV-AD-EC-filtration for potable water generation.**

In addition to the technical analysis, economic performance is another important factor to determine the viability of the system. An economic assessment was then conducted for the pilot system. The capital expenditure (CapEx) and operational expenditure (OpEx) of the system were used for the economic assessment. Revenues include fuel and water offset and savings. The Modified Accelerated Cost Recovery System (MACRS) was used to calculate the annual depreciation of CapEx. In addition, an annual inflation of 3% was set for OpEx and revenues based on the five-year average inflation rate. The net cash flow based on depreciated CapEx and inflated OpEx and revenues was conducted to determine the payback period. The parameters used for the economic assessment are described in Table 9.

Table 9. Parameters of the system for technical and economic assessment (150 personnel base)

System components	The system
Feedstock	3160 kg per day with 1.5% TS
Food wastes (kg, with 70% moisture)	160
Black water (L)	3,000
Solar energy collection	
PV panels	24 m^3
Anaerobic digestion	20 m^3
Digester technology	Upflow fixed film anaerobic digestion
Digester size (m^3)	15 (12 m3 effective volume)
Loading rate (m^3/day)	3.16
TS of the feed (g/L)	15
Retention time (day)	4
Reaction temperature (°C)	35
Biogas boiler	Hot water
Water reclamation	
Electrocoagulation reactor size (m^3)	1
Loading rate (m3/day)	3
Processing time (hr)	1
Centrifuge capacity (L/minute)	100
Centrifuge size (kW)	2
Aeration pump (kW)[a]	0.5
Aeration time (hr)[a]	12
Ultra/Nano/RO filtration (L/minute)	20
Labor cost	

Operator	None
Other expense	
Maintenance	Pumps, chemicals, and filters
Bioenergy and water	
Bioenergy	On-site uses to compensate the energy demand
Water	On-site uses to compensate the water usage
Financial analysis	
Inflation rate	3% [b]
Depreciation	MACRS [c]

a. The aeration parameters are for the techno-economic analysis of the PV-AD-EC-aeration combination.
b. The 5-year average local inflation is used as the inflation rate.
c. The depreciation period is set at 10 years. The depreciation is on solar panel, anaerobic digester, and water reclamation (the system installation cost is not included in depreciation). The annual depreciation rates from MARCRS (Modified Accelerated Cost Recovery System) are: 0.100, 0.188, 0.144, 0.115, 0.092, 0.074, 0.066, 0.066, 0.065, 0.065, 0.033, 0.033 (after 10 years).

4. RESULTS AND DISCUSSION

4.1 Designing a novel solar concentrator and engine system on solar and methane heat
4.1.1 Implementing a foldable solar heat collector
4.1.1.1 Solar tracking of the foldable unit

The foldable Fresnel lens solar thermal collector has been operated and tested in East Lansing, Michigan (elevation 262 m, latitude 42°43'27.8" N, longitude 84°28'38.6" W) from July 2013 to October 2013. The operation demonstrates that the two-module structure is easy to unfold and fold for working and rest modes (Figure 2). In the working mode, the pivots with screw pins steadily lock both vertical actuator and receiver on the horizontal actuator and platform respectively, which ensures that the impact of foldable structure on solar tracking and concentration is minimal.

Since the foldable structure at the working mode is fairly steady, the accuracy of the solar tracking is mainly dependent on the movement of Fresnel lens (stepper motors). The calculated decimal position data from the astronomical algorithm must be converted into integer numbers (step numbers of the stepper motors) before being transferred to the step motors. Relatively large step numbers should be used to achieve a high position resolution, which is the reason that the stepper motors with 20000 steps per revolution were selected to move the Fresnel lens collector. In addition, high and low integer step numbers generated by the round function in LabVIEW were able to compensate each other during the operation, which also facilitated reducing the position errors. The experimental data verify that the control system enabled the foldable unit to accurately realize the solar tracking (Figure 21). During the tracking test, differences on azimuth and zenith angles between the lens and real sun positions were 0.221° ± 0.238° and 0.025° ± 0.019°, respectively, which were relatively small and had no significant influence on solar thermal collection.
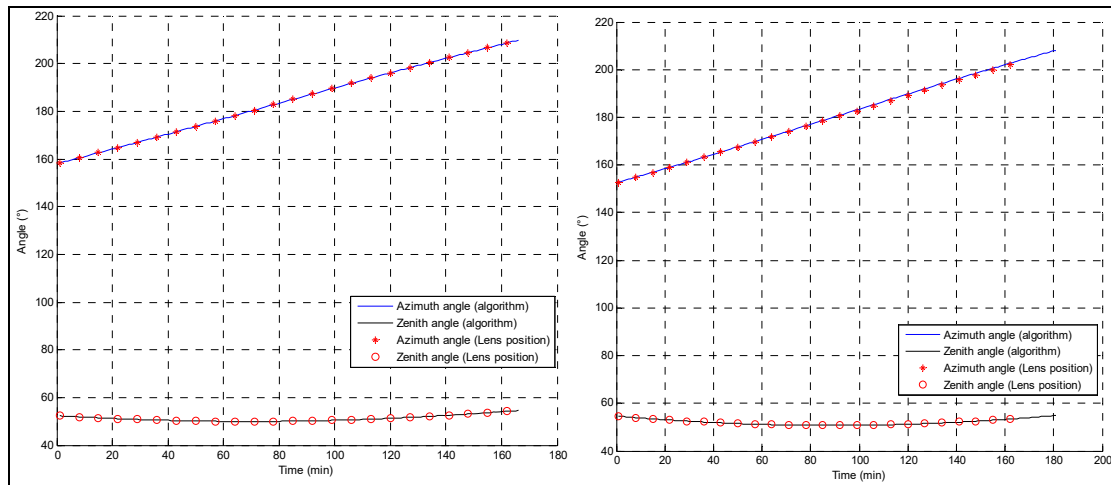
Figure 21. Topocentric azimuth and zenith angle of the Fresnel lens position during the solar tracking at two different dates*

*: The left graph is for the test on 10/11/2013, and the right graph is for the test on 10/13/2013.

4.1.1.2 FEM simulation and verification of temperature profile of thermal absorbers

Solar radiation and receiver column temperature (inside the receiver) were measured and used for FEM simulation (Table 10). The FEM simulation results are presented in Table 11 and

45

Figure 22. The data demonstrate that under the same operational conditions (ambient temperature and solar radiation), the larger CRs the higher the temperatures at the center of the absorber were. However, the increase of temperature was not proportional to the increase of CR or decrease of absorber area. For instance, once the CR was increased from 256 to 1000, the temperatures were only increased by 3.49%, 4.85%, and 6.28% for absorber areas of 1.5 x 1.5 in, 2 x 2 in, and 2.5 x 2.5 in, respectively. While, compared to the temperature response to the CR changes, absorber temperatures were more dramatically changed regarding the size change of absorbers. Once the absorber area was decreased from 2.5x2.5 in to 1.5x1.5 in, the temperatures at the center of absorber was increased by 36.75%, 37.00%, and 33.16% for concentration ratios of 256, 576, and 1000, respectively.

Table 10. Solar radiation and receiver column temperature for the FEM model*

CR	Area (in x in)	Solar radiation (W/m^2)	Number of measurements	Inside receiver temperature (°C)	Number of measurements
256	1.5x1.5	633.17±18.66	163	204.36±36.35	11
	2x2	674.16±5.19	106	217.00±21.33	9
	2.5x2.5	679.54±5.22	107	181.67±31.40	9
576	1.5x1.5	622.48±15.13	85	256.80±9.20	5
	2x2	665.78±7.11	69	274.20±15.80	5
	2.5x2.5	650.63±14.32	94	209.40±14.72	5
1000	1.5x1.5	616.72±23.53	86	301.80±7.98	5
	2x2	666.82±4.49	81	278.60±15.97	5
	2.5x2.5	670.64±4.37	73	241.75±24.51	4

*: Data are average of multiple measurements with standard deviation.

Table 11. Temperature at the center the absorbers and statistical comparison

| CR	Area (in x in)	Temperature from the FEM model (°C)	Measured temperature (°C)	Number of measurements	One-sample t-test t value	p value
256	1.5x1.5	592.94	564.49±38.75	163	4.643	> 0.1
	2x2	508.76	531.79±51.67	106	2.819	> 0.1
	2.5x2.5	433.58	410.79±31.36	107	4.596	> 0.1
576	1.5x1.5	603.83	633.28±13.17	85	14.143	> 0.1
	2x2	525.70	533.94±24.17	69	1.983	> 0.1
	2.5x2.5	440.74	418.66±24.20	125	5.771	> 0.1
1000	1.5x1.5	613.65	-	-		
	2x2	533.44	-	-		
	2.5x2.5	460.83	-	-		
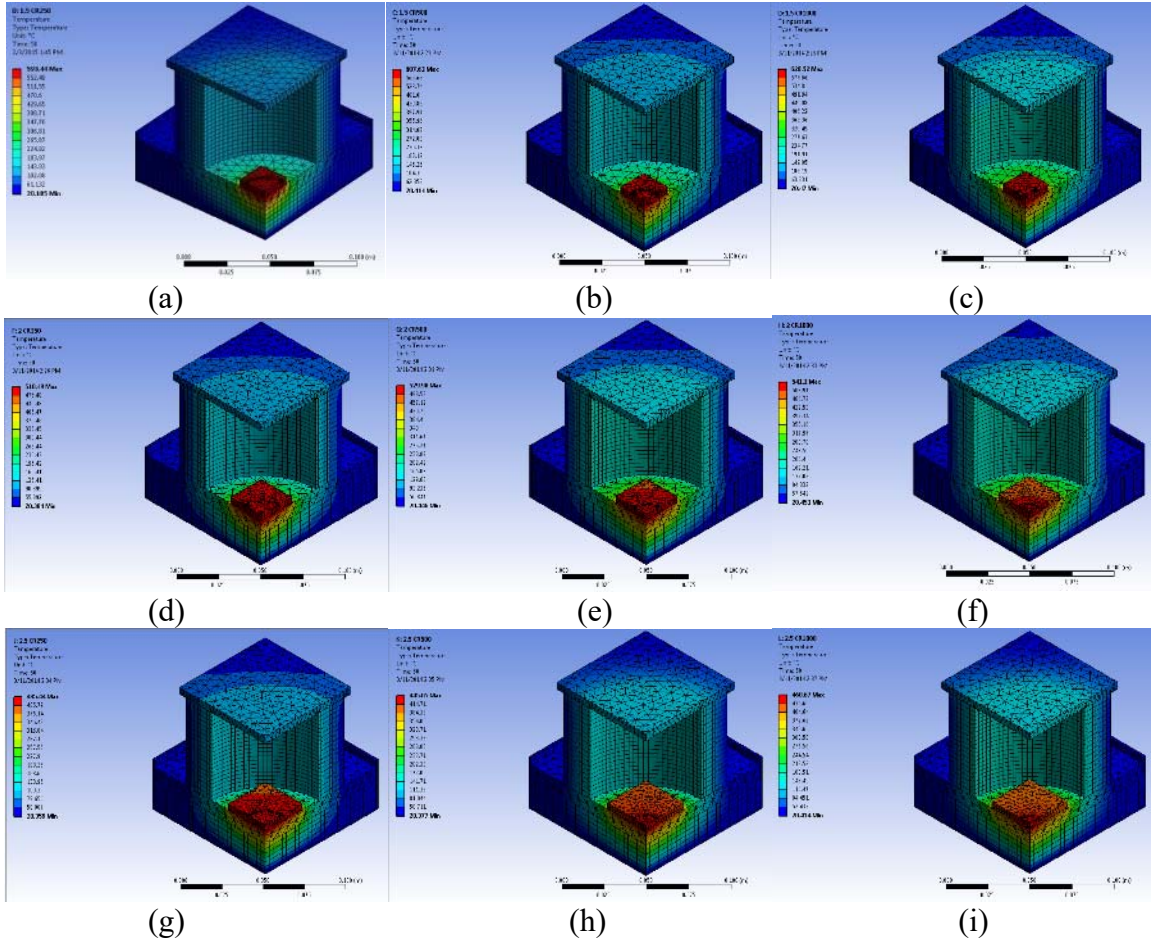
Figure 22. Temperature profiles obtained using FEM simulation.
(a)1.5 X 1.5 in^2 A_a, 256 CR, (b)1.5 X 1.5 in^2 A_a, 576 CR, (c) 1.5 X 1.5 in^2 A_a, 1000 CR, (d) 2 X 2 in^2 A_a, 256 CR, (e) 2 X 2 in^2 A_a, 576 CR (f) 2 X 2 in^2 A_a, 1000 CR (g) 2.5 X 2.5 in^2 A_a, 256 CR (h) 2.5 X 2.5 in^2 A_a, 576 CR (i) 2.5 X 2.5 in^2 A_a, 1000 CR

As for temperature distribution in the absorber, the ratio of concentration area (A_c) to absorber area (A_a) should be close to 1 in order to achieve a homogenous temperature profile. However, it is difficult to achieve such high ratio for most of reflective and refractive solar thermal collectors. It is even more-difficult for the studied foldable unit to use high A_c/A_a ratios due to the fact that the focal distance between the lens and receiver is achieved by multiple mechanical movements. High A_c/A_a ratios require extreme accuracy of the movement which is very hard to achieve. Therefore, the A_C/A_a ratios of the studied foldable collector were changed between 0.042 and 0.454 (Table 12). The simulation results indicate that temperature gradient occurred to all combinations of CR and absorber area (Figure 22). Temperature difference between the center and corners of absorbers increases with increase of A_c/A_a ratio (Tables 11 and 13). Percentages of the temperature difference are 3.19%, 4.63%, and 5.54 % at the CR of 256 for absorbers of 1.5 x 1.5 in, 2 x 2 in, and 2.5 x 2.5 in. Corresponding percentages of the temperature differences for the three absorbers are 5.16%, 6.87%, and 8.07 % at the CR of 576, and 7.27%, 9.13%, 10.48% at the CR of 1000 CR. The smallest difference of 3.19% was from the 1.5 x 1.5 in absorber and the CR of 256 with an A_C/A_a ratio of 0.454, and the largest

47

difference of 10.48% was from the 2.5 x 2.5 in absorber and the CR of 1000 with an A_C/A_a ratio of 0.042.

The simulation results were verified using thermocouple and thermal camera to measure temperatures of the absorbers for two concentration ratios of 256 and 576 (Table 11). A one-sample t-test concluded that all measurements were in the 90% confidence interval of the model results (Table 11).

Table 12. A_C/A_a ratios for different CRs and absorber areas

CR	Absorber area (in x in)		
	1.5 x 1.5	2 x 2	2.5 x 2.5
256	0.454	0.255	0.163
576	0.202	0.114	0.073
1000	0.116	0.065	0.042

Table 13. Simulated corner temperature for absorbers (°C)

Absorber (in x in)	Concentration ratio (CR)		
	256	576	1000
1.5x1.5	574.00	575.90	579.68
2x2	482.51	489.56	490.39
2.5x2.5	402.06	400.50	412.54

4.1.1.3 Optimization of concentration area and surface temperature

Solar thermal collectors are intended to transfer as much as solar energy via a receiver to various heat applications. It is apparent that the high surface temperature and large absorber area are two key factors to determine quality and quantity of the heat transfer of solar radiation. However, these two factors are oppositely related at a given lens area (fixed solar radiation). According to the discussion in the previous sections, the increase of the surface temperature can only be achieved by reducing the absorber area. In addition, heat losses (i.e., radiation and convection heat losses) of the absorber are also associated with absorber area and surface temperature, which further influences the net heat flux on the absorber. Therefore, relationship of surface temperature, absorber area and heat loss should be evaluated to conclude optimal conditions for Fresnel lens collector to maximally transfer solar thermal energy.

A incident heat radiation model that described heat flux in a metallic plate as a function of its temperature was used to delineate the relationship between heat flow and surface temperature of the absorber [67]. The mathematical expression of the incident heat radiation model is:

$$\epsilon_m(q_o'' - \sigma T_a^4) + h(T_\infty - T_a) + K_{PT}(T_\infty - T_a) = C_{PT}\frac{dT_a}{dt} \tag{29}$$

Where q_o'' is the incident heat flow, σ is the Stefan-Boltzmann constant, T_a is the absorber temperature, h is the convection coefficient, T_∞ is the temperature of the ambient environment where the absorber is located, K_{PT} is the combined effect of conduction and convective cooling on insulation, and C_{PT} is the overall heat capacity of the absorber and a portion of the insulation. At steady state, the term $\frac{dT_m}{dt}$ is equal to zero, and then the model presented that the inflow q_o'' is a function of the temperature of the absorber.

Integrating the results from both incident heat radiation model and FEM analysis delineates the relationship of heat loss, surface temperature and absorber area (Figure 23). Heat loss and absorber temperature were decreased with the increase of absorber area, and decrease of the heat loss was much faster than the absorber temperature. Since the absorber temperature was linearly changed with absorber area in the experimental range, the heat loss was used to determine the optimal absorber area that can achieve high absorber temperature with minimum heat loss. The optimal absorber area is defined as the area where the rate of corresponding heat loss started leveling off. Turning point analysis was applied on the heat loss curve in the experimental range (absorber area between 0.0015 and 0.004 m^2). The analysis concluded that the optimal absorber area is 0.00274 m^2 for the studied unit. At the optimal absorber area, the minimum possible heat loss of 16.90 kW/m^2 absorber area and a relatively high absorber temperature of 512.6°C were achieved correspondingly.
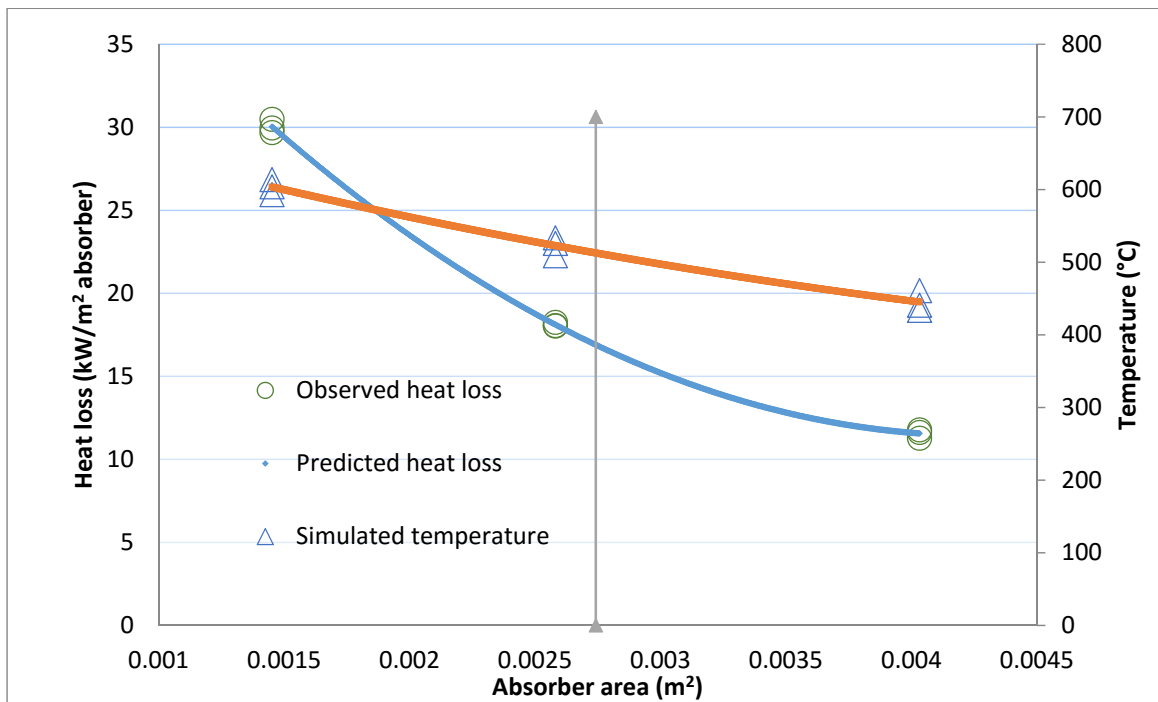

Figure 23. Turning point for the predicted absorber temperature and heat loss as function of absorber area (A_a)

The experimental results demonstrates that the two-module structure can be used to develop foldable Fresnel lens thermal collectors for small- and medium-solar power generation. With selection of high resolution stepper motors, the bench-scale foldable solar collector can accurately realize the solar tracking. FEM simulation of thermal absorber demonstrates that the absorber area impacts more on the surface temperature of the absorber than concentration ratio. An optimization approach using combination of incident heat radiation model and FEM simulation concluded that the optimal absorber area for the studied unit was 0.00274 m^2, and the corresponding absorber temperature and heat loss were 512.57 °C and 16.90 kW/m^2 absorber area.

4.1.2   Solar thermal receivers
4.1.2.1 Computational fluid dynamics (CFD) modeling solar receivers

Synthetic oil (Dowtherm A) was selected as the working fluid. Energy from solar radiation was transferred to the oil used for steam generation. A micro-turbine of 1.4 kW [59] was selected as the power generation unit. The operational parameters of the micro-turbine were used to carry out the calculation and receiver modeling. This particular turbine needs superheated steam at 180–220 °C and 8–10 bar. The temperature of the feeding water was 45 °C. In the model, the temperature change of the synthetic oil due to the solar radiation was set in the range of 220–250 °C. The ambient conditions (average direct normal irradiance (DNI) (Figure 24)) in Lansing were used as the environmental parameters to run the simulation, and average wind velocities were used to calculate the convection heat loss.
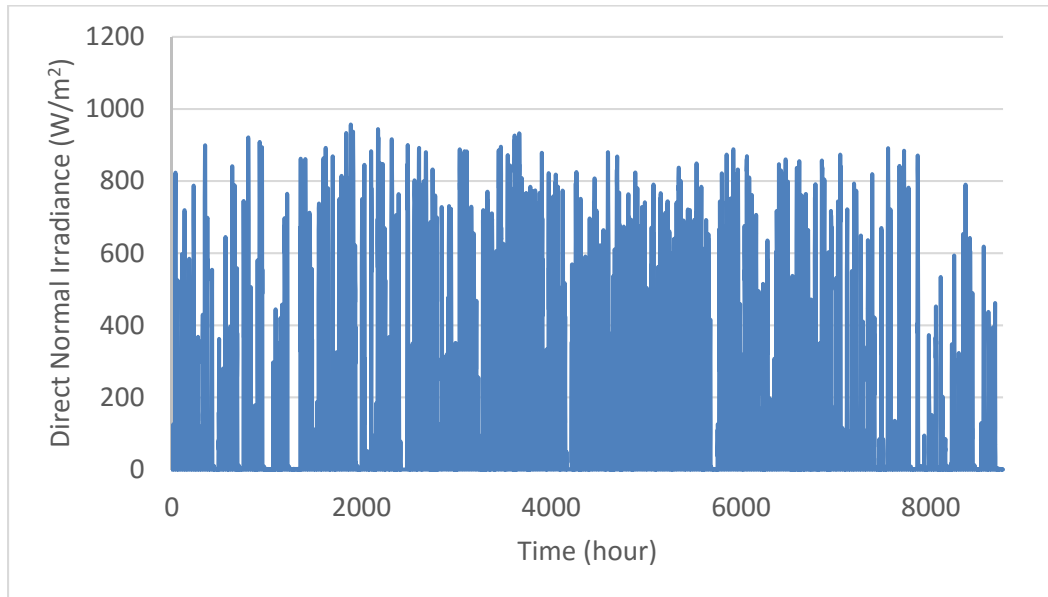

Figure 24. DNI during a year at Lansing, MI

Simulation CFD software [68] was used to carry out the analysis. Both receivers were discretized, and the mesh size was tested using a heat input value (with no heat losses). The heat input must be completely transferred to the fluid, and the corresponding fluid outlet temperature can be calculated. Using the correlation $Q = \dot{m} \cdot C_p \cdot \Delta T$, where mass flow, heat capacity, and temperature difference are known, the absorbed heat was calculated and compared with the heat input. The difference between the heat input and the absorbed heat was set at less than 1%. The analysis used the K-epsilon to model turbulent flow. The outlet working fluid temperature and heat transfer efficiency under steady-state receiver operation for two oil mass flows (5 g/s and 10 g/s) and three DNI values (750 W/m², 940 W/m², and 1125 W/m²) were then determined.

Since Fresnel lenses were the targeted solar thermal collection technology, optical efficiencies for the lens and the thermal glass were considered for the total heat flux receiver in the absorber area. The transmittances for the Fresnel lens and thermal glass reported by the manufacturers were 0.92 and 0.90, respectively. The DNI was then adjusted to the losses in the transmittance for the glass and the lens. Moreover, heat losses due to convection and radiation were taken into account for the external receiver surfaces. The calculation of the heat loss due to forced convection included the wind velocity (4.69 m/s (annual average at Lansing) and 2 m/s

50

(the wind velocity reduced by a screen installation to cover the refractive collector sides)). The heat loss due to convection was calculated according to the Newton's law of cooling:

$$Q_c = h \cdot A \cdot (T_s - T_\infty) \tag{30}$$

where Q_c is the heat loss due to convection (W); h is the convective coefficient (W/m²·°C); A is the surface in contact with the external air (m²); T_s is the surface temperature (°C); and T_∞ is the ambient temperature (20 °C). Furthermore, the convective coefficient was calculated as

$$h = \frac{Nu \cdot k}{D} \tag{31}$$

where Nu is the Nusselt number; k is the ambient air thermal conductivity (W/m·°C); and D is the characteristic length for the receiver geometry (m) (outside diameter). The dimensionless Nusselt number was calculated using the empirical correction for cylinders [69]:

$$Nu = 0.027 \cdot Re^{0.805} \cdot Pr^{1/3} \tag{32}$$

$$Re = \frac{V \cdot D}{v} \tag{33}$$

where Re is the Reynolds number; Pr is the Prandtl number; V is the wind velocity (m/s); and v is the ambient air viscosity (m²/s). Table 14 summarizes the calculation of the convective heat transfer coefficient.

<div align="center">Table 14. Convective coefficient for heat loss</div>

Parameter	Cavity absorber	Conical absorber
Diameter (mm)	409.58	361.95
Height (mm)	122.56	206.38
Wind speed (m/s)	2 4.69	2 4.69
T_∞ (°C)	20	20
T_s assumed (°C)	45	45
v (m²/s) @ T_s	1.75×10^{-5}	1.75×10^{-5}
Re	4.68×10^4 1.10×10^5	4.14×10^4 9.70×10^4
Pr @ T_∞	0.7323	0.7323
Nu	227.0 468.4	204.4 421.8
k (W/m·°C) @ T_∞	0.02476	0.02476
h (W/m²·°C)	13.723 28.319	13.98 28.856

In addition to the convective heat loss, the energy losses of solar receivers due to radiation can be calculated as

$$Q_R = \varepsilon \cdot \sigma \cdot A \cdot \left(T_s{}^4 - T_\infty{}^4\right) \tag{34}$$

where ε is the material emmisivity; σ is the Stefan-Boltzmann constant (W/m^2·K^4); A is the surface area (m^2); and T_s and T_∞ are the surface and ambient temperature, respectively. The conical receiver material consisted of aluminum, with an emissivity of 0.18, and the cavity receiver had a emissivity of 0.27 (that of stainless steel) [55]

Both receiver designs allowed the refractive Fresnel lens to concentrate 750 times solar radiation into the absorber area (1,333.33 mm^2). A homogenous distribution of input heat in the absorber area is assumed as the boundary condition in the CFD analysis.

4.1.2.2 Testing the solar receivers
The fluid temperature at the outlet of the receivers was significantly influenced by different values of DNI, working fluid mass flows, and wind velocities. When the wind velocity changed from 2 m/s to 4.69 m/s, the convective factor increased from 13 W/m^2·°C to 28 W/m^2·°C (Table 14). In addition, the CFD results show that, for a mass flow of 5 g/s, when the wind velocity changed from 2 m/s to 4.69 m/s, the heat transfer efficiencies for cavity absorbers decreased from 57.92% to 48.11%, respectively; while that for conical absorbers decreased from 61.09% to 51.92%, respectively (Table 15). For a high mass flow of 10 g/s, when the wind velocity changed from 2 m/s to 4.69 m/s, the heat transfer efficiencies for cavity absorbers decreased from 51.91% to 45.37%, respectively, and for conical absorbers from 53.74% to 46.88%, respectively (Table 15). Although the heat transfer efficiencies for a high mass flow were significantly lower than those for a low mass flow, the changes in the heat transfer efficiencies corresponding to the increase in convective factor were smaller than those for the low mass flow. For the high mass flow, the changes in the heat transfer efficiencies for the cavity and conical absorbers were 6.54% and 6.86%, respectively, while the corresponding changes for the low mass flow were 9.81% and 9.17%, respectively. In addition, there were no significant differences in the final working fluid temperature between the two absorbers for the same wind velocity and mass flow (Table 15).

Table 15. Heat transfer efficiency for wind velocity variation

Receiver	Cavity absorber				Conical absorber			
Wind velocity (m/s)	4.69	2	4.69	2	4.69	2	4.69	2
Mass flow (g/s)	5	5	10	10	5	5	10	10
T initial (°C)	220	220	220	220	220	220	220	220
T final (°C)	248	253.71	235.11	237.78	246.41	250.21	233.64	235.64
Q absorbed (W)	298.76	359.65	322.4	379.36	281.76	322.38	291.12	333.74
Transfer efficiency	48.1%	57.9%	51.9%	61.0%	45.4%	51.9%	46.9%	53.7%

The DNI is the most critical parameter that has an effect on the thermal transfer efficiency and working fluid temperature. An increase in the net DNI can significantly improve the solar thermal collection for both receivers. When the net DNI increased from 621 W to 931 W, the

thermal transfer efficiency of the cavity receiver increased from 58% to 68% for a mass flow of 5 g/s, and from 61% to 72% for a mass flow of 10 g/s. The corresponding increase for the conical absorber was from 52% to 66% for a mass flow of 5 g/s, and from 54% to 68% for a mass flow of 10 g/s (Figure 25). Comparing the impact of change of net DNI on heat collection efficiencies, those of the conical receiver (single path) were affected more than those of the cavity receiver (multiple paths).
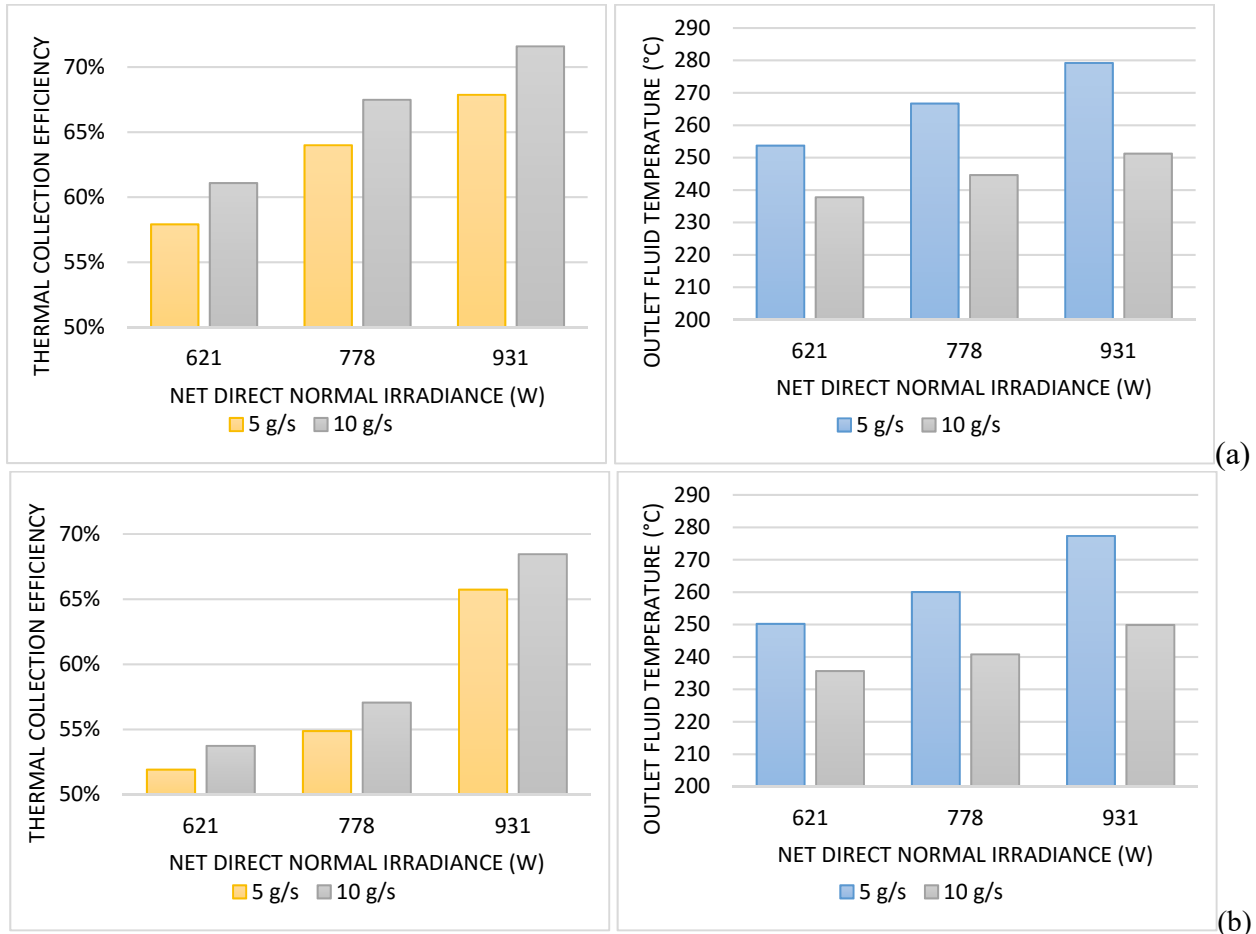

(a)

(b)

Figure 25. Thermal collection efficiency and fluid output temperature of the receivers for two fluid mass flows: (a) cavity absorber; (b) conical absorber

Tables 16 and 17 summarize the results from the CFD analysis for both cavity and conical receivers, and Figure 26 shows the fluid temperature profile for selected scenarios. For the conditions of a net DNI of 931 W and the lower mass flow of 5 g/s, the maximum temperatures of the working fluid were 582.31 °C and 399.19 °C for the cavity and conical receivers, respectively.

(a)

(b)

(c)

(d)
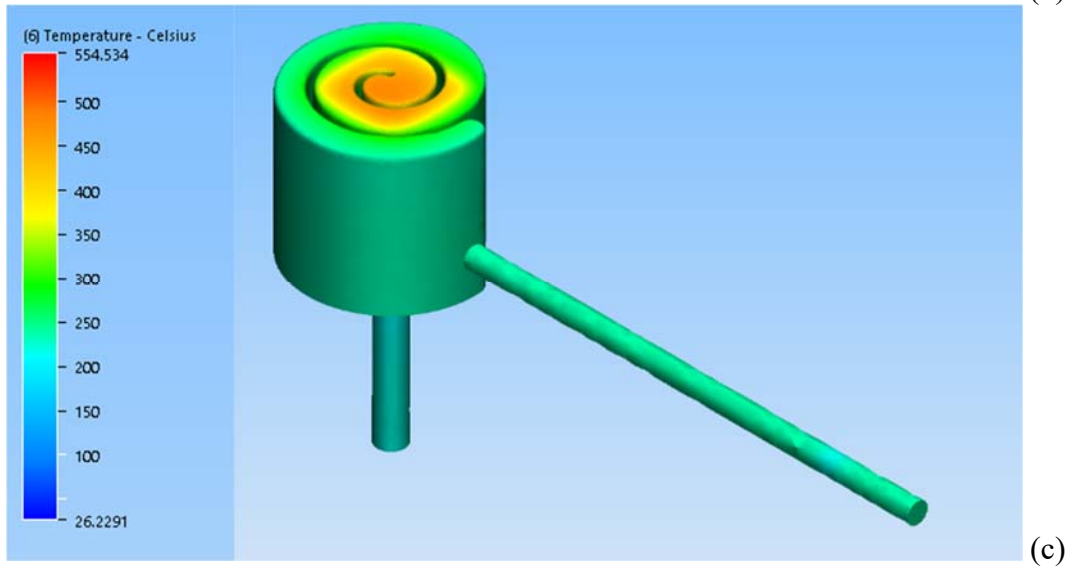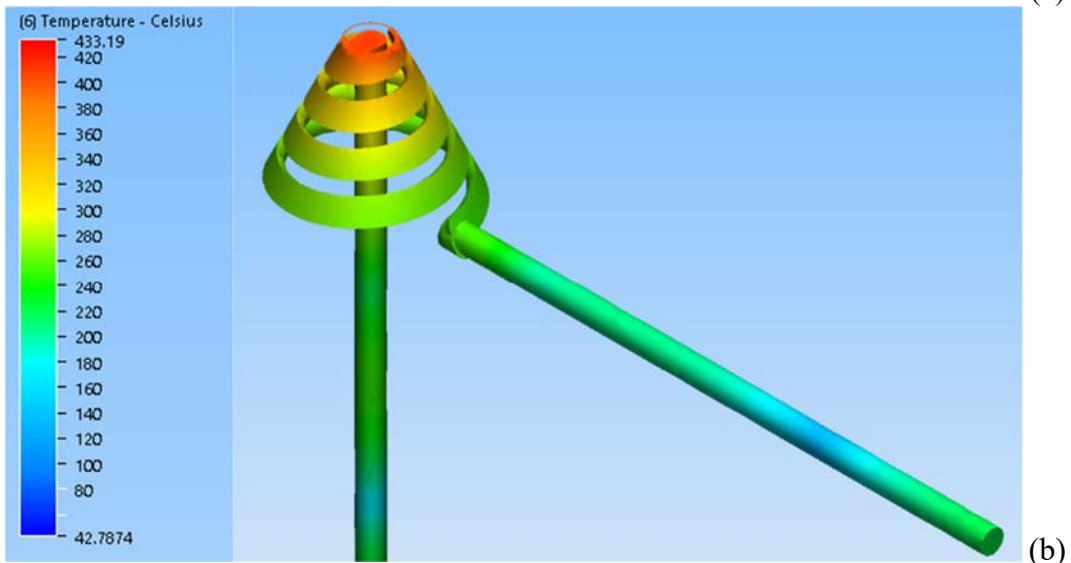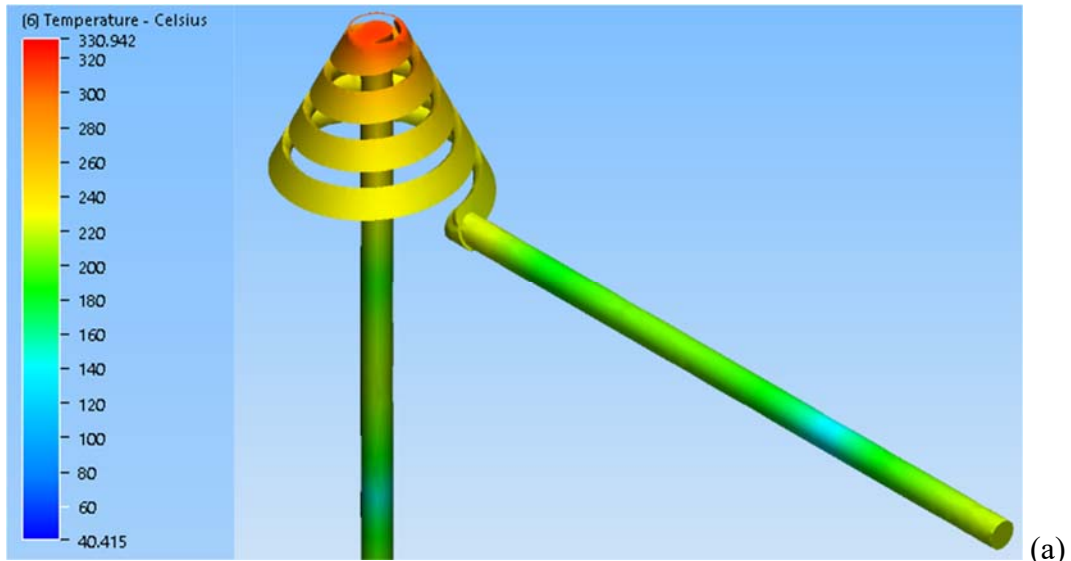
Figure 26. Fluid temperature distribution in the studied receivers for selected scenarios. conical receiver: (a) 621 W at 10 g/s, (b) 931 W at 5 g/s; cavity receiver: (c) 621 W at 10 g/s, (d) 931 W at 5 g/s

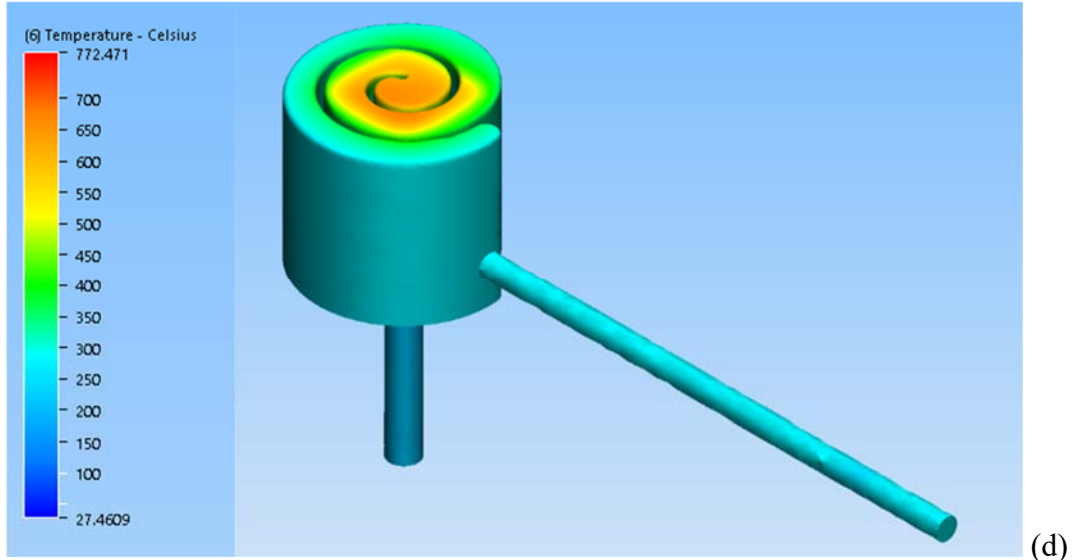Since the synthetic oil (Dowtherm A) used by this paper has a maximum operating temperature of 400 °C, the maximum temperature for the cavity receiver exceeds the limit of the synthetic oil. Due to the multiple paths in the spiral hole, the fluid molecules around the heating surface have a longer residence time, increasing their temperature much higher than the average, which could cause a dangerous degradation of the synthetic oil. Reduction of the concentration ratio (CR) and increase of the mass flow of the working fluid can be used to limit the maximum temperature that the fluid reaches. By reducing the CR by half (to CR = 375), the surface absorber temperature decreases from 772.72 °C to 516.70 °C, which limits the maximum working fluid temperature to 474.70 °C, still exceeding the recommendation for the synthetic oil. However, since the cavity absorber has multiple paths for the working fluid, the temperature profile is not evenly distributed on the surface. The cavity absorber has zones with low velocities near the heating surfaces (hot spots), which lead to an uneven heating and a high working fluid temperature at these spots (exceeding the temperature limit of the synthetic oil) even at the low CR. As mentioned previously, a low CR and high fluid mass can reduce the thermal transfer efficiency. Therefore, the conical (single path) absorber, which has a relatively homogenous temperature distribution in the working fluid, represents a preferable design for the solar thermal receiver.

Table 16. The effects of DNI on the conical absorber

Parameter	Value					
Direct normal Irradiance (W)	621	621	778.3	778.3	931	931
Wind velocity (m/s)	2	2	2	2	2	2
Mass flow (g/s)	5	10	5	10	5	10

55

T initial (°C)	220	220	220	220	220	220
T final (°C)	250.2	235.6	260.0	240.8	277.4	249.9
Cp (J/kg·°C)	2,134	2,134	2,134	2,134	2,134	2,134
Q absorbed (W)	322.4	333.7	427.1	444.1	612.0	637.3
Transfer efficiency	51.9%	53.7%	54.9%	57.1%	65.7%	68.5%

Table 17. Effects of DNI on the cavity absorber

Parameter	Value					
Direct normal Irradiance (W)	621	621	778.3	778.3	931	931
Wind velocity (m/s)	2	2	2	2	2	2
Mass flow (g/s)	5	10	5	10	5	10
T initial (°C)	220	220	220	220	220	220
T final (°C)	253.7	237.8	266.7	244.6	279.2	251.2
Cp (J/kg·°C)	2,134	2,134	2,134	2,134	2,134	2,134
Q absorbed (W)	359.7	379.4	498.1	525.2	631.8	666.5
Transfer efficiency	57.9%	61.1%	64.0%	67.5%	67.9%	71.6%

Two solar thermal receiver designs have been presented. The receiver with the cavity absorber, which has multiple paths and provides a longer residence time of the working fluid, presents a higher thermal transfer efficiency than the receiver with conical absorber, which has a single path and provides a short residence time of the working fluid. However, the cavity absorber has hot spots, where the high working fluid temperature at the spots exceeds the temperature limit of the synthetic oil. Reducing the concentration ratio and increasing the mass flow can solve the issue, although the fluid outlet temperature is reduced correspondingly. The receiver with the conical absorber demonstrates similar thermal efficiencies to the cavity receiver and avoids the adverse effects of low local velocities that the cavity receiver encounters. Therefore, the conical absorber represents a preferable design to collect solar thermal energy considering the currently available synthetic oil.

4.1.3 Comparison of Brayton and Rankine cycles for small-scale solar-bio-hybrid power generation

4.1.3.1 Relationship between solar energy, capacity factor, and ratio of solar energy to biomethane energy

The biomethane consumption of solar–bio hybrid power systems (steam and gas turbines) depends on the usage of solar energy (the heat input from solar energy) and the net capacity factor of the power generation. The effects of capacity factor and solar usage on bioreactor volume and solar energy requirements for solar–bio hybrid steam and gas turbine systems are presented in Figure 27. With an increase in net capacity factor and solar usage, the solar energy demands of both systems linearly increase. At the same time, the hybrid steam engine system demands more solar energy than the hybrid gas turbine system (Figure 27 a and b). During full utilization of solar energy (100% solar usage and 1 net capacity factor) to power the hybrid systems, the hybrid steam turbine system requires 18,017 MJ/day of solar energy, which is approximately double the demand of the hybrid gas turbine system (9299.4 MJ/day). Meanwhile, the required bioreactor volume to generate biomethane for 30 kW electricity generation increases with an increase in net capacity factor and decrease in solar usage for both systems, and the hybrid steam engine system requires a larger bioreactor volume than the hybrid gas engine system (Figure 27 c and d). At the point of 0% solar usage and a net capacity factor of 1, the hybrid steam engine system requires a bioreactor volume of 1,435.3 m^3, while the hybrid gas turbine only requires a bioreactor volume of 642.53 m^3.

(a)   (b)
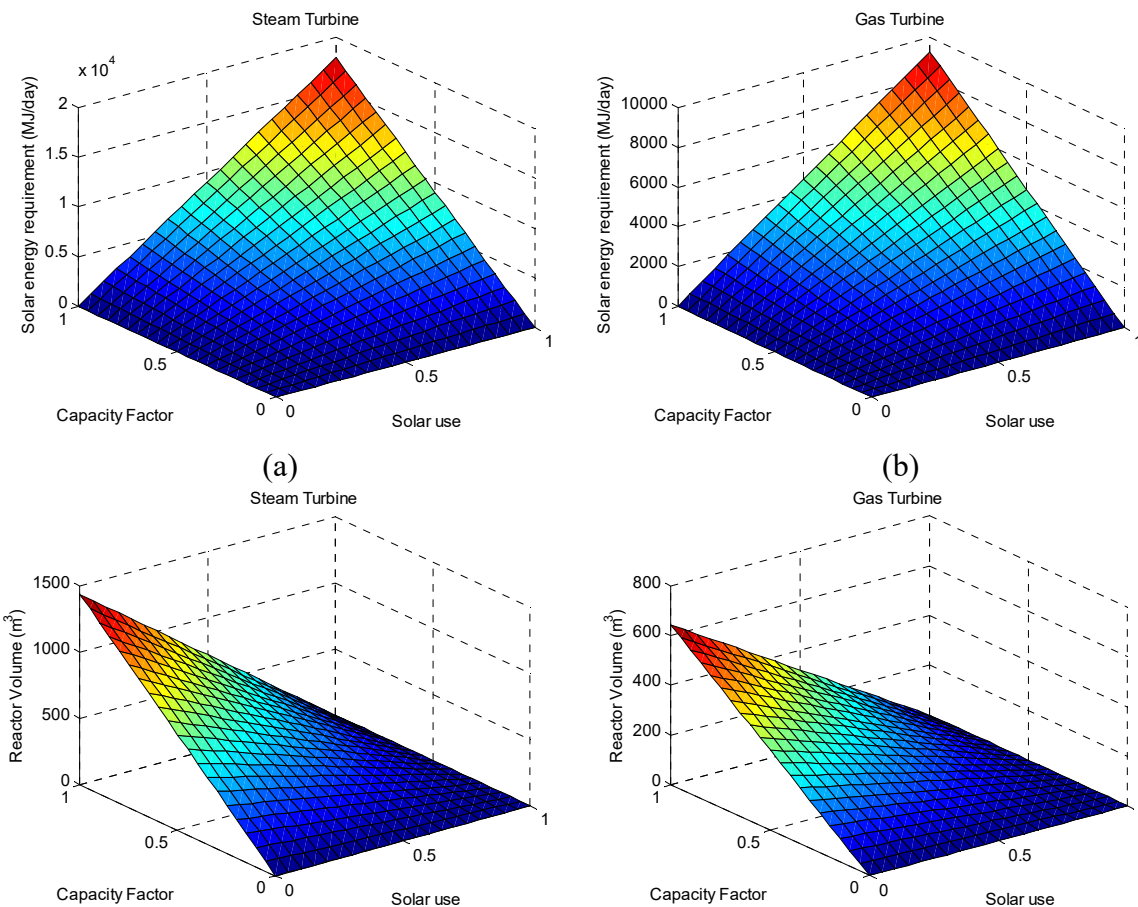
Figure 27. Effects of net capacity factor and solar usage on bioreactor volume and solar energy requirements for different solar–bio hybrid systems*

*: (a) Solar energy requirements for the solar–bio hybrid steam turbine system; (b) solar energy requirements for the solar–bio hybrid gas turbine system; (c) bioreactor volume for the solar–bio hybrid steam turbine system; (d) bioreactor volume for the solar–bio hybrid gas turbine system.

4.1.3.2 Energy requirements for biomethane production
4.1.3.2.1   Thermal energy requirements for biomethane production

Thermal energy is needed by the anaerobic digestion of biomethane production to heat the feed and maintain the culture temperature at 50 °C. The energy requirement per day (E_{req} (MJ/day)) is calculated as follows [70]:

$$E_{req} = \frac{V_{AD}}{HRT} \cdot \rho_{inf} \cdot C_p \cdot \left(T_{AD} - T_{inf}\right) \cdot (1 + 30\%)/10^6 \qquad (35)$$

where V_{AD} is the digester volume (m³); HRT is the hydraulic retention time (days); ρ_{inf} is the feed density (1220 kg/m³); C_p is the feed specific heat (3606 J/kg·°C); T_{AD} is the culture temperature (50 °C); T_{inf} is the feed temperature and assumed to be the same as that for ambient temperature when the ambient temperature is above 4 °C (the feed temperature is set at 4 °C when the ambient temperature is below 4 °C); and 30% is the additional heat that is needed to maintain the thermophilic culture condition of the digester.

The maximum thermal energy demands at Lansing on the coldest winter day under the conditions of a net capacity factor of 1 without solar utilization for steam and gas turbines are 18,880 MJ/day and 8451.9 MJ/day, respectively. The corresponding thermal energy demands at Phoenix for steam and gas turbines are 15,186 MJ/day and 6,798.2 MJ/day, respectively. To satisfy the requirements of year-round power generation, the solar–bio hybrid system should have a positive energy balance on the coldest winter days. Thus, the maximum thermal energy demands at the two locations were used to determine the size of the solar unit and anaerobic bioreactor for 30 kW electricity output.

The solar utilization value was selected based on the balance between thermal energy required by the anaerobic digester and thermal energy generated in the power generation system at a given net capacity factor. The thermal energy generated in the power system (MJ/day) is calculated as follows:

$$E_{th}{}^G = \frac{Q_H{}^* \cdot CF \cdot (24 \cdot 3600)}{1000} \qquad (36)$$

where $Q_H{}^*$ is the heat generated ($Q_H{}^G$ or Q_H) (kW) and CF is the net capacity factor. The energy requirements per day (E_{req} (MJ/day)) given by Equation 35 can also be expressed as

$$E_{req} = \frac{V_{CH4}}{\eta_{CH4} \cdot HRT} \cdot \rho_{inf} \cdot C_p \cdot \left(T_{AD} - T_{inf}\right) \cdot (1 + 30\%)/10^6 \qquad (37a)$$

$$V_{CH4} = \frac{E_{CH4}}{HC} \qquad (37b)$$

$$E_{CH4} = \frac{Q^* \cdot (1-SU) \cdot (CF \cdot 24 \cdot 3600)}{1000} \qquad (37c)$$

where V_{CH4} is the biomethane requirement (m³); η_{CH4} is the biomethane productivity (m³CH4/m³digester); E_{CH4} is the energy provided by the biomethane (MJ/day); HC is the heat of combustion of methane ($HC = 34$ MJ/m³); Q^* is the heat input (Q_F or $Q_F{}^G$) (for the turbine) (kW); and SU is the solar utilization factor. Substituting Eq. 37b and Eq. 37c into Eq. 37a, and combining with Eq. 36, the solar utilization factor can be calculated.

For instances of a given net capacity factor of 0.5, the relationship between solar utilization and the required thermal energy by the AD is shown in Figure 28. To satisfy the energy demands of heating the influent and maintaining the digestion temperature, the solar utilization required at Lansing for steam and gas turbines is 0.3840 and 0.5349, respectively; and the corresponding values at Phoenix for steam and gas turbines are 0.2341 and 0.4217, respectively. These values at the capacity factor of 0.5 are used as the base numbers to select the anaerobic digester volume and solar collector for each location and power system (Table 18).
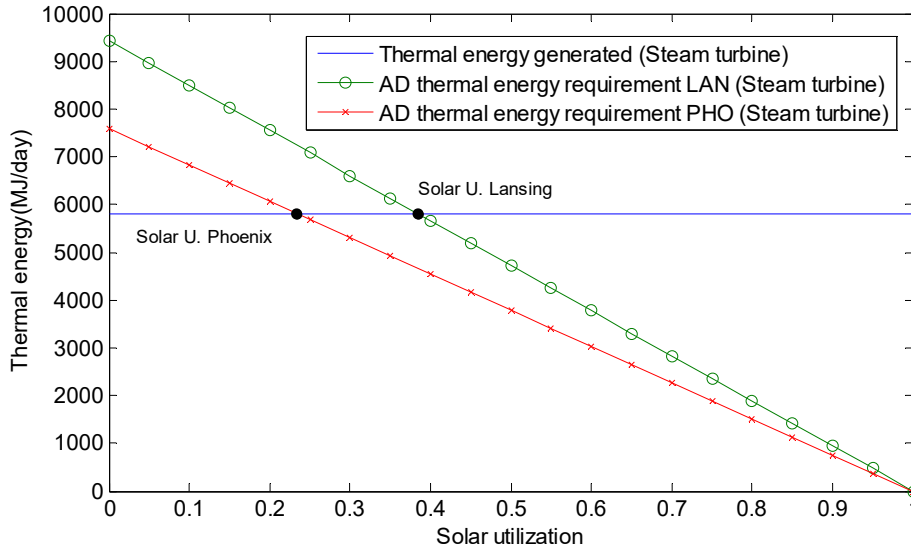
(a)
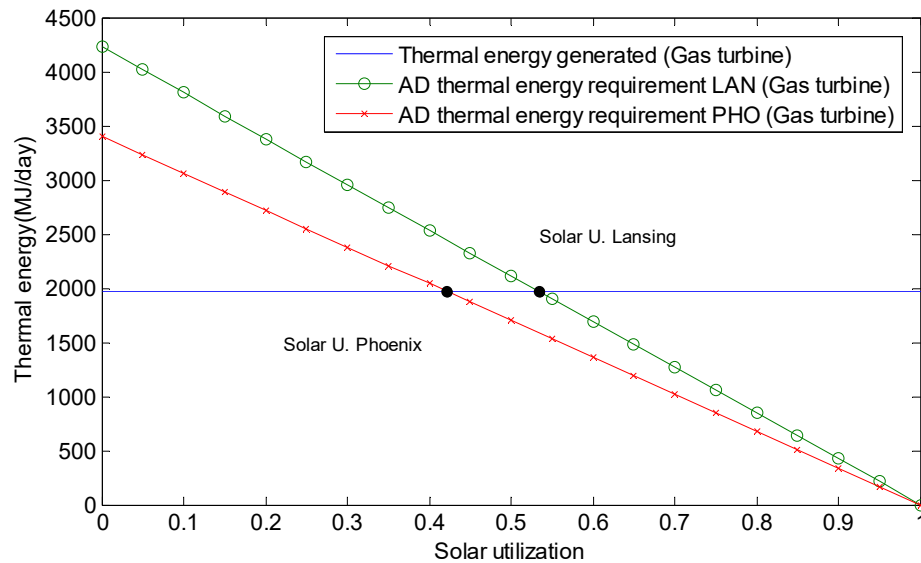
(b)

Figure 28. Relationship between the solar utilization and thermal energy requirements of the AD for the solar–bio hybridization systems*: a) steam turbine system; (b) gas turbine system.
*: A net capacity factor of 0.5 was used to calculate these numbers.

Table 18. Bioreactor volume and daily biomethane production for selected solar utilization*

Location	Reactor volume (m³)		Biomethane production (m³/day)	
	Steam	Gas	Steam	Gas
Lansing	442.08	149.43	166.34	56.23
Phoenix	549.62	185.78	206.81	69.90

*: The net capacity factor of 0.5 was used to calculate these numbers.

4.1.3.2.2 Electricity requirements for biomethane production and upgrading

Besides the thermal energy demand, biomethane production and upgrading also require electricity to power the liquid handling equipment and biomethane upgrading process. It has been reported that the electricity consumption by the liquid handling equipment (pumps, agitators, and screw compressor) is 0.0509 MJ per m³ digester per hour [71].

Biomethane also has many other compounds, such as carbon dioxide, moisture, hydrogen sulfide (H_2S), siloxanes, hydrocarbons, ammonia, and carbon monoxide. Among these compounds, H_2S and water vapor are the most corrosive compounds. The H_2S can be converted into SO_2 and SO_3 during the biomethane combustion, and consequently damage turbines and other necessary equipment. The water vapor in biomethane reacts with H_2S, NH_3, and CO_2 to form corrosive acids [72]. Thus, they must be removed before the biomethane is sent to the boiler or combustion chamber for heat and electricity generation. The typical biomethane upgrading process includes three steps consisting of water scrubbing and regeneration, cryogenic separation, and physical absorption. The electricity demands for the individual cleaning steps are listed in Table 19 [57]. Depending on the engine units, they can be configured differently. The Brayton cycle (gas turbine) requires fuel gas and air to be mixed in the burner and directly expanded in the turbine, so that it requires all three steps to clean up the biomethane and protect the turbine. The Rankine cycle (steam turbine) does not require direct contact between the biomethane and turbine, so a single step treatment of water scrubbing and regeneration is a suitable clean-up method for steam turbine application.

Table 19. Energy consumption for biomethane cleaning

Cleaning technology	Electricity consumption (kWh/normalized m³ biomethane)
Water scrubbing and regeneration	0.275
Cryogenic separation	0.24
Physical absorption	0.25

To calculate the electricity consumption required to treat the amount of biomethane from the studied thermophilic digester (Table 18), the following conversion equation was used to determine the effect of temperature on normalized biomethane volume from Table 19.

$$V_N = \frac{P_{AD} \cdot V_{AD}}{T_{AD}} \cdot \frac{T_N}{P_N} \qquad (38)$$

where $P_N = 1\ atm$; $T_N = 288.15\ K$; $P_{AD} = 1.025\ atm$; and $T_{AD} = 323.15\ K$. The calculation data show that the electricity demands for biomethane cleaning for the solar–bio hybrid gas and steam turbine systems were 2.517 MJ/m^3 and 0.9048 MJ/m^3 biogas (containing 58.6% biomethane), respectively.

4.1.3.3 Selection of solar thermal collectors for the hybrid systems

The selection of solar thermal collectors for the solar–bio hybrid systems was based on the desired temperature of the heating fluid for the steam and gas turbines. The central tower, parabolic dish, and parabolic trough are the three most popular solar thermal collection technologies [73-75]. Central tower solar collection can generate extremely high temperatures (above 1,000 °C), but requires a large footprint to accommodate the solar reflectors, which is not suitable for small-scale solar power generation. Parabolic dish solar thermal collection also generates high temperatures (500–900 °C). However, parabolic troughs generate medium temperatures (200–400 °C), so are more suitable for small-scale solar power generation [73]. For the small-scale solar–bio hybrid power generation systems, considering the required temperature of the heating fluid for steam (200 °C) and gas turbines (840 °C), parabolic trough collectors were selected to be integrated with the steam turbines and parabolic dish collectors with the gas turbines.

It has been reported that the optical efficiencies for parabolic trough and parabolic dish are approximately 0.76 and 0.93, respectively [73, 76]. The solar concentration ratio (C_r) is another important parameter for solar thermal collectors, and is expressed as the absorber area (A_a) vs. the collector area (A_c). The numbers of 70 and 750 are used as the concentration ratios for parabolic trough and parabolic dish collectors [73, 77].

Based on the collector type, working fluid temperature, and solar concentration ratio, the solar energy can be calculated by the following equation:

$$Q_S = \eta_o \cdot A_c \cdot G \cdot S_F - [\alpha \cdot \sigma \cdot A_a \cdot (T_{HS}^4 - T_\infty^4) - h \cdot A_a \cdot (T_{HS} - T_\infty)] \cdot \left(\frac{t_c}{1x10^6}\right) \qquad (39)$$

where Q_S is the solar heat required (MJ/day); η_o is the optical efficiency; A_c is the collector area (m^2); G is the direct normal irradiance (MJ/m^2·day); S_F is the solar operating factor (which, for parabolic trough and parabolic dish collectors, is 0.878 and 0.429, respectively, at Lansing and 0.934 and 0.4752, respectively, at Phoenix); α is the absorber emittance (0.27, stainless steel Type 312 [55]); σ is the Stefan-Boltzmann constant (5.67 × 10^{-8} W/m^2·K^4); A_a is the absorber area (m^2); T_∞ is the ambient temperature (K); h is the convective coefficient (8 W/m^2·K); t_c is the solar energy collection time (which, for the parabolic dish and parabolic trough collectors is 5.65 and 5.88 h per day, respectively, at Lansing; and 9.66 and 9.69 h per day, respectively, at Phoenix); and T_{HS} is the receiver's absorber temperature (K), which is assumed to be 25% higher than the maximum temperature of the working fluid (water or air) in the system. The solar operating factor (S_F) is defined as the ratio of direct normal irradiance that can be used by the solar collection technology for electricity generation, and is calculated as the ratio of the total thermal power produced and the absorbed thermal energy. The S_F values were obtained using the software System Advisor Model [78].

In addition, the working fluids (water and air) have a large impact on the thermal efficiency of the heat exchanger (ε_{HE}). The overall heat transfer coefficient (the capability of the heat exchanger to transfer thermal energy) is several orders of magnitude higher for water than for air [69, 79], and the thermal efficiency of air is correspondingly lower than that of water. The

ε_{HE} values for air and water were selected as 0.70 and 0.85, respectively, in this study. Therefore, the heat that the working fluid transfers from the absorber to the boiler and burner can be calculated as

$$Q_{FL} = \frac{Q_S}{\varepsilon_{HE}} \qquad (40)$$

where Q_{FL} is the energy transferred (MJ/day) from the absorber to the working fluid; and ε_{HE} is the thermal efficiency of the heat exchanger.

Under the conditions of the coldest winter day and a net capacity factor of 0.5, the solar collector area required by the solar–bio hybrid systems to generate 30 kW electricity can be calculated (Table 20). Because Phoenix has a much higher ambient temperature and DNI than Lansing year-round, the required solar collector areas at Phoenix for steam and gas turbines were 180.4 m^2 and 330.1 m^2, respectively, much smaller than those in Lansing, which for steam and gas turbines were 1,034.8 m^2 and 1,502.1 m^2, respectively.

Table 20. Required solar collector areas for steam and gas turbines at Lansing and Phoenix on the coldest winter day for a net capacity factor of 0.5

Location	Solar collector area (m^2)	
	Steam	Gas
Lansing	1,034.8	1,502.1
Phoenix	180.4	330.1

Based on the selected solar collector area at the coldest time, the monthly net capacity factors were simulated for both systems at Phoenix and Lansing (Figure 29). Since the coldest time of the year is used as a reference state to select the solar collector area, the solar thermal energy generated during most of the year exceeds the value for the minimum heat requirements. The biomethane is therefore used to extend the operating hours of the power generation system, and the net capacity factor is correspondingly increased. In the warm climate location (Phoenix), during the month of July, which has the highest ambient temperature, the net capacity factors for the steam and gas turbine systems were increased by 13.82% and 24.50%, respectively (Figure 29b). In the cold climate location (Lansing), the net capacity factors changed more dramatically. During July, the net capacity factors for the steam and gas turbine systems were increased by 70.88% and 95.82%, respectively (Figure 29a).
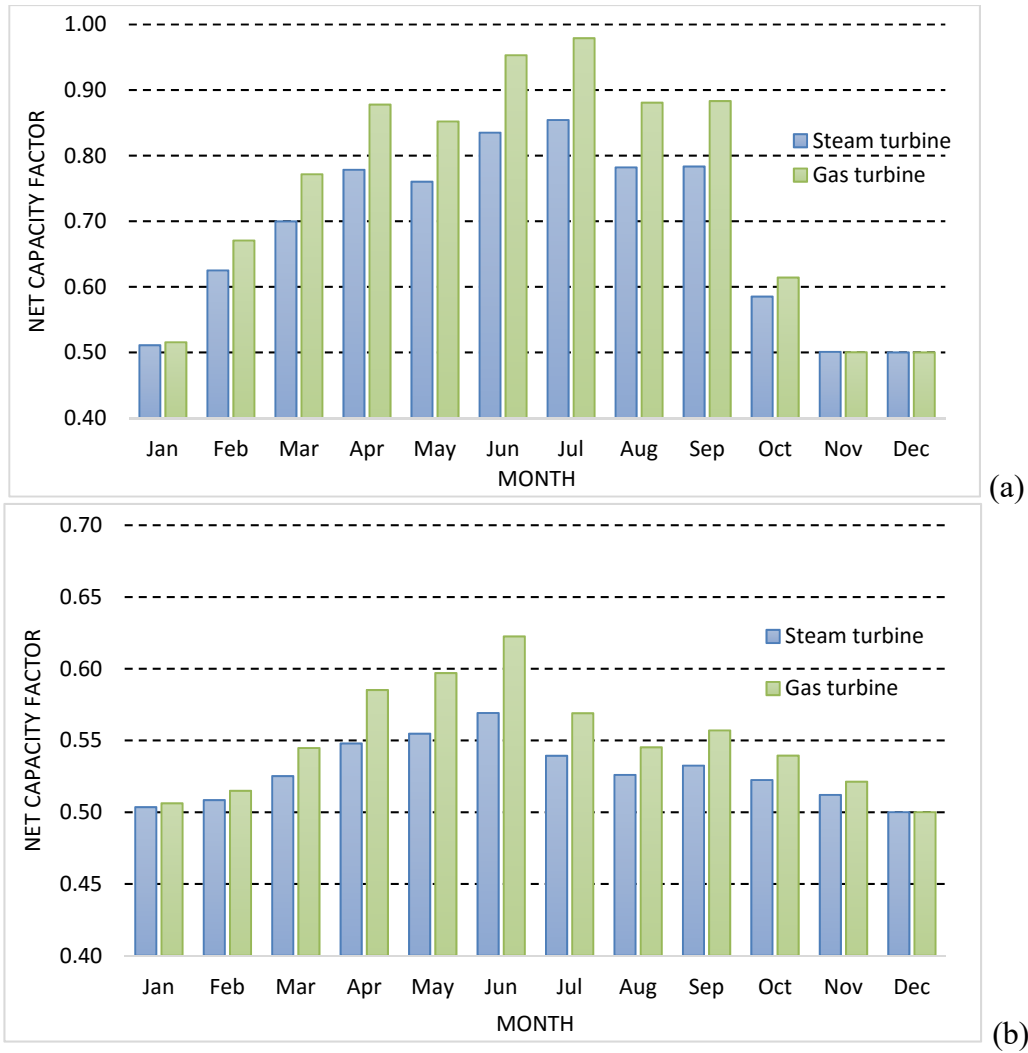
Figure 29. Effects of location and month on the net capacity factor of the solar–bio hybrid power generation system: (a) Lansing; (b) Phoenix.

4.1.3.3 System analysis

The system analysis shows the relationship between the net capacity factor, bioreactor volume, solar thermal utilization, and geographic location for both the Brayton and Rankine cycles. According to the system configurations (Figure 10), the highest temperatures required for individual thermal cycles determine the solar collector technologies that can be integrated into the solar–bio hybrid power generation systems. In the case of the steam turbine (Rankine cycle), the maximum temperature (turbine inlet) is 200 °C (Figure 10b), which can be achieved by medium-temperature solar thermal technologies, such as the parabolic trough proposed by this study. However, the working fluid in the gas turbine (Brayton cycle) needs to be heated by solar thermal energy from 533 °C at the outlet of the regenerator to 840 °C before entering the burner (Figure 10d). High-temperature solar thermal technologies, such as the parabolic dish selected by this study, are required to satisfy the need of such a high temperature increase. However, 840 °C is at the higher end of the temperature range that conventional parabolic dishes (with a reflector area ranging from 43 m^2 to 117 m^2) can achieve [80, 81]. This is a limiting factor for the further increase of solar thermal energy utilization in the gas turbine hybrid system. Although it is

63

theoretically possible to raise the temperature at the absorber of a parabolic dish to above 1,000 °C by extending the reflection area, fabricating such large parabolic dishes may pose certain manufacturing and installation difficulties, as well as economic barriers for small-scale applications.

Since the solar radiation and ambient temperature vary significantly between seasons and locations (Figure 11), the bioreactor volume must be large enough to produce sufficient methane to satisfy the system energy demands when the solar thermal energy is not able to fulfill the heating requirements (i.e., in the winter months at Lansing). This is the reason that the minimum solar utilization values for the system design were selected by this study based on maintaining the capacity factor of 0.5 on the coldest day of a year. Moreover, due to the thermodynamic difference in fuel efficiency between the gas and steam turbines, the required bioreactor volumes are different for the hybrid systems. The fuel efficiency for the gas turbine (27.32%) is much higher than that for the steam turbine (14.69%). The corresponding bioreactor of the steam turbine hybrid system is approximately 2.95 times larger than that of the gas turbine hybrid system (Table 18).
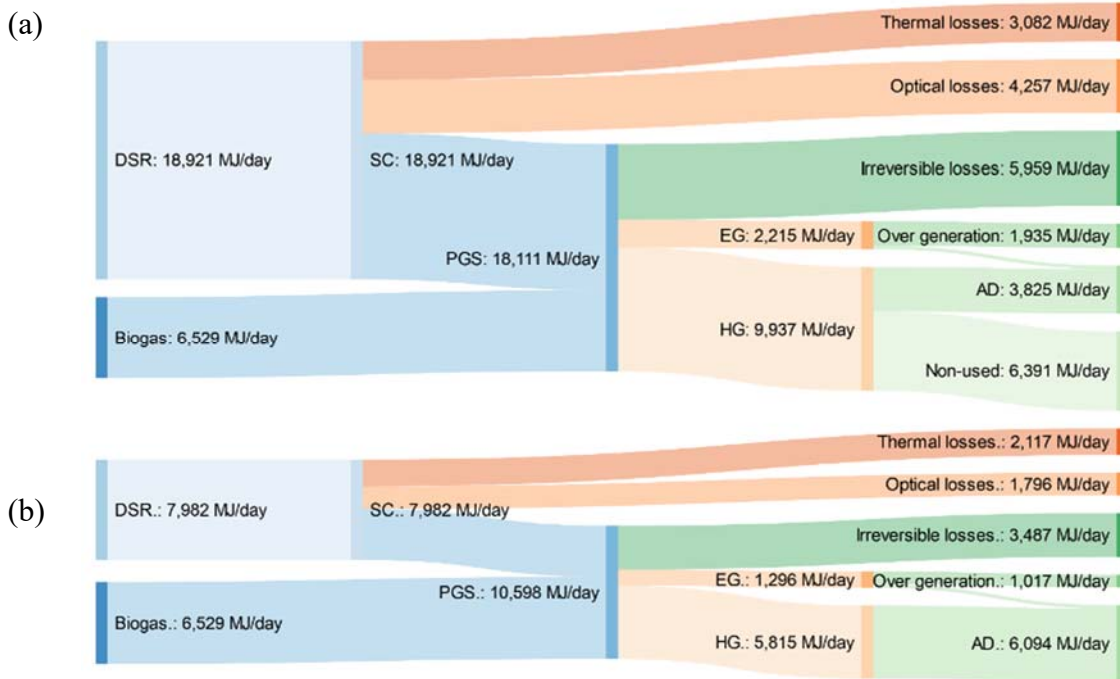
In addition, as mentioned previously, the ambient temperature and solar radiation have a strong influence on the configuration of hybrid systems. The simulation results demonstrated that the solar–bio hybrid steam turbine system required a smaller solar collector area (1,034.8 m^2 and 180.4 m^2 for Lansing and Phoenix, respectively) than the gas turbine system (1,502.1 m^2 and 330.1 m^2 for Lansing and Phoenix, respectively) (Table 20). This is mainly caused by the low value of the solar operating factor for the gas turbine systems. The solar collector area must be over-sized to satisfy the energy demand of the working fluid when the direct normal irradiance is weak during the winter months. Considering the fact that a smaller footprint is desirable for small-scale systems, the solar–bio hybrid steam turbine power generation with a smaller solar collector area is thus preferred

The overall energy balance for the coldest and hottest months at the two locations elucidates the comprehensive energy distribution profiles for both systems (Figure 30). Because of the low thermal efficiency of the steam turbine, the solar–bio hybrid steam turbine system (245.33 kW) demanded 2.23 times more heat than the hybrid gas turbine system (109.83 kW) to generate 30 kW electricity (Tables 4 and 5). The steam turbine hybrid system had a higher ratio of heat generation to total energy input (0.5487) than the gas turbine hybrid system (0.4143); and the corresponding heat generated for the steam and gas turbine hybrid systems was 134.61 kW and 45.50 kW, respectively. During the coldest winter month, the heat was completely used to maintain the culture temperature of the anaerobic digestion for biomethane production and ensure the generation of the target electricity amount.
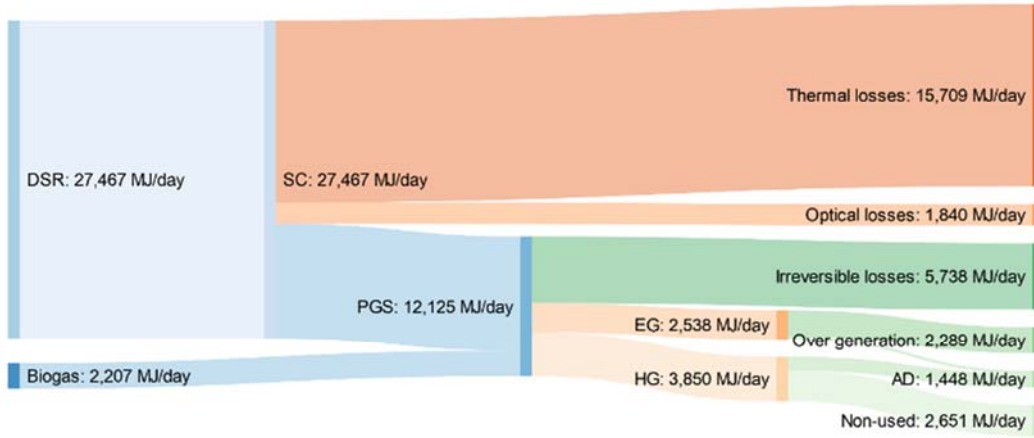
During the hottest summer month, extra heat was generated from both systems in both locations (Figure 30 a, c, e, and f). In addition, although the fuel efficiency of the gas turbine is higher than that of the steam turbine, the global efficiencies (electricity and heat outputs vs. biomethane and solar energy inputs) of the solar–bio hybrid steam turbine system (47.75% in July and 49.00% in December at Lansing, 58.13% in July and 58.92% in December at Phoenix) were significantly higher than those of the solar–bio hybrid gas turbine system (21.52% in July and 23.64% in December at Lansing, 30.84% in July and 32.69% in December at Phoenix). Moreover, due to the temperature differences between winter and summer for both locations, the larger temperature difference requires larger solar collectors and correspondingly more heat. The hybrid steam and gas turbine systems located at Lansing generate 38.9% and 45.9% more heat, respectively, than those located at Phoenix. As for electricity generation, the solar–bio hybrid

64

steam turbine system requires more biomethane to maintain the net electricity output of 30 kW. The parasitic electricity energy required by the hybrid steam turbine system (279 MJ/day and 347 MJ/day for Lansing and Phoenix, respectively) was higher than that required by the hybrid gas turbine systems (249 MJ/day and 310 MJ/day for Lansing and Phoenix, respectively), although the gas turbine requires more electricity to clean up the biomethane for power generation. In addition, the systems at the location with lower solar thermal utilization (i.e., Phoenix) require more biomethane energy, and correspondingly increase the consumption of parasitic electricity, which leads to a lower net electricity output (Figure 30).
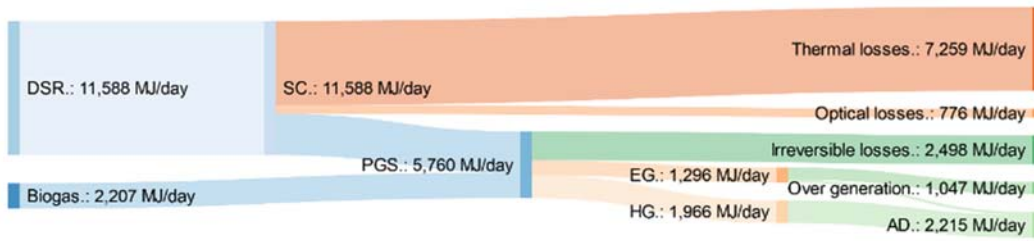
The analysis in this study is based upon the use of solar thermal energy as a supplemental energy source to facilitate the utilization of the biofuel–biomethane, and indirectly improve the power generation performance of the system. As a matter of the fact, the net capacity factor can be significantly increased if the solar thermal energy can be utilized directly as a single energy source in the thermodynamic cycle for several hours per day (once solar radiation is able to bring the working fluid to the desired temperatures for the gas and steam turbines). Further studies are needed to explore such scenarios.
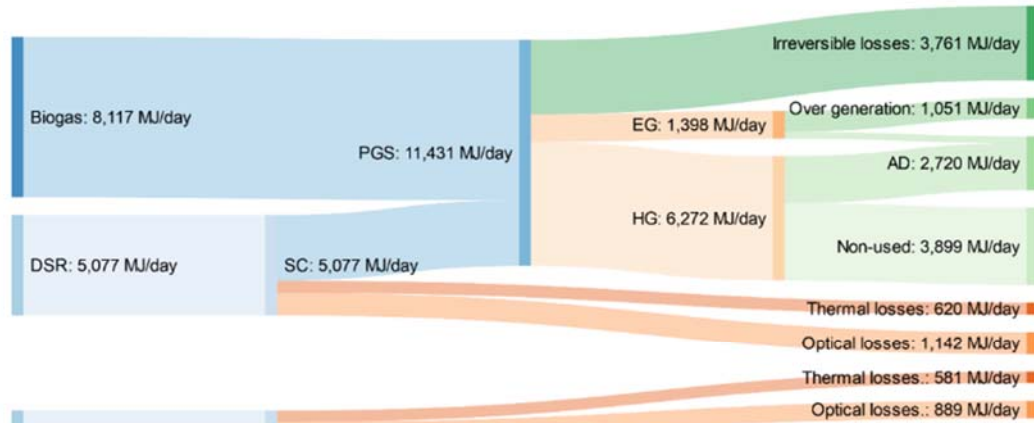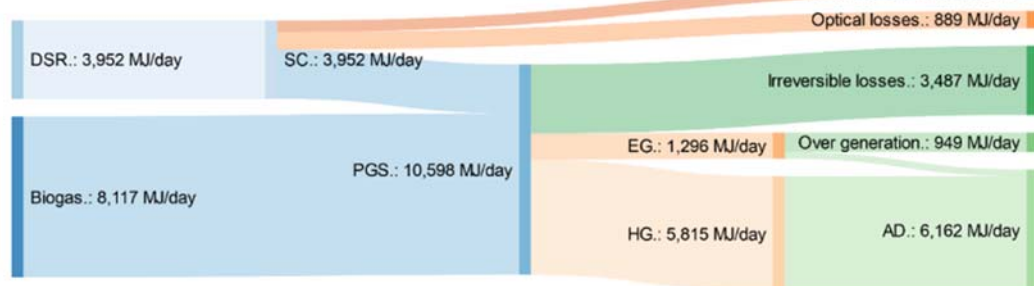
(c)

DSR: 27,467 MJ/day | SC: 27,467 MJ/day | Thermal losses: 15,709 MJ/day
Optical losses: 1,840 MJ/day
PGS: 12,125 MJ/day | Irreversible losses: 5,738 MJ/day
EG: 2,538 MJ/day | Over generation: 2,289 MJ/day
Biogas: 2,207 MJ/day | HG: 3,850 MJ/day | AD: 1,448 MJ/day
Non-used: 2,651 MJ/day

(d)

DSR.: 11,588 MJ/day | SC.: 11,588 MJ/day | Thermal losses.: 7,259 MJ/day
Optical losses.: 776 MJ/day
PGS.: 5,760 MJ/day | Irreversible losses.: 2,498 MJ/day
EG.: 1,296 MJ/day | Over generation.: 1,047 MJ/day
Biogas.: 2,207 MJ/day | HG.: 1,966 MJ/day | AD.: 2,215 MJ/day

(e)

Biogas: 8,117 MJ/day | Irreversible losses: 3,761 MJ/day
Over generation: 1,051 MJ/day
PGS: 11,431 MJ/day | EG: 1,398 MJ/day | AD: 2,720 MJ/day
HG: 6,272 MJ/day | Non-used: 3,899 MJ/day
DSR: 5,077 MJ/day | SC: 5,077 MJ/day | Thermal losses: 620 MJ/day
Optical losses: 1,142 MJ/day

Thermal losses.: 581 MJ/day
Optical losses.: 889 MJ/day

(f)

DSR.: 3,952 MJ/day | SC.: 3,952 MJ/day | Irreversible losses.: 3,487 MJ/day
EG.: 1,296 MJ/day | Over generation.: 949 MJ/day
Biogas.: 8,117 MJ/day | PGS.: 10,598 MJ/day | HG.: 5,815 MJ/day | AD.: 6,162 MJ/day
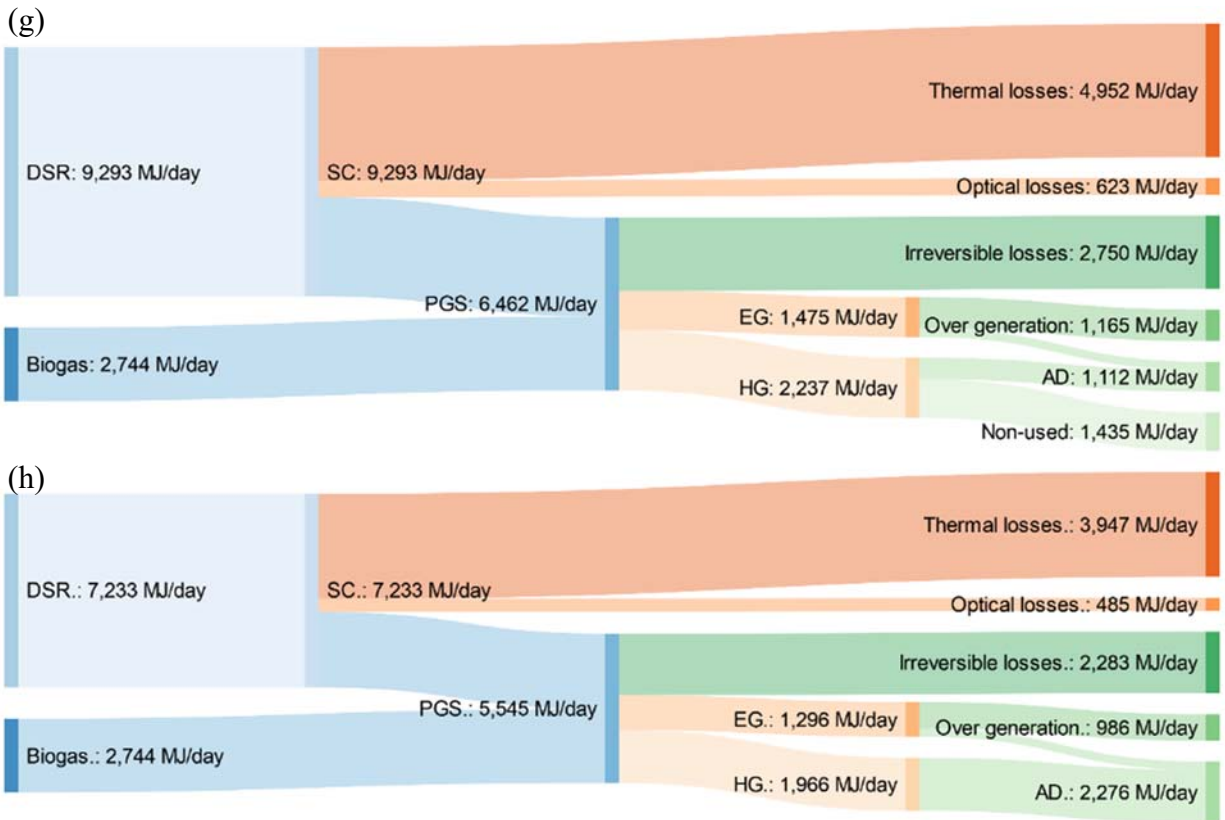
66

(g)

(h)

Figure 30. Energy balance of small-scale solar–bio hybrid power generation systems*
*: (a) Steam power generation system in Lansing in July; (b) steam power generation system in Lansing in December; (c) gas power generation system in Lansing in July; (d) gas power generation system in Lansing in December; (e) steam power generation system in Phoenix in July; (f) steam power generation system in Phoenix in December; (g) gas power generation system in Phoenix in July; (h) gas power generation system in Phoenix in December.
DSR: available direct solar radiation; Biomethane: energy obtained from biomethane combustion; SC: solar collector subsystem; PGS: power generation subsystem; Thermal losses: losses in the solar collector due to radiation, convection, and solar operating factor influence; Optical losses: losses in the solar collector due to absorptivity of the reflector and reflectivity of the absorber; Irreversible losses: energy losses in the heat transfer equipment; EG: electricity generation in the PGS; NEG: net electricity generation; HG: heat generation in the PGS; AD: electricity required in the anaerobic digestion subsystem; and Extra heat: heat generated in the power generation system not used by the anaerobic digestion process.

A comprehensive analysis on small-scale solar–bio hybrid power generation (30 kW) has been carried out. The relationship between net capacity factor, solar utilization efficiency, and biomethane utilization efficiency has been determined. The analysis demonstrated that the hybrid steam turbine system had better global thermal efficiency (54.87%) than the hybrid gas turbine system (41.43%), although the electricity generation efficiency of the hybrid steam turbine system (14.69%) was lower than that of the hybrid gas turbine system (27.32%). Moreover, the global efficiencies of the solar–bio hybrid steam turbine system were significantly higher than those of the solar–bio hybrid gas turbine system, regardless of location. It was found from the

67

analysis that, in order to reduce the system footprint, the hybrid steam turbine is preferable to the hybrid gas turbine system.

4.2 Optimizing lab-scale upflow fixed-film anaerobic digestion on blackwater and food wastes

4.2.1 Effects of the Pall-ring median on the upflow fixed-film anaerobic digestion

A preliminary experiment prior to CRD was conducted to investigate the effects of the Pall-rings on the anaerobic digestion. The fixed film digesters contained 25 rings (1 inch OD, 1 inch height). A feedstock concentration of 1% was tested under a HRT of 6 days and temperature of 35°C. The control was under the same conditions except Pall rings in the reactor. The overall biogas accumulation is demonstrated in Figure 31. The digester with Pall-rings had significantly higher biogas production than the control. In addition, the Pall rings helped to suppress the accumulation of organic foam in the digester and make the maintenance easier and ensure a long term operation. Therefore, the upflow fixed film reactor was selected for the rest of the study.
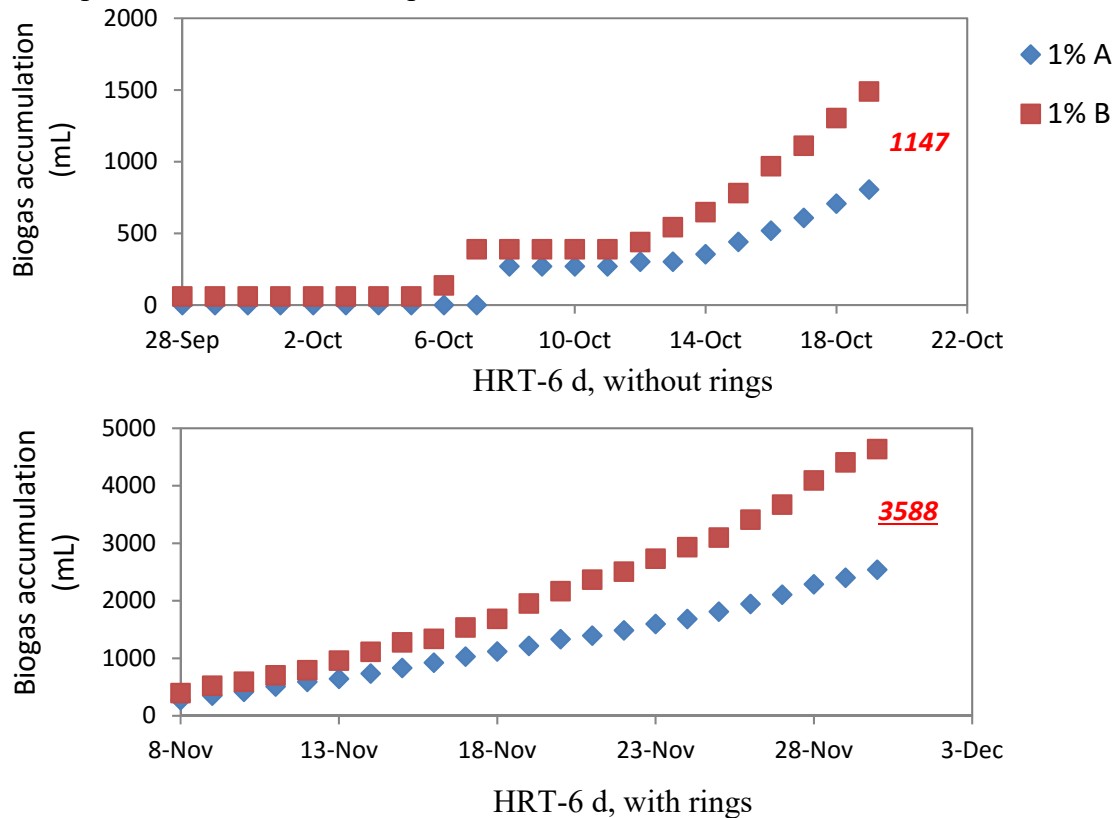

Figure 31. Overall biogas accumulation in digesters with and without plastic ring shaped media at 35 °C and HRT-6 d*
*: Each condition had two biological replications.

4.2.2 Effects of HRT, temperature, and TS on performance of upflow fixed film anaerobic digestion

The CRD experiment demonstrates that biogas accumulation increased with the increase of TS and temperature. As shown in Figure 32, under the mesophilic condition (35 °C), 1% TS had a highest biogas accumulation of 3.0 L, it was 8.2 L for 3% TS and 11.9 L for 5% TS. The effect of HRT on the biogas accumulation had different trends. Under the thermophilic condition (50 °C), the 3% TS accumulated double the amount of biogas than 35 °C. 1% and 5% also had significant increase at higher reaction temperature. However, 5% did not produced more biogas

69

than the 3% as it did at 35 °C. Therefore the optimal conditions of digesting food waste based on *biogas accumulation* were 3% TS at 50 °C with HRTs of 6 and 4 days.

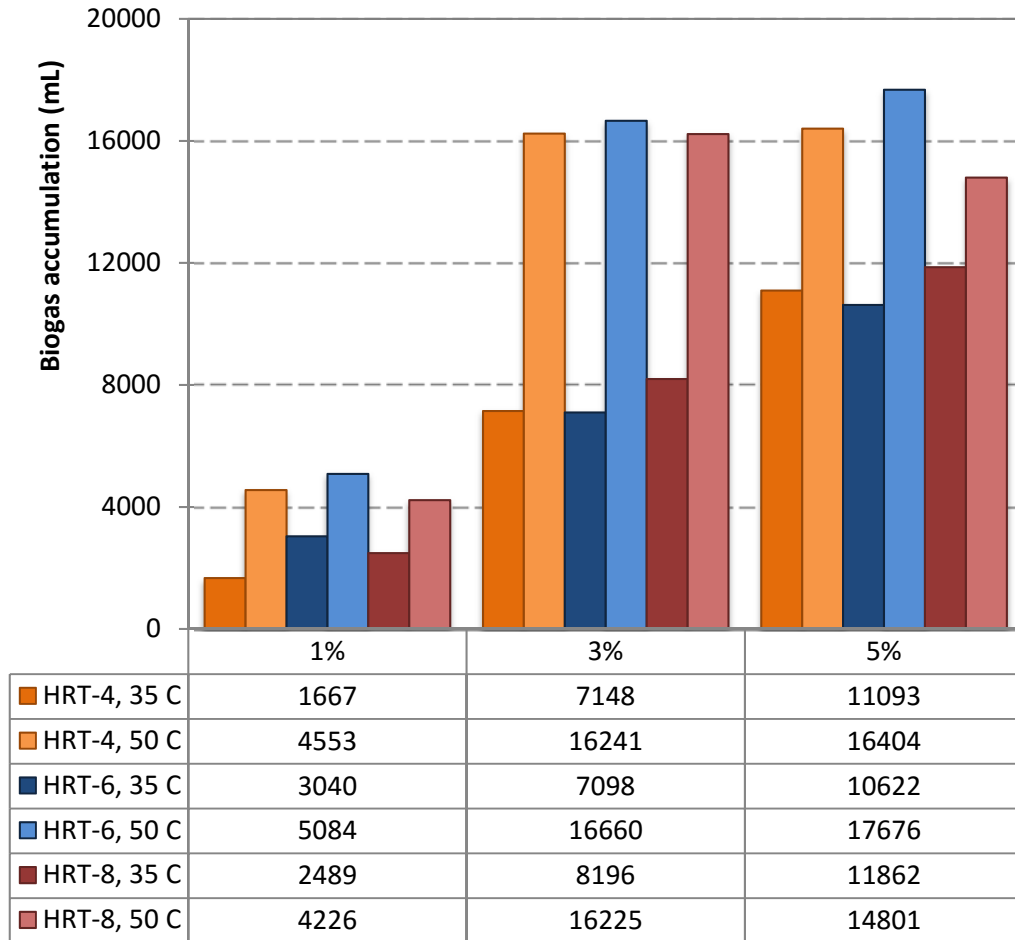|	1%	3%	5%
■ HRT-4, 35 C	1667	7148	11093
■ HRT-4, 50 C	4553	16241	16404
■ HRT-6, 35 C	3040	7098	10622
■ HRT-6, 50 C	5084	16660	17676
■ HRT-8, 35 C	2489	8196	11862
■ HRT-8, 50 C	4226	16225	14801

Figure 32. The biogas accumulation from all treatments

Figure 33 represents the TS reduction under different digestion conditions. Both 1% and 3% had similar TS reduction at mesophilic condition. Their TS reduction increased by 26-51% once the digestion was under thermophilic condition. It is noticeable that both 1% and 3% had significant lower TS reduction under HRT 8 days and 50 °C than 5%. As for 5% TS, neither HRT nor temperature had significant impact on the TS reduction. Therefore, the optimal digesting conditions based on TS reduction were 3% OLR at 50 °C with HRT of 4 and 6 days.

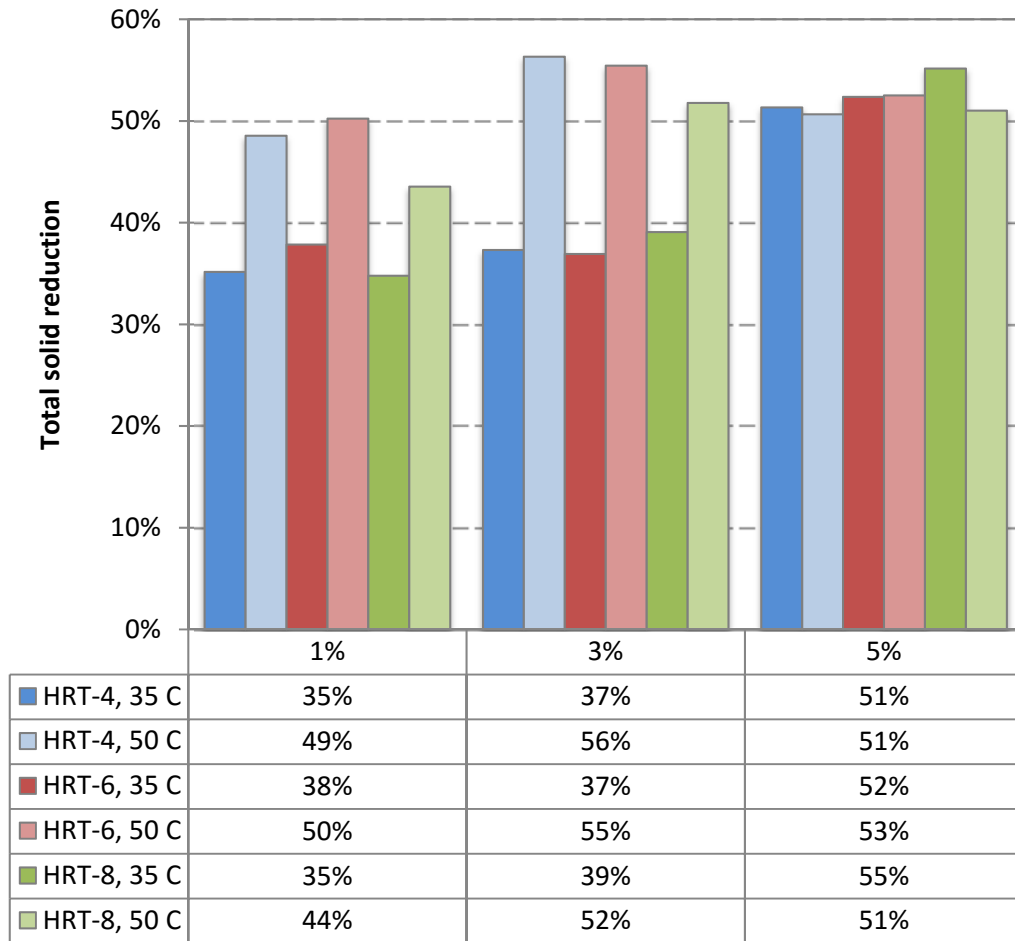|	1%	3%	5%
■ HRT-4, 35 C	35%	37%	51%
□ HRT-4, 50 C	49%	56%	51%
■ HRT-6, 35 C	38%	37%	52%
■ HRT-6, 50 C	50%	55%	53%
■ HRT-8, 35 C	35%	39%	55%
□ HRT-8, 50 C	44%	52%	51%

Figure 33. The total solids reduction from different digestion conditions

Considering both biogas accumulation and TS reduction, biogas productivity was calculated. The biogas productivity was defined as the volume of biogas produced from one gram of organic matter (TS) consumed by the microbes (Figure 34). Generally, all thermophilic digesters performed significantly better than mesophilic ones. The 5% TS had the lowest biogas productivity at both temperatures and all three HRTs. The 1% TS at 35 °C had better biogas productivity compared to corresponding 3% TS regardless HRT change. Both 1% and 3% TS at 50 °C had similar productivities. Therefore, the optimal digesting conditions based on the biogas productivity were both 1% and 3% OLR at 50 °C with HRT of 6 and 8 days.

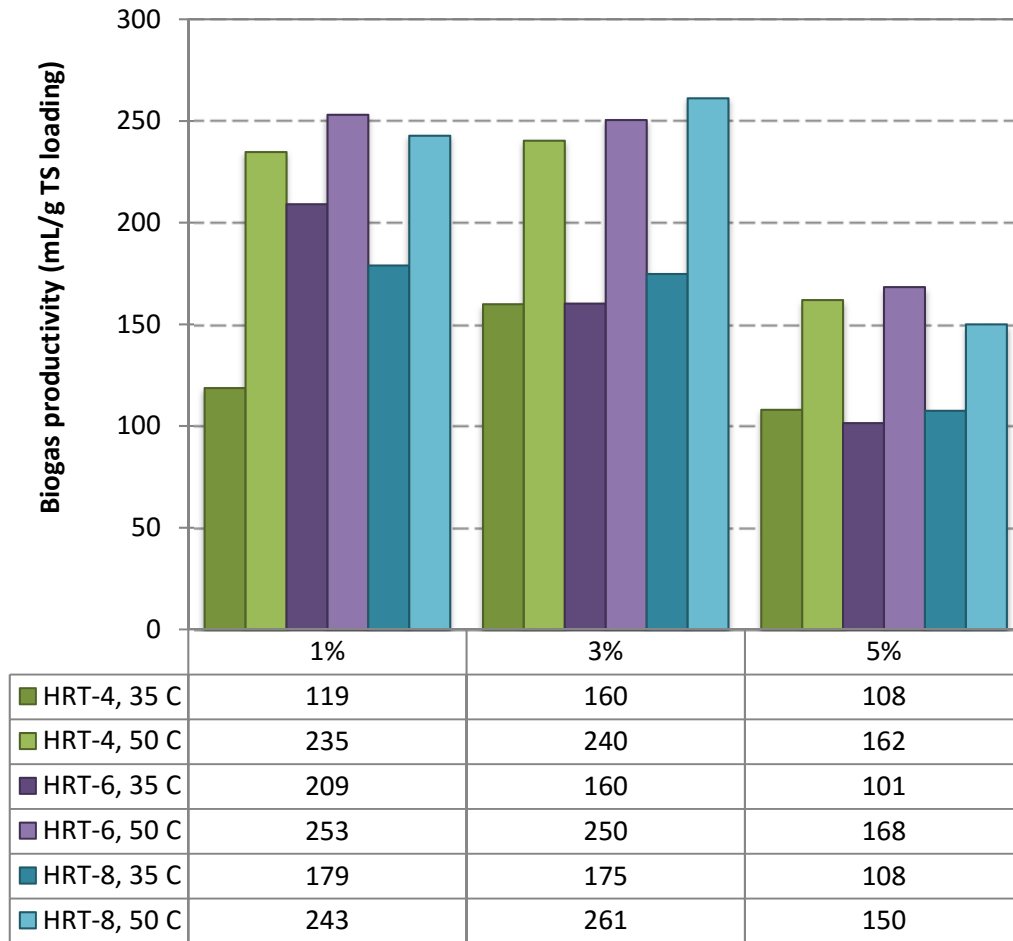|	1%	3%	5%
■ HRT-4, 35 C	119	160	108
■ HRT-4, 50 C	235	240	162
■ HRT-6, 35 C	209	160	101
■ HRT-6, 50 C	253	250	168
■ HRT-8, 35 C	179	175	108
■ HRT-8, 50 C	243	261	150

Figure 34. The biogas productivity from all treatments

According to the CRD, the results demonstrate that 3% OLR at 50 °C with HRT 6 days was the best operating condition based on biogas accumulation, TS reduction and biogas productivity. The digesters of 3% TS in general had superior and stable performance than the other two TS contents. The 1% TS had the greatest variation between replications, which was possibly caused by that the organic matter in these digesters was not sufficient to provide carbon and other nutrients for microbial communities. The 5% OLR at 50 °C did not show the further increase of biogas production. It might be due to that feedstock loading exceeded the digestion capacity in the tested range of HRTs. If future project is aimed to improve the performance at 5% TS, extended HRTs for the upflow fixed film reactor needed to be studied.

Furthermore, the significance of three factors (organic loading rate, hydraulic retention time and temperature) were statistically examined (Figure 35) based on biogas productivity. Figure 46a demonstrates that 5% TS was significantly lower than the other two TS loadings, but 1% and 3% were not significantly different from each other. The analysis also demonstrates that there was no significant difference between all three HRT levels. As for the reaction temperature, thermophilic condition was significantly more effective than mesophilic.
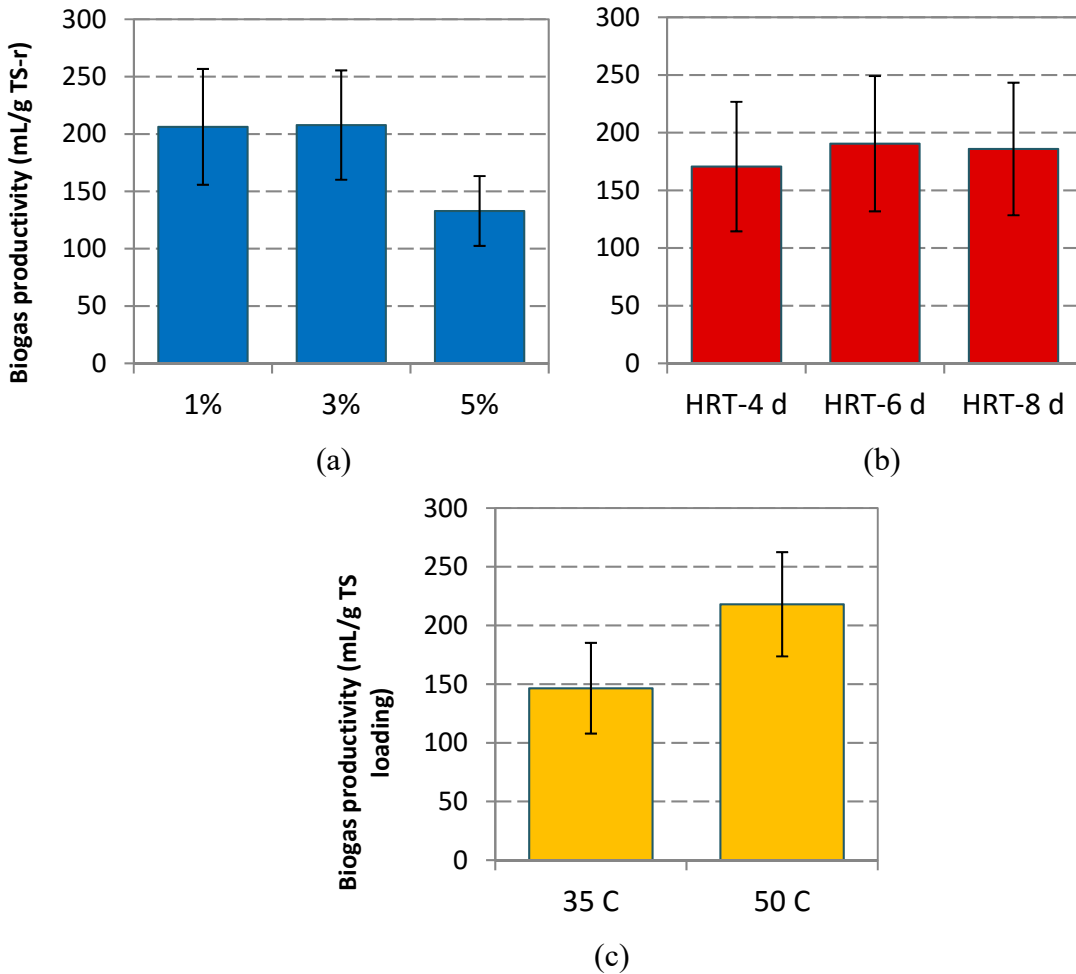
Figure 35. Statistical analysis on significance of all three factors
(a) Biogas productivity in response to TS loading, (b) Biogas productivity in response to HRT,
(c) Biogas productivity in response to the temperature

Methane production from 18 treatments were presented in Table 21. The data demonstrated that several treatments (3% food waste in HRT-4, 6 and 8 days at 50 °C, 1% in HRT-6 and 8 days at 50 °C) had over 160 g methane produced for every kg food waste (TS) destroyed. Considering the TS loading and gas production, 3% TS and HRTs of 6 and 8 are the preferred conditions for the digestion.

Table 21. Mass balance for upflow fixed film anaerobic digestion

TS	1%	3%	5%
Methane production [g CH4/kg TS of food waste] [a]			
HRT-4, 35 C	79	106	72
HRT-4, 50 C	156	**160**	108
HRT-6, 35 C	139	107	68
HRT-6, 50 C	**169**	**167**	112
HRT-8, 35 C	119	116	72

HRT-8, 50 C	**162**	**174**	100

a. Methane production [g CH$_4$/kg TS of food waste] = Overall biogas [L] * biogas density [g/L] * methane content in biogas [%] / (total solids loaded [g] * solid reduction rate [%]), where the biogas density was 1.11 g/L, and methane content in biogas on average was 60%.

4.3 Studying electrocoagulation to reclaim water
4.3.1 Studying the effects of electrocoagulation on the AD effluent treatment
### 4.3.1.1 The 1st EC treatment

TS and COD removal effects were demonstrated in Figure 36. According to the GLM analysis, the experimental runs with the current of 2A had a significantly ($p<0.05$) better COD removal (62.9%) than other current levels. The higher currents of 1A and 2A also had better TS removal than the lower current of 0.5 A. Under the current of 2A, longer RT and smaller SA were beneficial for both COD and TS removal. The results indicate that current density (current strength on unit surface area of electrodes) was critical to improve the electrocoagulation performance on AD liquid effluent, which is consistent with other studies on various waste streams [82, 83]. It was reported that high current density leads to generation of a large amount of cations and gas bubbles, cations act as coagulants to agglomerate small particles to form flocs in the solution, the gas bubbles then float the flocs to the surface, and the water is reclaimed [84, 85]. With more particles being removed by flocculation and flotation, the electrical conductivity of the EC solution was correspondingly decreased. Thus, the electrical conductivity could serve as an indirect indicator of EC performance of particle removal. As shown in Figures 36, a big drop of electrical conductivity was observed with the runs under 2A that had better TS and COD removal than other current levels.

Considering TS and COD removal, the EC conditions of 2A, 60 min with electrode surface area of 62 cm^2 were selected to carry on the 1st stage EC treatment of AD effluent. Dynamic change of COD, TP and TN during the selected EC treatment was further investigated (Figure 37a). TP was dropped from 340 mg/L to 0 mg/L within 60 min of HR, and a COD removal of 86% was achieved during 60 min of EC. However, TN content was barely impacted by the EC treatment, maintaining a relative high level of 1000 mg/L. It is because over 80% of total nitrogen in the liquid AD effluent was in the form of ammonia. Ammonia is highly soluble in water and thus difficult to be removed by EC. Both pH and power consumption kept increasing during the 1st EC (Figure 37b). At the end of the 1st EC, the pH and power consumption reached 11.5 and 0.12 kWh/L respectively.
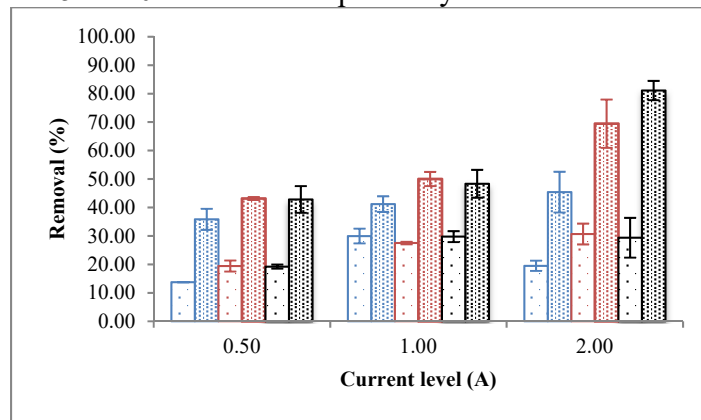

(a)
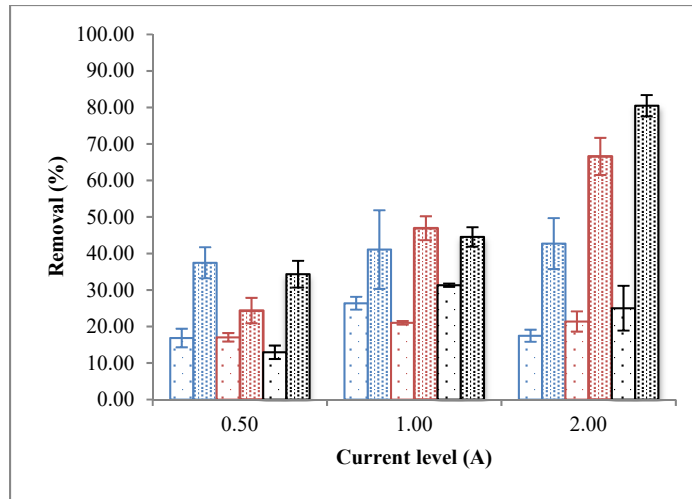
(b)
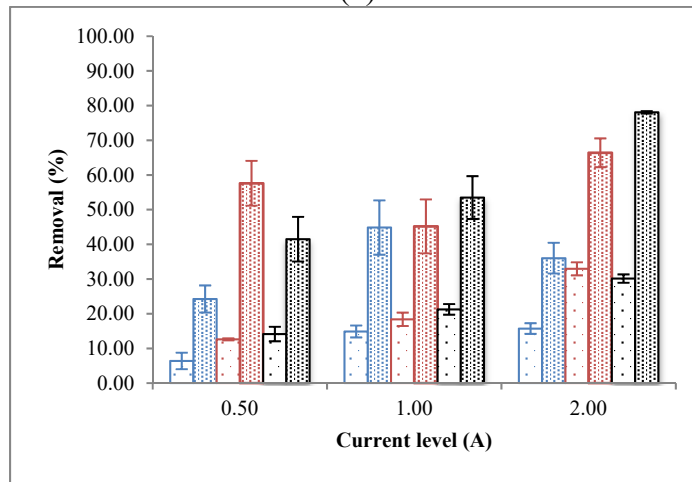
(c)

Figure 36. TS and COD removal of 1st stage EC *

*Columns with sparse dots stand for TS removal, and columns with dense dots stand for COD removal. Blue (left), red (middle) and black (right) stand for the retention times of 20, 40 and 60 min respectively. (a) TS and COD removal efficiency with electrode surface area of 62 cm^2. (b) TS and COD removal efficiency with electrode surface area of 134 cm^2. (c) TS and COD removal efficiency with electrode surface area of 210 cm^2. * Data represent the average of three replicates with standard deviation
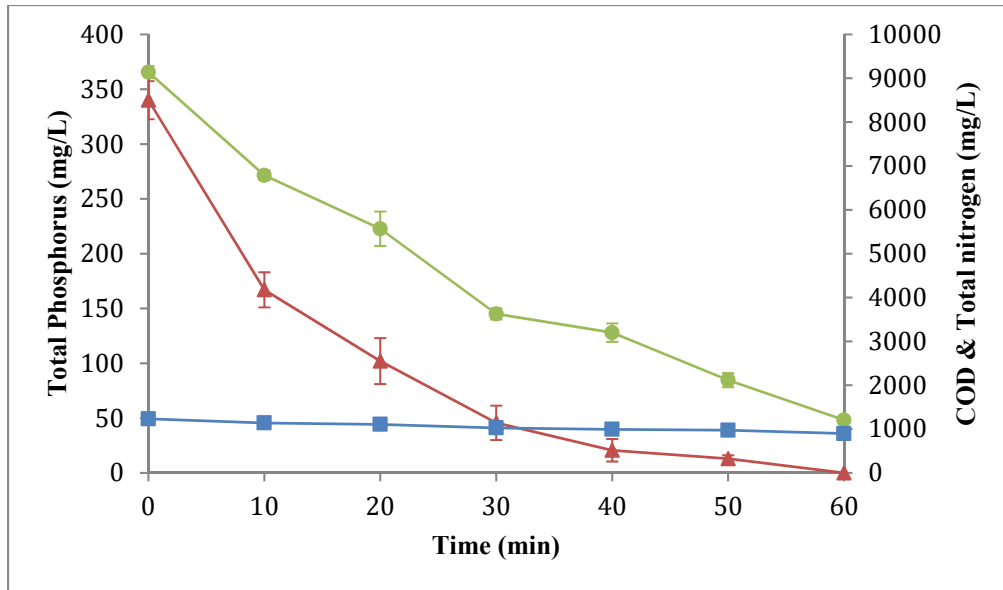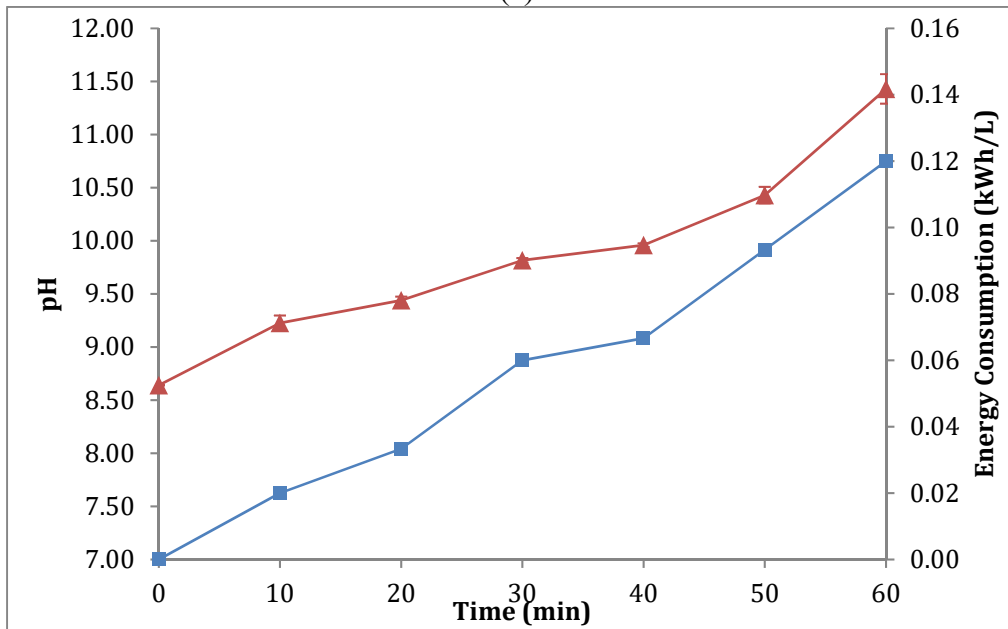
Figure 37. Dynamic change of nutrients, pH and power consumption of 1st EC under the selected conditions*

(a) Dynamic change of TP, COD and TN of AD effluent. Red triangle stands for TP, green circle stands for COD, and square blue stands for TN. (b) Dynamic change of pH and power consumption of AD effluent. Red triangle stands for pH change, and blue square stands for energy consumption.

*Data of power consumption, TP and COD are the average of three replicates

4.3.1.2 Biogas cleanup and pH adjustment of the EC effluent

Although significant improvement of TS, COD, and TP removal were obtained from the 1st EC, COD was still at a level over 1000 mg/L, which means that both organic and inorganic

pollutants were still abundant in the EC effluent [19]. In order to achieve water reclamation from AD liquid effluent, an additional EC is needed. However, as shown in Figure 37b, pH of the solution was very high at the end of the 1st EC due to the production of hydroxide ion (OH^-) during the EC. It has been reported that a high initial pH would negatively influence the EC performance [82, 86-88]. Under high pH level, removal efficiency of COD, TS and other nutrients during EC treatment is largely reduced, and energy demand is dramatically increased, which make EC process energy intensive and less efficient. It has also been reported that pH range of 4.0 – 8.0 is preferred as initial pH for EC to have a good nutrients removal performance with relatively less energy demand [89, 90]. A pH adjustment was thereby necessary in EC treatment to maintain a good efficiency. On the other hand, the byproducts of CO_2 and H_2S in biogas are acidic, and using them to neutralize the pH of EC solution can address both issues of biogas cleanup and EC performance efficiency. A biogas pumping step was thus introduced to mix raw biogas and the 1st EC effluent.
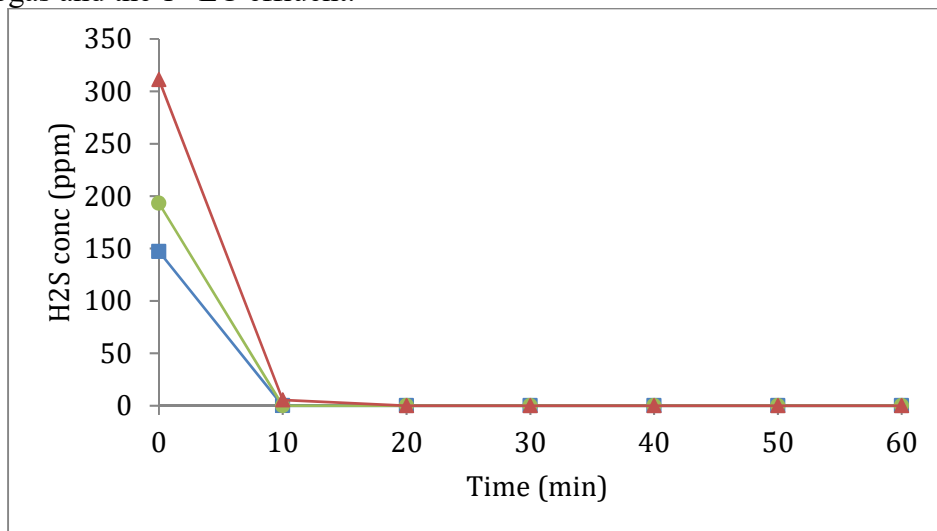

(a)
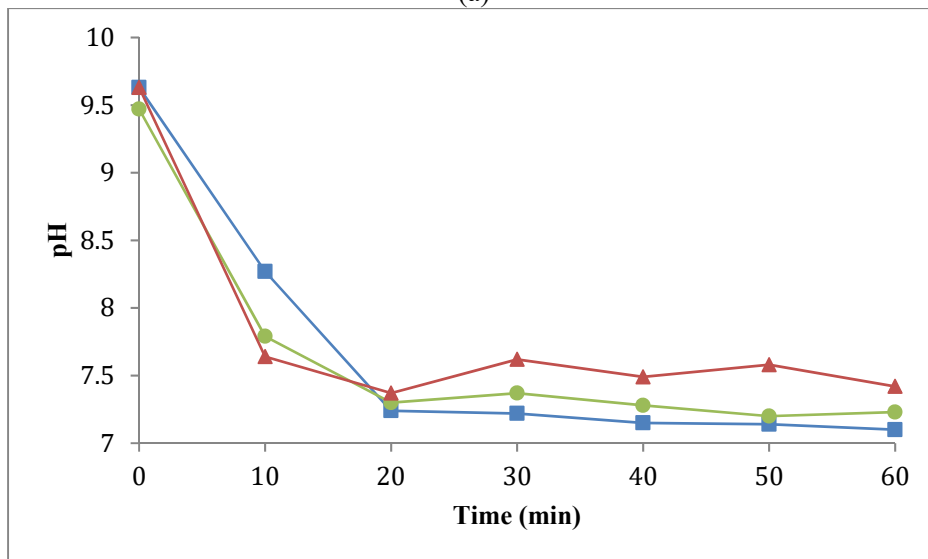
(b)

Figure 38. H2S and pH change of 1st EC effluent during biogas pumping

Blue square stands for batch 1, green circle stands for batch 2, red triangle stands for batch 3. (a) Dynamic change of H₂S concentration. (b) Dynamic change of pH

As shown in Figure 38a, H₂S concentration dramatically dropped from 300 ppm to 0 ppm in the first 20 min of biogas pumping, and maintained no detectable for the rest of the testing period (60 minutes). However, once the H₂S concentration in the biogas exceeded 300pm, there was small amount of H₂S (35 ppm) detected in the treated biogas at the end of the testing period. These results indicated that the conditions of 60 minutes and 1 vvm are good for the biogas containing 300 ppm or less H₂S, but may not be suitable for the biogas with high H₂S content. In-depth studies are needed to further understand the effects of EC solution and biogas pumping on H₂S removal. Gas analysis also demonstrated that CH₄ content stayed stable during the biogas pumping. CO₂ was declined slightly at the beginning of the biogas pumping, and backed up to the content similar with the raw biogas. There was no significant amount of NH₃ detected in the raw biogas, as well as in the treated biogas. Meanwhile, the pH level of the liquid effluent had a substantial reduction, and a pH of 7.25 was obtained at the end of the biogas pumping (Figure 38b). The results elucidated that the combined operation not only efficiently removed H₂S from biogas as a key step for biogas purification, but also acidified the solution to facilitate the following EC process. The H₂S removal of biogas pumping could be theoretically explained based on the following reactions [91]:

$$H_2S = HS^- + H^+$$
$$2Fe^{3+} + HS^- = 2Fe^{2+} + S \downarrow + H^+$$
$$Fe^{2+} + H_2S + 2OH^- = FeS \downarrow + 2H_2O$$
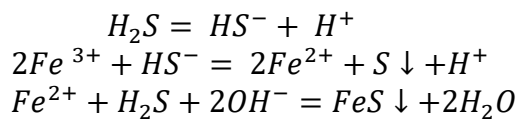
At the initial stage of biogas pumping, the abundance of hydroxyl ions (OH⁻) promoted the dissolving of hydrogen sulfide (H₂S) into water and disintegrated into hydrosulfide ions (HS⁻) and hydrogen ions (H⁺). The latter two reactions consequently occurred and functioned in H₂S fixation. The hydrogen ions (H⁺) also react with OH⁻, which drives the equilibrium of these reactions towards the right side. With formation of FeS and S, the other characteristics of the BP effluents besides pH were significantly changed as well. BP effluent had 1.87 g/L and 308 NTU of COD and turbidity, correspondingly, which were higher than 1.00 g/L and 277 NTU of NBP effluent (Table 22).

Table 22 Characteristics of 1ˢᵗ EC effluent

Parameter	NBP effluent	BP effluent
Total solids (%, w/w)	0.5±0.1ª	0.6±0.1ª
COD (mgL⁻¹)	1000±140ª	1873±23ª
TN (mgL⁻¹)	801ᵇ	777ᵇ
Turbidity (NTU)	277.0±54.1ª	308.0±14.2ª
Ionic conductivity (μs cm⁻¹)	2986.5ᶜ	4893.2ᶜ

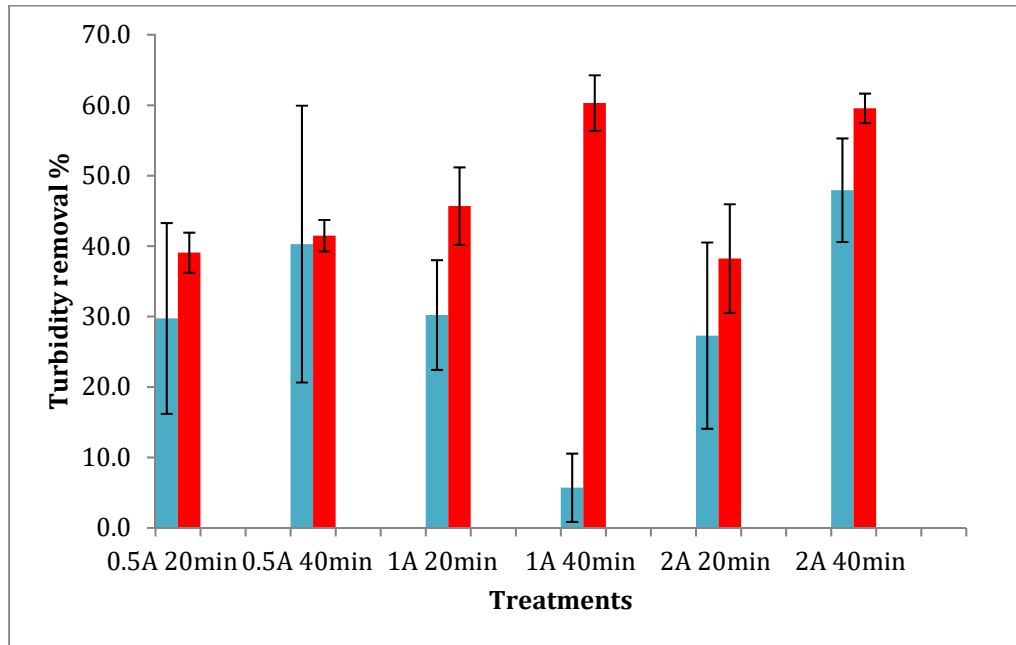a: Data represent the average of three replicates with standard deviation.

b: TN data represent the average of two replicates. TN tests were measured separately for kinetic change, and may not comply with other data set.
c: Ionic conductivity represent the average of two replicates.

4.3.1.3 The 2nd EC treatment

The 2nd EC carried on the BP effluent from the 1st EC treatment was compared with the control (NBP effluent) to further evaluate the impacts of gas pumping on the performance of the 2nd EC. The effects of I and RT on turbidity, COD removal, pH, and power consumption of the 2nd EC effluent were demonstrated in Figures 39 and 40. Turbidity removal of the 2nd EC on both BP and NBP effluent were generally enhanced with the increase of RT and I, except for the EC on NBP under 1A where the turbidity removal was decreased with increase of RT (Figure 39a). The data also demonstrated that all EC treatments on BP effluent had significantly ($P<0.05$) higher turbidity removal than the EC on NBP effluent. COD removal had a similar trend (Figure 39b). Increase of RT and I improved the COD removal of both NBP and BP effluent. The EC on BP effluent also presented obvious enhancement on COD removal compared to the EC on NBP effluent. Better turbidity and COD removal of the 2nd EC on BP effluent is partially attributed to lower pH of BP effluent (Figure 40b) that is in favor of generation of more metal ions and increase of conductivity. The metal ions react with OH^- ions in the solution to form metal hydroxide, which is one of the most important factors in removing COD and suspended solid (turbidity) via EC treatment [19]. The increased conductivity leads to low dynamic voltage (IR) drop of the electrolysis [20], therefore, less energy was needed by the EC on BP effluent. The 2nd EC on BP effluent only consumed 0.08 kWh/L (at 2A and 40 minutes) that was about half power demand of the corresponding 2nd EC on NBP effluent (Figure 40a). In addition, total nitrogen (TN) change was also different between NBP and BP effluent. BP effluent had a significantly less TN removal (15.7%) in the 2nd EC treated solution than that of NBP effluent (39.7%). Those differences are also related with the pH difference between BP and NBP effluent. As shown in Figure 40b, pH of the 2nd EC treated solution on NBP effluent remained above 9.5, which was much higher than that of BP effluent (pH around 8). There were over 80% of TN in liquid AD effluent was in the form of ammonia. Since high pH drives the equilibrium

of ammonia and ammonium towardsammonia, more ammonia was thus released from the EC of the NBP effluent that led to low TN in the solution.

(a)
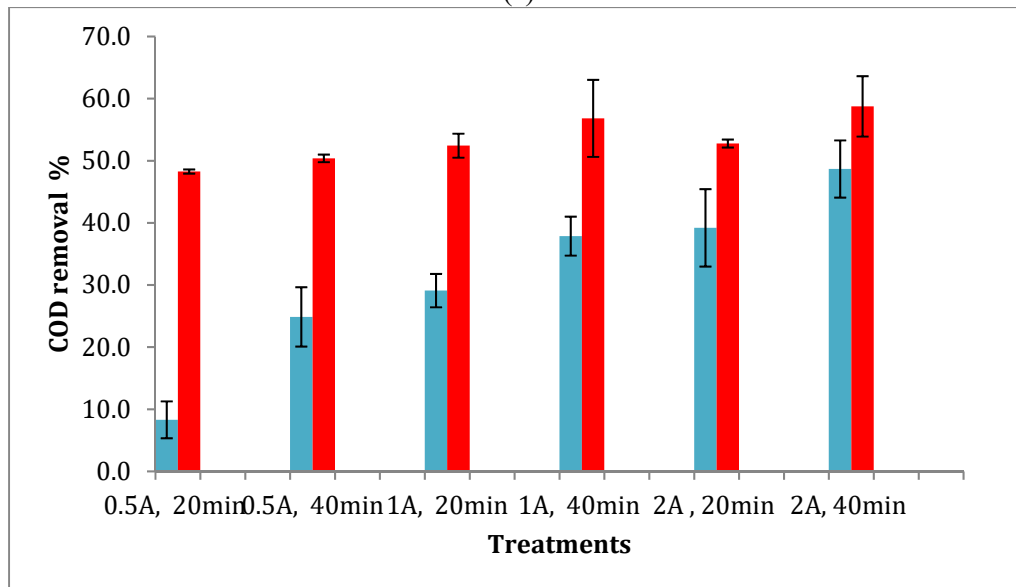
(b)

Figure 39. Comparison of COD and turbidity removal between no-biogas-pumped (NBP) and biogas pumped (BP) after 2nd EC *
Light blue square (left) stands for NBP, red square (right) stands for BP. (a) Turbidity (b) COD removal. *Data represent the average of three replicates with standard deviation.
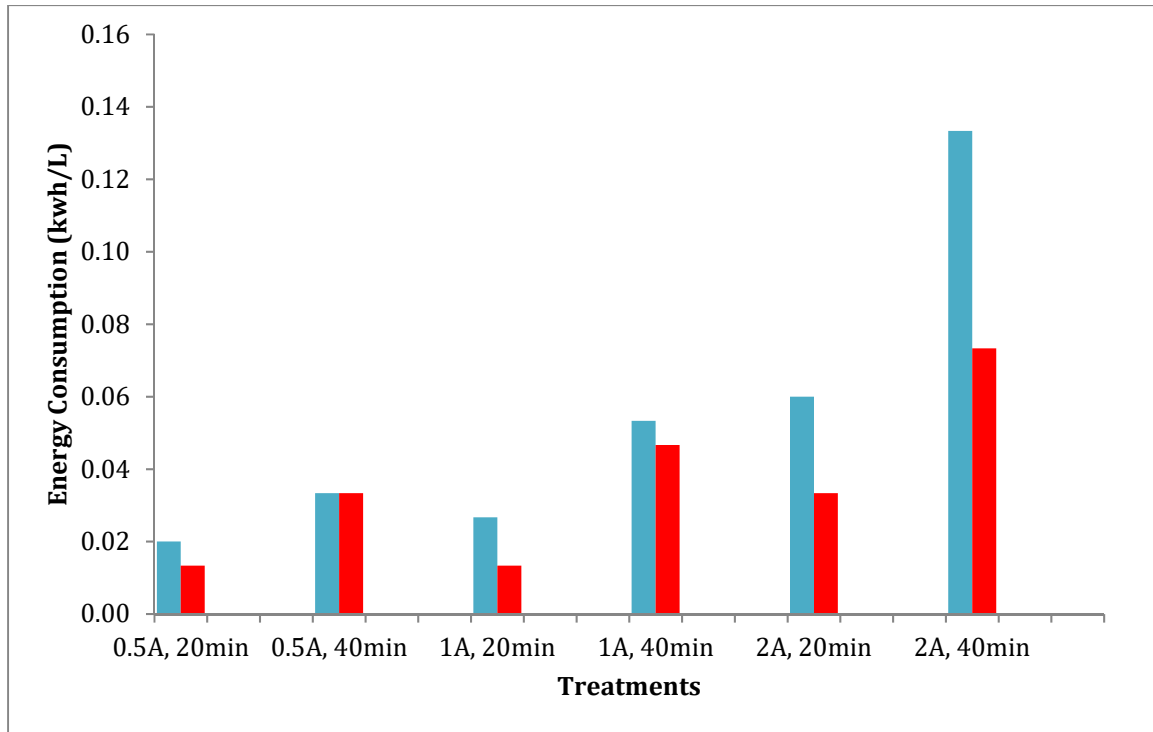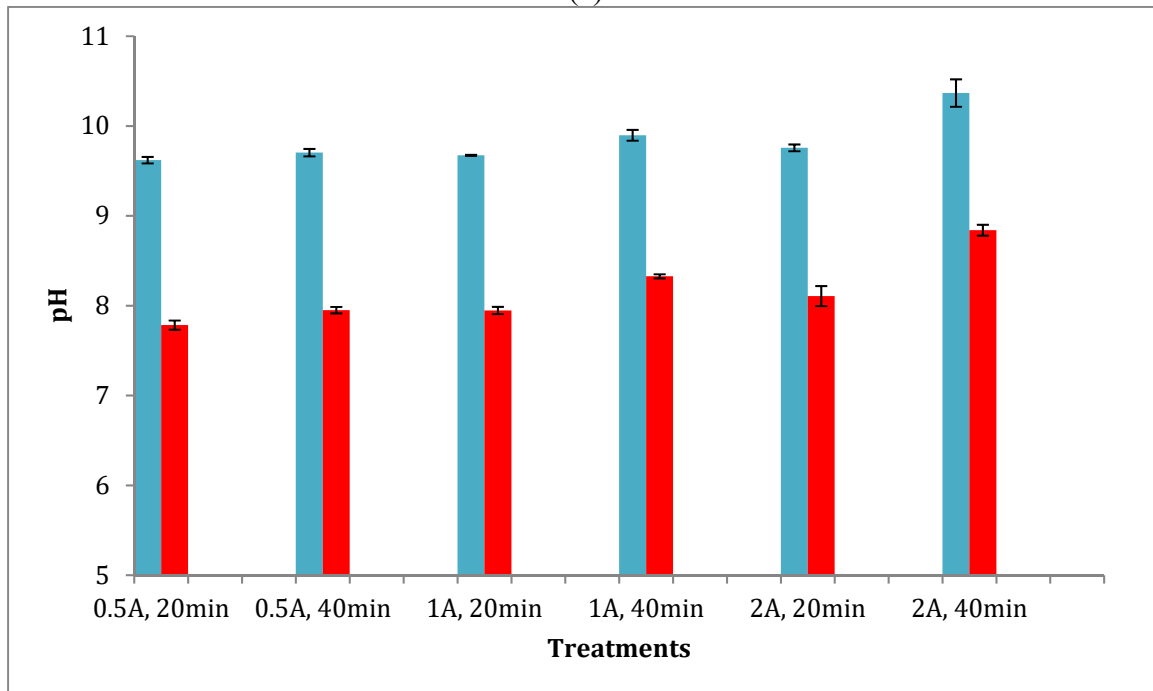
(a)

(b)

Figure 40. Comparison of power consumption and pH between no-biogas-pumped (NBP) and biogas pumped (BP) after 2nd EC *

Light blue square (left) stands for NBP, red square (right) stands for BP. (a) Power consumption, (b) pH. *Data represent the average of three replicates with standard deviation.

The pair-wise comparison based on both turbidity and COD removal indicated that the preferred EC conditions (I and RT) for BP and NBP effluents were 1A and 40 minutes, and 2A and 40 minutes, respectively. Under the preferred conditions, the 2nd EC had better effects on BP effluent (removed 56% of COD and 60% of turbidity) compared to NBP effluent (49% of COD removal and 48% of turbidity removal) (Figure 39). The solution from the preferred EC with BP had COD, TN and turbidity of 809 mg/L, 655 mg/L, and 114 NTU, respectively, and the solution from the preferred EC with NBP had corresponding numbers of 513 mg/L, 443 mg/L, and 144 NTU (Table 23).

Table 23 Characteristics of the treated solutions from two-stage EC with NBP and BP [a, b, c]

Parameter	Two-stage EC with NBP	Two-stage EC with BP
TSS (mg L^{-1})	ND	168
TDS (mg L^{-1})	2574	2106
TOC (mg L^{-1})	60	101
Color absorbance (at 527.5 nm)	0.085	0.082
COD (mg L^{-1})	513.3±46.0	808.7±116.1
TN (mg L^{-1})	443.3±56.9	655.2 ±5.9 [c]
Turbidity (NTU)	144.2±20.4	113.6±6.8
Conductivity (µs cm^{-1})	4778.8	3939.9

a: NBP treatment was carried on at I of 2A and RT of 40 min, and BP treatment was carried on at I of 1A and RT of 40 min.
b: Data represent the average of three replicates with standard deviation.
c: The number was from the run at I of 2A and RT of 40 min.

4.3.1.4 Comparison of two-stage EC processes with NBP and BP

The preferred two-stage EC processes with BP and NBP were compared to evaluate the performance of combined EC and BP approach (Table 24). The data presented that there were no significant differences on COD and TP removal between two processes. TN removal of the EC with NBP (65%) is better than the one with BP (47%) due to the effects of high pH on the formation of volatile ammonia nitrogen (released during the EC treatment). The liquid recovery of the EC with NBP (55%) was also better than that with BP (34%).

Table 24. Comparison of the selected multiple-stage EC processes with BP and NBP

Parameter	Two-stage EC with NBP[c]	Two-stage EC with BP[d]
COD removal (%)[a]	94.3±0.5	91.0±1.3
TP removal (%)[a]	100	100

TN removal (%)[a]	64.7±6.3	46.9±0.5[c]
TSS removal (%)[e]	>99.9	95.9
TOC removal (%)[e]	97.4	95.7
Color reduction (%)[e]	88.2	88.6
Liquid recovery (%) [b]	54.9±1.5	34.0±6.5
Overall energy consumption (kwh/L treated solution)	0.25	0.16

a: Removal was calculated based on unit volume of solution. Data represent the average of three replicates with standard deviation.
b: Recovery was calculated based on the volume of the initial solution. Data represent the average of three replicates with standard deviation.
c: This set of data was derived from 2nd EC with I of 2A and RT of 40 min.
d: This set of data was derived from 2nd EC with I of 1A and RT of 40 min.
e: Data represent the average of two replicates.

As shown in Figure 41, the turbidity and color of EC solution without BP was gradually improved from 1st EC to 2nd EC. A transparent and light yellow solution was obtained after the 2nd EC (Figure 41a). After the biogas pumping, the color of the solution turned into black, and the turbidity was higher than the original AD liquid effluent (Figure 41b) that was caused by the generation of ferrous sulfide (FeS) and sulfide (S) from reactions of ferric/ferrous ions and H_2S. The dark color and high turbidity of the BP solution had less influence on the transparency of the final treated solution. There was no significant difference on color between NBP and BP treated effluent (Table 23). The turbidity of the BP solution after 2nd EC was lower than the NBP solution (Table 23). Furthermore, analyses of TSS and TOC also demonstrated that high removal efficiencies of TSS and TOC were obtained for both NBP and BP treatments (Table 24). As for ionic conductivity, the significant reduction during the 1st EC treatment showed a good removal of dissolved solids in the AD effluent (Table 22). Biogas pumping greatly increased the ionic conductivity, which indicated that the physiochemical properties of EC solution was changed by biogas pumping, and more conductible ions became available. The fine and relatively coarse particles were observed in the settlement of the EC with BP, which also indicated that H_2S might influence the formation of flocculation and clarity of the treated solution during the 2nd EC as well. An in-depth study is on-going at the authors' research group to understand this change. Moreover, the EC with NBP (0.25 kwh/L) consumed much more energy than the EC with BP (0.16 kwh/L) (Table 24).

(a)

(b)

Figure 41. Turbidity and color change of the solution during electrocoagulation processes (a) Left to right: AD effluent, solution after 1st EC, supernatant after 2nd EC. (b) Left to right: AD effluent, solution after 1st EC and biogas pumping, supernatant after 2nd EC

Table 25. Mass balance analysis

Mass balance			Volume (mL)	TN^a (mg)	TP^a (mg)	Fe^b (mg)	S (mg)^b
1st EC stage	Input	AD effluent	500	616.7 ± 50.3	170 ± 8.7	19.4 ± 1.0	-
		Electrodes loss	-	-	-	2100 ± 100	-
	Output	1st EC sludge & other loss	196.7 ± 5.8	344.2 ± 62.4	170 ± 8.7	2017.8 ± 79.1	-
		1st EC solution	303.3 ± 5.8	272.5 ± 48.3	0	101.6 ± 37.9	-
2nd EC stage with NBP^c	Input	1st EC solution	500	400.5 ± 2.1	-	142.8 ± 6.7	-
		Electrodes loss	-	-	-	1333.3 ± 57.7	-
	Output	2nd EC sludge & other loss	47.8 ± 1.9	182.4 ± 14.8	-	1473.0 ± 59.1	-
		2nd EC solution	452.2 ± 1.9	218.1 ± 48.3	-	3.2 ± 0.5	-
2nd EC stage with BP^c	Input	1st EC solution	500	388.5 ± 61.5	-	135 ± 11.3	3.8 ± 0.1
		Electrodes loss	-	-	-	633.3 ± 115.5	-
	Output	2nd EC sludge & other loss	68.3 ± 7.1	105.7 ± 35.4	-	741.6 ± 110.3	-
		2nd EC solution	431.7 ± 7.1	282.8 ± 7.1	-	26.7 ± 8.1	0

a: Data represent the average of three replicates with standard error; TP data are average of two replicates;

b: Data are from EC treatments on a different batch of AD effluent, and represented the average of three replicates with standard error;

c: 2nd EC condition for NBP group was 2A of I and 40 minutes of RT; 2nd EC condition for BP group was 1A of I and 40 minutes of RT.

The mass balance analysis shows that the total iron losses for NBP and BP were 3,433 and 2,733 mg per run, respectively (Table 25), and over 95% of the consumed iron precipitated down and mixed into the sludge for EC with either NBP or BP. Nitrogen removal from the AD effluent by EC with NBP and BP were 65% and 54%, respectively (Table 25). Evaporated ammonia at high pH during the EC and ammonium/nitrite salts adsorbed by sludge could be the main causes of nitrogen removal during the EC. Since the pH for the 2nd EC after BP was lower than that after NBP, the nitrogen removal of EC with BP was not as efficient as EC with NBP. The sulfur analysis during the EC with BP showed that 1 L of EC solution was capable of adsorbing 7.6 mg sulfur in 60 minutes at a biogas flow rate of 0.5 L/min with a H_2S concentration of 300 ppm, and there were no sulfide ions detected in the solution after 2nd EC operation. The H_2S absorption data demonstrate that combining EC with BP could have a biogas

clean-up capacity of up to 60 L biogas (with a H_2S concentration of 300 ppm) per 1 L EC solution.

Combining biogas cleanup and AD effluent reclamation not only demonstrates a potential in facilitating EC process by reducing power consumption, but also provides an alternative of H_2S removal for biogas purification. Under the preferred conditions, 90% of COD and 100% TP in AD effluent were removed. Implementation of the biogas pumping operation reduced about 36% of overall power consumption compared with that without biogas pumping. This integration provides a new approach to simultaneously reclaim AD effluent and remove H_2S from biogas, which well addresses the downstream challenges of anaerobic digestion and further advances the adoption of AD technology on waste management.

4.3.2 Evaluating a bench-scale electrocoagulation unit

The TS and COD of the feed were 0.75% and 4,600 mg/L. The current applied on the EC unit was 19.5 amperes of direct current. Voltage was recorded during the experimental runs. A 100 ml sample was taken every 30 minutes. During the experimental run, the voltage was gradually increased (Table 26). The average voltage was approximate 8.5 volt. The chemical analyses present that The COD reduction is inversely correlated with a change in voltage (Figure 42). As the voltage increased, the COD reduction started to decrease. At the end of the test, the drastic change in voltage correlated to a plateau in COD removal. The EC reaction had an overall COD reduction of 79.1%. In addition, phosphorus removal was also monitored (Figure 43). The EC reaction efficiently removed TP as well (Figure 43). The TP reduction was reached at 92.6% during 240 minutes of the reaction. Similar to the TP and COD reduction, TS was gradually settled down throughout the experiment (Figure 44). The final TS reduction was 70.5%. The corresponding TS in the EC solution was 0.2%.

Table 26. Voltage change of the EC operation

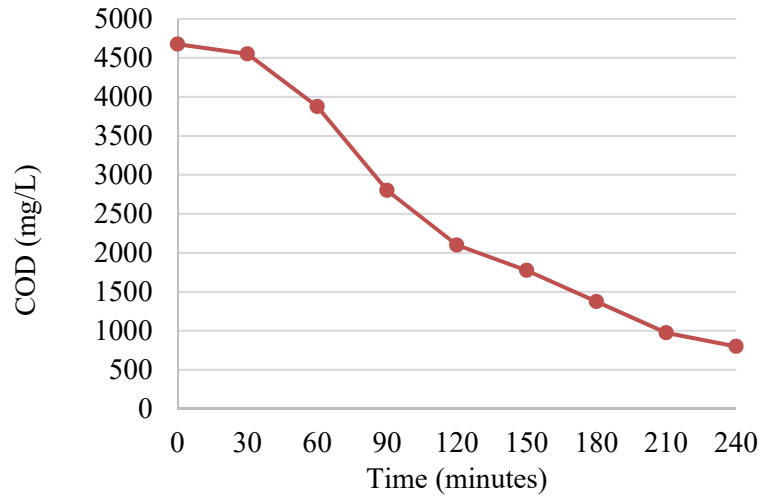| Time (Min)	Voltage (V)	Current (A)
0	7	19.5
30	7	19.5
60	7.1	19.5
90	7.4	19.5
120	7.6	19.5
150	8	19.5
180	8.3	19.5
210	8.6	19.5
240	9.3	19.5

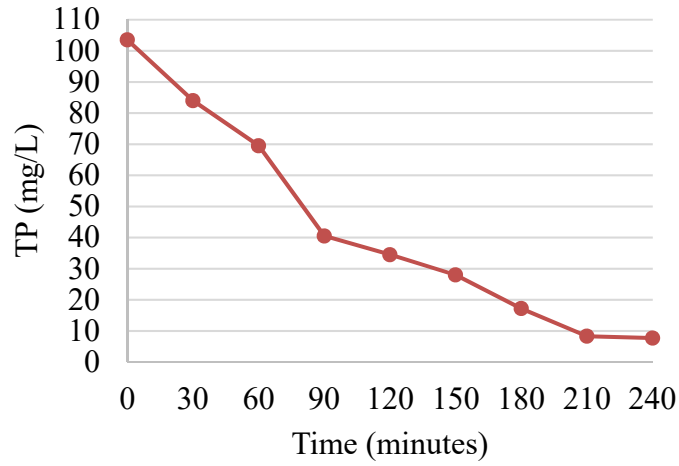Figure 42. COD reduction during the EC reaction

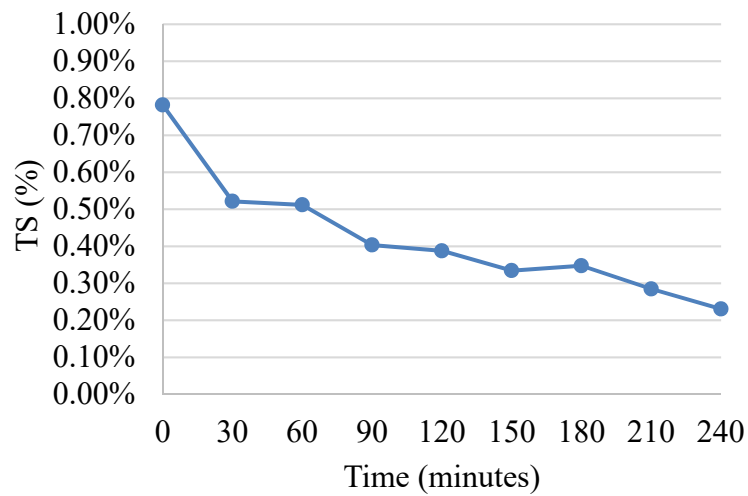
Figure 43. TP reduction during the EC reaction

Figure 44. TS reduction during the EC reaction

4.4 Investigating nano-filtration on potable water generation from EC solution
4.4.1 EC treatment of AD effluent

The characteristics of AD liquid effluent and EC treated AD effluent were listed in Table 27. After a two-stage EC treatment [65], a transparent solution was obtained, and 97% of COD was removed. The COD of the EC treated AD effluent was 330 mg/L. Even though the EC treatment demonstrated excellent efficiencies of solid and COD removal, COD in the EC treated AD effluent was still higher than the EPA's wastewater treatment standards. Further treatments are needed to remove the residual COD and other compounds in order to meet the EPA's standards. Membrane-based filtration was therefore employed to remove the COD from the EC treated AD effluent.

Table 27. Characteristics of the AD liquid effluent and filtered EC treated AD liquid effluent (post vacuum filtration)

Parameters	AD liquid effluent*	EC-treated AD liquid effluent (post vacuum filtration)
pH	7.5-8.0	9
TS (w/w %)	0.90	--
COD (mg L^{-1})	10017	330
TP (mg L^{-1})	340	1.18
TN (mg L^{-1})	1233	150
TOC (mg L^{-1})	2332	100

*: The AD liquid effluent for EC pretreatment was made by diluting the raw AD liquid digestate five times.

4.4.2 Performance of commercial membranes on the EC treated AD liquid effluent

NF 270, NF 90, and BW 30 were tested on the EC treated AD liquid effluent to compare their permeability and COD reduction. The experimental data demonstrate that the NF 270 membrane had the highest pure water flux and solution permeability among the three membranes, while BW 30 showed the highest COD removal (Figures 45 and 46). It has been reported that pH of sample has significant influence on the separation behavior of the membranes [92]. The original pH of the EC treated AD liquid effluent was around 9. The pH of the EC effluent was adjusted to 3 in order to evaluate the effect of pH on the permeability and COD reduction. As shown in Figure 2, NF 270 membrane had higher COD reduction at acidic pH than alkaline pH. The solution permeability of NF 270 membrane was also lower at acidic pH than alkaline pH (Figure 46b). The remaining two membranes did not show significant ($P > 0.05$) difference in COD reduction under different pH. Both NF 90 and BW 30 had much lower solution permeability than NF 270, and there is no significant ($P > 0.05$) difference on the permeability between both membranes under either acidic or alkaline environment (Figure 46b).

The effect of pH on membranes, especially on NF 270 membrane, can be interpreted based on the membrane surface properties as well as characteristics of the EC treated AD liquid effluent. NF90 and BW30 are dense non-porous membranes compared to NF 270 membrane, which is a loose porous membrane. Even though all three membranes have positive charge at acidic conditions and negative charge at alkaline conditions, the responses of the NF 90 and BW 30 membranes to changes of effluent properties are different than the NF 270 membrane.

Natural organic matters (NOM) are present in almost all types of wastewater samples and the EC-treated AD effluent is no exception. Total organic carbon (TOC) analysis confirmed the presence of organic matter in the EC effluent in a significant proportion (100 mg/l). Among the various types of NOMs present in the solution, it has been reported that the humic compounds are largely responsible for the pH-dependent behavior of the effluent. [93-96]. As the humic compounds play critical roles as electron mediators in microbial electron transfer and respiration during anaerobic digestion [97], their concentration in the AD effluent is relatively high, and the EC treatment is not able to remove all of them. Consequently, a certain amount of them remain in the EC treated AD liquid effluent. Previous studies have shown that at acidic pH, humic compounds lose most of their charge resulting in their aggregation[95], and alkaline pH leads to their dissolution in the solution. For dense membranes like NF 90 and BW 30, the size changes of the compounds have little influence on their performance. This is the reason why there were no significant (P > 0.05) differences on COD removal and solution permeability between NF 90 and BW 30 regardless of pH changes. The NF 90 and BW 30 membranes showed around 92-95% COD reduction with the COD concentration of approximately 21 ppm in the final filtrate, but extremely low solution permeability of around 0.6 l/m^2·hr·bar.

As for NF 270 membrane, it was apparent that both membrane surface properties and characteristics of the EC treated effluent had significant influence on the performance of NF 270 membrane. Under acidic conditions, the humic compounds were inclined to settle down on the membrane surface, resulting in lower permeability of the NF 270 membrane at pH = 3 than pH = 9 (Figure 46a). However, the deposition of humic compounds created an additional layer that prevented the passage of the remaining humic compounds and other fine particles in the effluent, so that the COD reduction of the membrane was improved (Figure 2). On the other hand, at alkaline pH, humic compounds were dissolved in the solution. Relatively large pore size of NF 270 is not able to block the dissolved humic compounds and other fine particles, even though there was charge-based repulsion between negatively charged humic compounds and NF 270 membrane surface. Consequently, the COD removal was greatly reduced and the solution permeability was enhanced under alkaline pH conditions. Considering the fact that loose surface structure provides some flexibility for the following LbL coating experiments, NF 270 was selected as the underlying substrate for fabricating the PEM membranes.
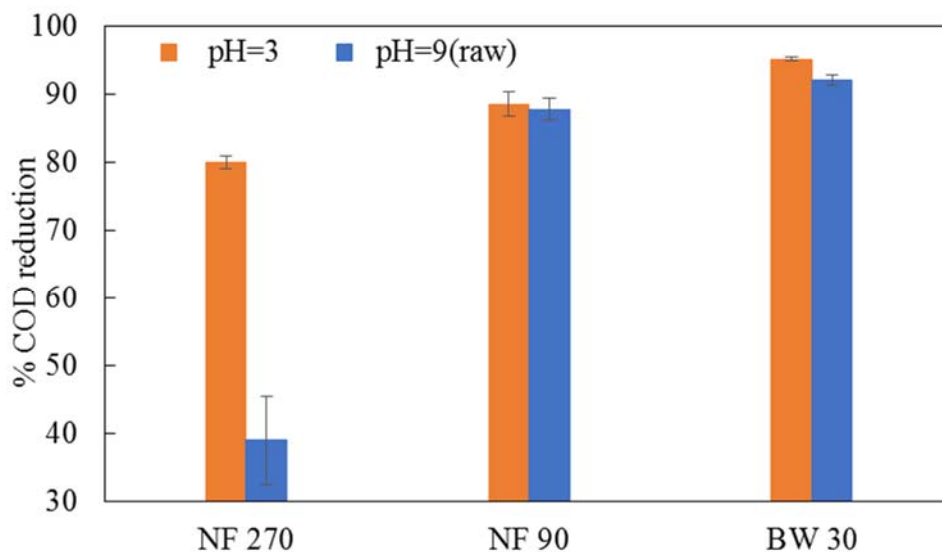
Figure 45. Comparison in COD reduction between the commercial membranes.
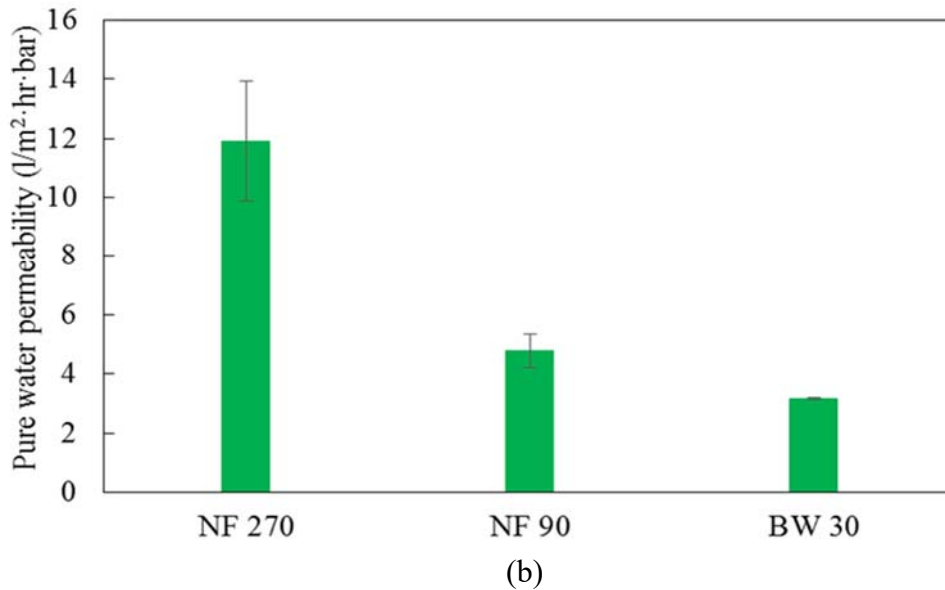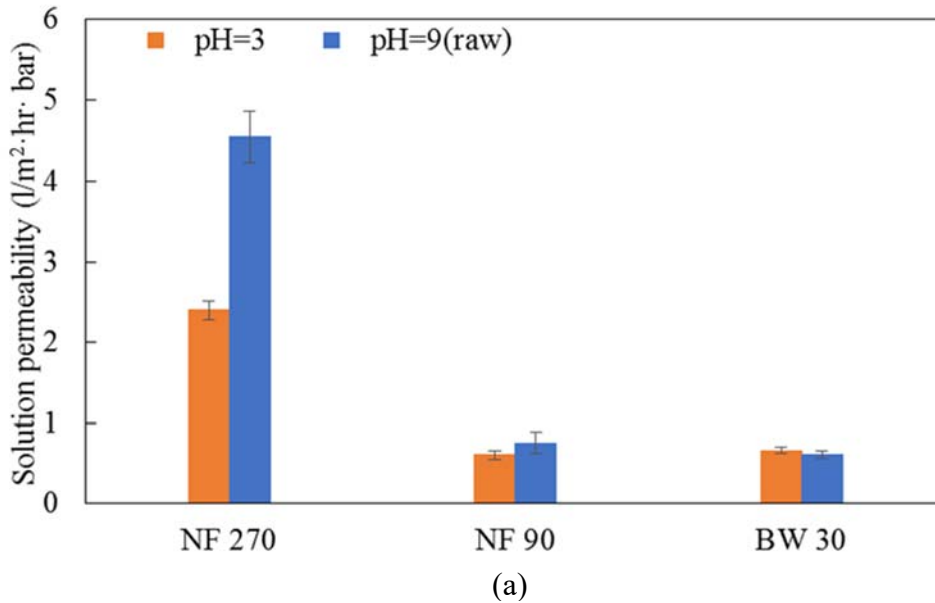

(a)

(b)

Figure 46. Permeability comparisons between the commercial membranes based on (a) solution tested under two different pH conditions and (b) pure water.

4.4.3 Performance of PEM-based membranes on EC-treated AD effluent
4.4.3.1 [PDAC (0.5 M NaCl)/SPS (0.5M NaCl)] $_{5.5}$ multilayer system

Both PDAC and SPS are strong polyelectrolytes, which remain charged over a wide range of pH. 0.5 M NaCl was used as the supporting electrolyte which helps increase the surface charge density [98]. The surface charge plays an important role in shaping the rejection behavior of these polyelectrolyte-based membranes, especially while dealing with the removal of charged species. Under acidic conditions, as the humic compounds lose most of their charge, effect of the charge on the outermost layer is minimal. It was, however, important to learn how the charge on

the outermost layer affects the rejection once humic compounds are negatively charged under alkaline conditions. Two different PEM multilayer systems were investigated to treat the EC treated AD liquid effluent at pH 9: the first one comprising of 5 bilayers of PDAC/SPS ending with SPS (negatively charged), and the second one consisting of 5.5 bilayers of PDAC/SPS ending with PDAC (positively charged). The experimental data demonstrate that the 5.5-bilayer system ending with PDAC had higher COD reduction (~ 84 %) than the system ending with SPS (~70 %) (Figure 47). Under alkaline condition, the negatively charged humic compounds bind to the positively charged PDAC layer and form an additional barrier layer that helps enhance the rejection, while, the system ending with a SPS layer mainly uses charge-based repulsion to reject the negatively charged humic compounds. Therefore, under alkaline conditions, the barrier layer formation by humic compounds on a positively charged surface is more instrumental in COD reduction than charge-based repulsion that occurs with a negatively charged outermost layer. Based on the performance results, the multilayer membrane ending with PDAC was chosen over the one ending with SPS, and used for the following experiments. The number of bilayers is also a tunable factor for the LbL process. 5.5 was the optimal number of bilayers to reclaim the EC treated AD liquid effluent and achieve high permeability and rejection.
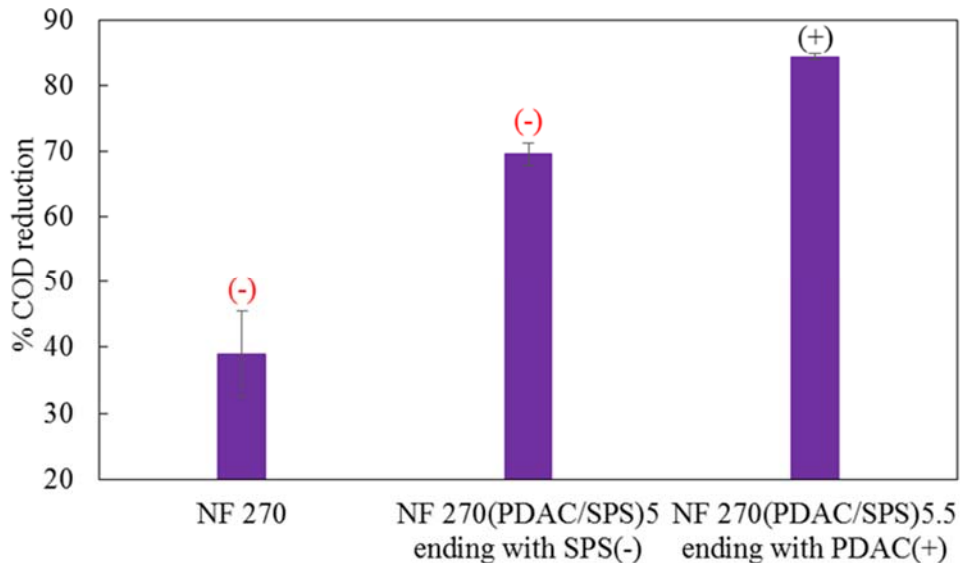

Figure 47. COD reduction of two PDAC/SPS based modified membranes.
(-) Bare NF270 or Multilayer assembly on NF270 ending with negatively charged SPS outer layer.
(+) Multilayer assembly on NF270 ending with positively charged PDAC outer layer.

The performance of the PDAC/SPS–based modified membranes was further compared with the commercial membranes. The modified membranes showed around 84% COD reduction at pH = 9 and 90% at pH = 3 with corresponding COD values of 33 and 51.5 ppm in the filtered solution (Figure 48), which were significantly better than the original NF270. Permeability experiments demonstrate that the pure water permeability of the PDAC/SPS coated NF 270 membrane was significantly ($P < 0.05$) higher than NF 90 and BW 30 membrane (Figure 49b). The modified membrane also showed superior solution permeability than BW 30 and NF 90, which was approximately 3 times higher than BW30 and NF 90 at pH 3 and 5 times higher than BW30 and NF90 at pH 9 (Figure 49a). Similar to the control NF 270 membrane, the PDAC/SPS

based membranes also had lower solution permeability at acidic pH as compared to alkaline pH (Figure 49a). As aforementioned, the formation of a barrier layer of humic compounds on the membrane surface was a key factor influencing the flux. However, the attachment mechanisms of barrier layer under acidic and alkaline conditions are different. Under acidic condition, the layer is formed due to the aggregation and settling of the humic compounds on the membrane surface. Under alkaline condition, the negatively charged humic compounds adhere to the positively charged surface by electrostatic attraction. Given that the flux is lower under acidic condition, we can assume that the barrier layer formed at pH 3 was thicker and denser than what was formed at pH 9. Owing to the thicker barrier layer, the rejection of the membrane was higher under acidic condition. The deposition of PDAC/SPS multilayers led to a considerable enhancement in the COD reduction compared to the control NF 270 membrane. The percentage reduction was almost equal to that of BW 30 membrane under acidic conditions but lower than BW 30 under alkaline conditions. Covalently cross-linked multilayer structure was then studied in order to further improve the membrane performance.
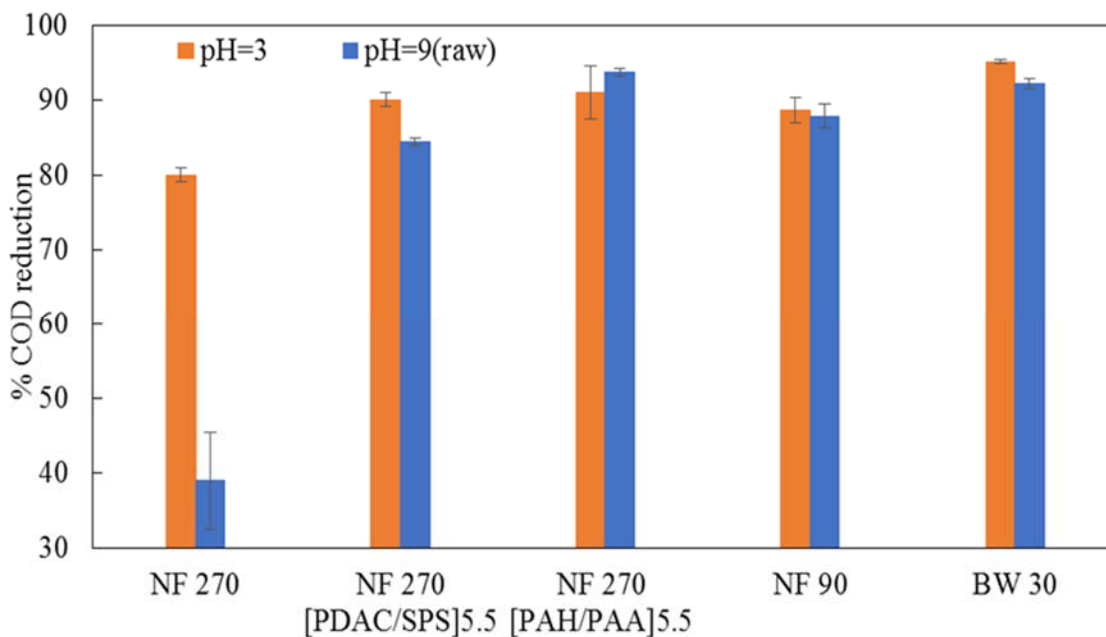

Figure 48. Comparison in COD reduction between the modified membranes and the commercial membranes at different pH conditions.

(a)

(b)
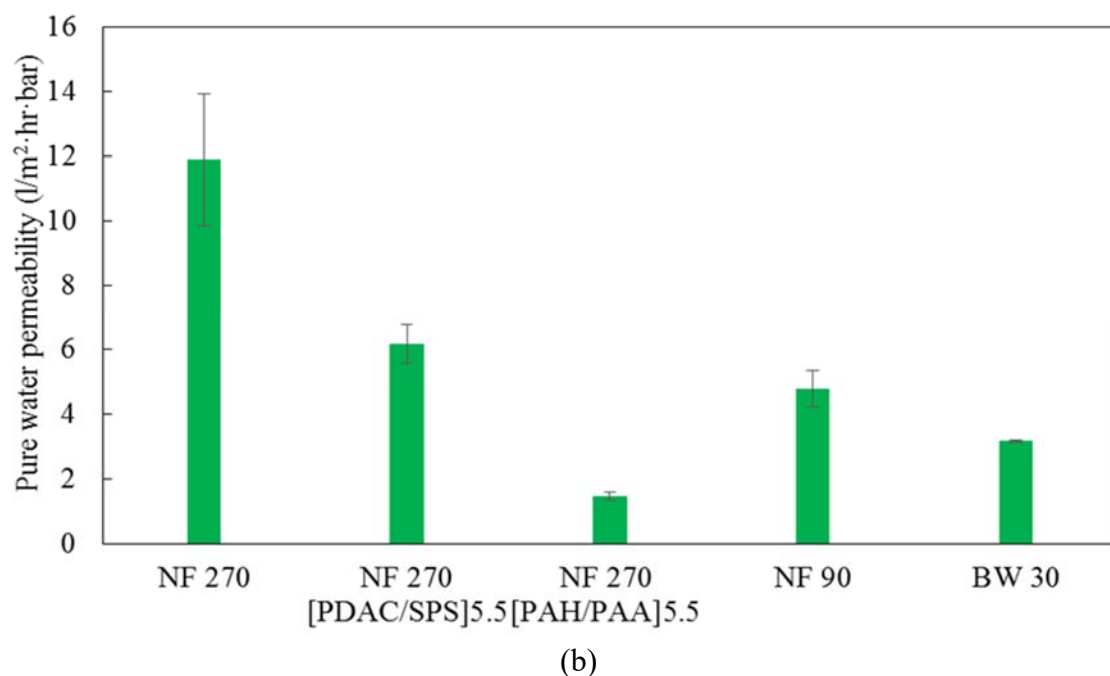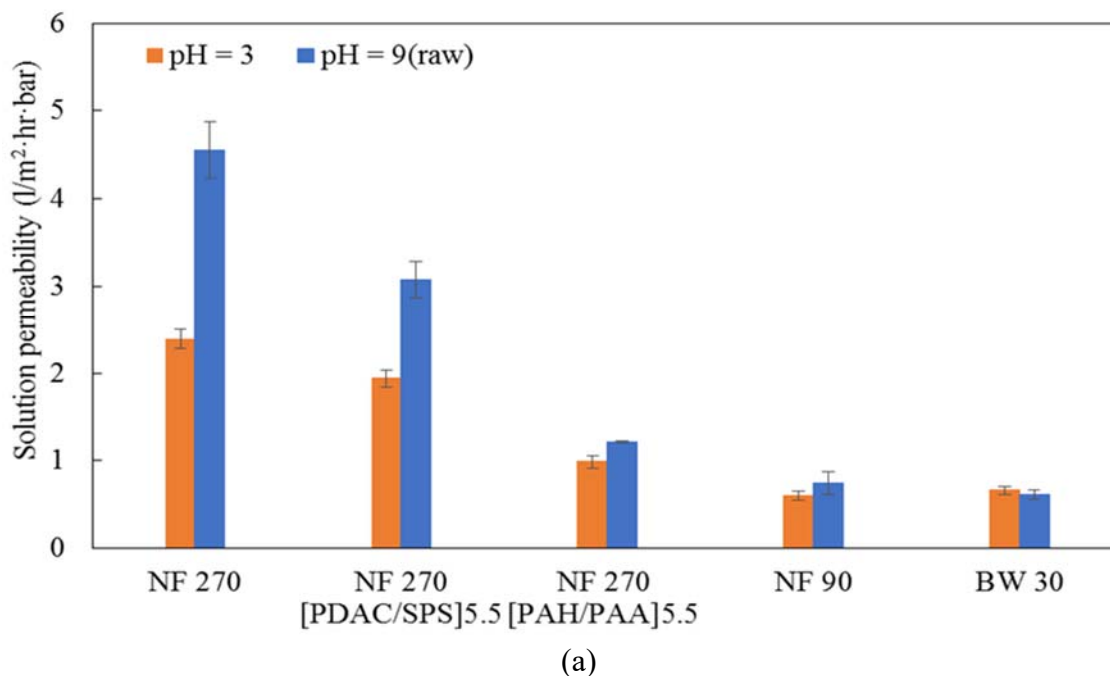
Figure 49. Permeability comparisons between the modified membranes and the commercial membranes based on (a) the solution using at two different pH conditions and (b) pure water

4.4.3.2 [PAH (pH 8.5)/PAA (pH 3.5)] $_{5.5}$ multilayer system

Since covalent cross-linking can provide a tightly woven network, which is capable of blocking unwanted components of wastewater by "sieving "mechanism much more efficiently than ionic cross-linking, a covalently cross-linked multilayer structure was coated on the surface of the NF 270 membrane. The polyelectrolytes, PAH and PAA, were used to construct such coatings.

Both PAH and PAA are weak polyelectrolytes that exhibit pH-tunable behavior. When PAH is at pH 8.5 and PAA at pH 3.5, they form thick loopy films with inter-penetrated layers [99]. The amine groups of PAH and the carboxylic groups of PAA can be reacted to form covalent linkages between them. This can be simply done by heating the multilayers up to a high temperature (>180 °C) [100]. However, due to the fact that the underlying NF 270 membrane cannot tolerate such high temperature, EDC induced chemical cross-linking was applied. [101]. A high EDC concentration of 50 mg/ml was used to ensure the desired cross-linking density [101]. In order to enable comparison with the PDAC/SPS –based membrane, the same number (5.5) of PAH bilayers was deposited.

The performance of the PAH/PAA-based modified membrane was presented in Figure 5. The COD reduction was between 91-95% under both acidic and alkaline conditions, and the final COD concentration was not significantly ($P > 0.05$) different from that of BW 30 membrane. This could be attributed to a tight dense polymeric network that was formed by crosslinking PAH (pH 8.5) and PAA (pH 3.5), which is capable of completely blocking the passage of the unwanted components. The pure water permeability of the PAH/PAA membrane was the lowest among the tested membranes (Figure 49b), while the solution permeability at both pH conditions was higher than BW 30 and NF 90 membranes (Figure 49a). The thick layers of PAH/PAA coating contributed to the low pure water permeability of the modified membrane. In spite of having a lower pure water flux, the PAH/PAA coated NF 270 membrane showed 1.7 times higher permeability than the BW 30 membranes. It might be caused by lower fouling propensity of the PAH/PAA coated membrane in comparison to the commercial RO membranes. In addition, due to the tight dense polymeric network and thick layer of the coating, the deposition of an additional layer of humic substances by pH changes did not contribute much to the rejection. Therefore, there were no significant differences on COD reduction and solution permeability between acidic and alkaline conditions. Compared to the PDAC/SPS system, the PAH/PAA multilayer membrane had the same COD reduction ($P > 0.05$) at acidic pH, but higher reduction at alkaline pH ($P < 0.05$). The flux was however, lower than the latter system. However, the pH-independent characteristics of the PAH/PAA multilayer system makes it very useful for treating the EC treated AD liquid effluent. This eliminates the need of adjusting pH of the wastewater solution for the treatment, and in turn prevents severe fouling by humic compounds under acidic conditions.

The ratio of solution flux over initial pure water flux could be used as a criterion to evaluate anti-fouling property of different membranes. A higher ratio indicates better fouling resistance offered by the membrane surface. The PEM membranes (PDAC/SPS and PAH/PAA) showed better anti-fouling than their commercial counterparts (Table 28).The creation of anti-fouling surfaces by the deposition of polyelectrolytes has been reported earlier as well [102-105]. Among all the membranes, the PAH/PAA-based membranes had the best anti-fouling performance under both pH conditions. In this context it should also be noted that, apart from humic compounds, NOMs also consist of a significant hydrophilic fraction that can lead to irreversible membrane fouling[106]. Membranes with a higher degree of hydrophilicity are therefore more prone to organic fouling[107]. This could be one of the reasons for the PAH/PAA membrane (contact angle around 59°) having lower organic fouling propensity than the more hydrophilic PDAC/SPS system (contact angle around 37°).

Table 28. The ratio of the average solution flux to the average initial flux for commercial membranes and the PEM membranes*

Membranes	$J_s(50)/J_w(0)$ at pH = 3	$J_s(50)/J_w(0)$ at pH = 9
NF 270	0.201	0.382
NF 270 modified with (PDAC/SPS)5.5	0.315	0.500
NF 270 modified with (PAH/PAA)5.5	0.678	0.829
NF 90	0.125	0.157
BW 30	0.209	0.193

$J_s(50)$: The solution flux of the membrane measured by calculating the time taken to filter 50 ml of the permeate solution
$J_w(0)$: The pure water flux or the initial flux of the membrane
*: Both the fluxes were normalized with respect to the pressure applied during the measurements

     With the combination of EC and membrane filtration, the color of the AD effluent was completely removed (Figure 50). This is important from the point of view of producing potable water. The EC process greatly removed the majority of the COD and TS in the AD effluent. The following membrane filtration step further decolored and cleaned the EC treated AD effluent. A relatively low energy-demand high-strength wastewater treatment is therefore achieved.

Figure 50. Color change of the solution following different treatment stages
Left to right: AD effluent, EC effluent and membrane filtrate.

4.4.4 Effect of the coating properties on the membrane performance
4.4.4.1 Thickness of the PEM coatings

     The thickness of the coatings plays an important role in determining the permeability of the modified membrane. The strong polyelectrolytes PDAC and SPS are fully charged

irrespective of pH conditions. The strong ionic linkages between the positively charged PDAC backbones and negatively charged SPS lead to the formation of very thin flat coatings (Table 29). The addition of NaCl increases the surface charge density by virtue of "extrinsic charge compensation" within the polyelectrolytes [108]. This, however, increases the thickness of the films [109]. PAH and PAA exhibit pH dependent ionization behavior. PAH is around 50% ionized at a pH of 8.5, and PAA is only about 10% ionized at pH of 3.5 [110]. Since they are only partially charged, they arrange themselves in a coiled conformation along with a high level of interlayer diffusion to enable charge compensation [99], which leads to thick loopy films with a high degree of swelling. Crosslinking polyelectrolytes was used to reduce the swelling and corresponding thickness [111]. It is apparent that thickness of the coatings directly affects the permeability. The thicker PAH/PAA coatings had lower initial permeability than the PDAC/SPS-based coatings.

Table 29. The thickness values of the two types of polyelectrolyte coatings on NF 270 membrane

Type of coating	Thickness (nm)
[PDAC (0.5M NaCl) / SPS(0.5M NaCl)] $_{5.5}$	28.70 ± 4.66
[PAH (pH 8.5) / PAA (pH 3.5)]$_{5.5}$	134.15 ± 9.87

4.4.4.2 Surface charge of the PEM coatings

Surface zeta potential of membranes plays an important role in determining the membrane rejection properties. The zeta potentials of all three commercial membranes as well as two modified membranes under three different pH conditions (acidic, neutral and alkaline) are listed in Table 30.

Table 30. The streaming potential data for the commercial membranes and the modified membranes as a function of pH*

Membrane	Surface zeta potential (mV) @ pH 3	Surface zeta potential (mV) @ pH 7	Surface zeta potential (mV) @ pH 9
NF 270	5.54 ± 0.13	$- 4.17 \pm 1.89$	-21.35 ± 0.36
NF 270 modified with (PDAC/SPS)$_{5.5}$	20.38 ± 1.66	29.24 ± 2.45	20.07 ± 5.86
NF 270 modified with (PAH/PAA)$_{5.5}$	20.50 ± 4.47	12.83 ± 2.30	10.26 ± 3.36
NF 90	20.91 ± 0.99	$- 15.74 \pm 0.09$	-15.33 ± 0.23
BW 30	12.70 ± 3.80	$- 4.70 \pm 1.45$	-3.66 ± 0.45

*: Data represent average of three replicates with standard deviation.

The PEM membranes remain positively charged throughout the entire pH range of 3-9, unlike the commercial membranes. For the PDAC/SPS system, the outermost PDAC layer remained almost fully ionized and therefore imparted positive charge to the membrane outer surface in the tested pH range, which leads to small variation between different pH conditions (Table 30). For the PAH/PAA system, the effect of pH is much more complicated since both polyelectrolytes have pH dependent ionization. When exposed to a pH of 3, the outermost PAH layer was fully ionized and therefore had the highest positive charge. With the decrease in

percentage ionization, the surface zeta potential also decreased as the pH was increased (Table 30). However, this polyelectrolyte system has much more complicated phenomena associated with it like the inter-diffusion of polyelectrolytes [112] and shifting of the pK_a value of the polyelectrolyte [110] when incorporated within the multilayer assembly. Besides, the effect of cross-linking on the ionization of the weak polyelectrolytes not been thoroughly studied to date.

The results concluded that combining electrocoagulation and membrane separation is able to efficiently reclaim a high-strength wastewater - AD liquid effluent. The pH of the wastewater solution played a pivotal role in determining the performance of the membranes mainly due to the NOMs in the EC effluent. Both PDAC/SPC and PAH/PAA based membranes had better solution permeability than the commercial reverse osmosis membrane (BW 30). The PAH/PAA-based membrane showed better COD reduction than the PDAC/SPS based membrane and equal reduction as BW 30 membrane. Both polyelectrolyte-based membranes had much lower fouling propensity than the commercial membranes, which provides a potential membrane-based solution to treat high-strength wastewater.

4.5 Evaluating performance of the pilot-scale system
4.5.1 Biogas production

Figures 51 and 52 illustrate the performance of the upflow fixed-film digesters during a 12 weeks continuous operation. With 60 L feed (2.2% TS, 1.86% VS, 2,001 mg/L TN, and 690 mg/L) per day, average biogas production of 787 L per day was achieved with a corresponding methane content of 68% (methane production of 549 L per day) (Figure 51). The TS and VS were reduced to 0.68% and 0.44% in the AD effluent, respectively (Figure 52). The TS and VS removal of 71% and 76% were achieved by the uplfow fixed-film digesters. Correspondingly, a methane productivity of 644 L/kg VS reduced was achieved. The pH of the digestion was steady at 7.9 and no external pH adjustment was needed, even though the feed had a relatively low pH at 5.5. The strong buffer capacity indicates that stable and robust anaerobic microbial communities have been established in the pilot upflow fixed-film digesters.
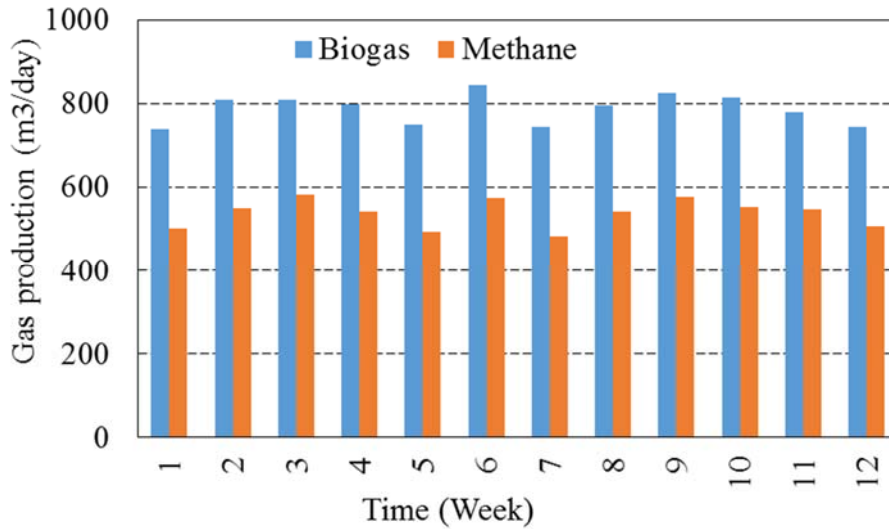
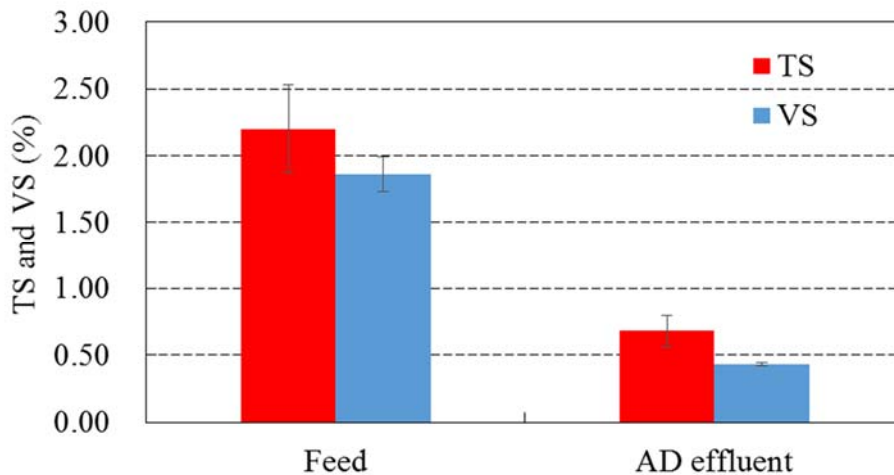Figure 51. Biogas production of the upflow fixed-film digesters

Figure 52. TS and VS changes during the digestion

Besides the continuous digestion test, the stability of the digestion has been studied as well. The effects of feeding and temperature on biogas production were tested. Figure 53 shows the effects of feeding on biogas production. The biogas production dropped to 67 L/day a week after the feeding was stopped. The feed was resumed after three weeks of no feeding. The biogas production quickly came back to 702 L/day in two weeks. In addition, the effect of temperature on the biogas production was also studied (Figure 54). Reducing the culture temperature to 20°C negatively impacted the biogas production. One week after the temperature change, the biogas production was dropped to 240 L/day while the feeding was still maintained at 60 L/day. After three weeks culture at 20C, the temperature was raised back to 35°C. The biogas production was gradually increased back to 741 L/day. Both tests clearly demonstrate that a robust culture was achieved by the upflow fixed film reactors, which is a critical factor for FOB operations considering both temperature variation and feed instability.
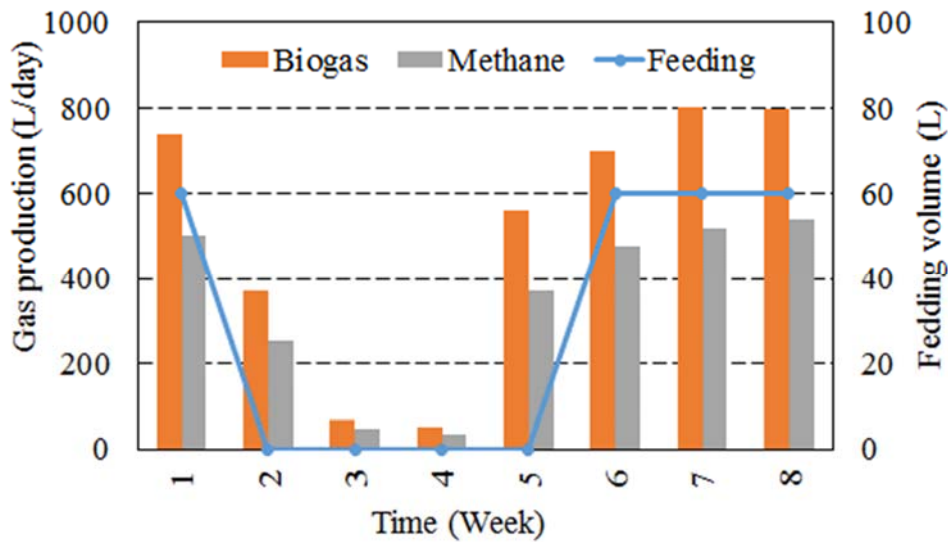

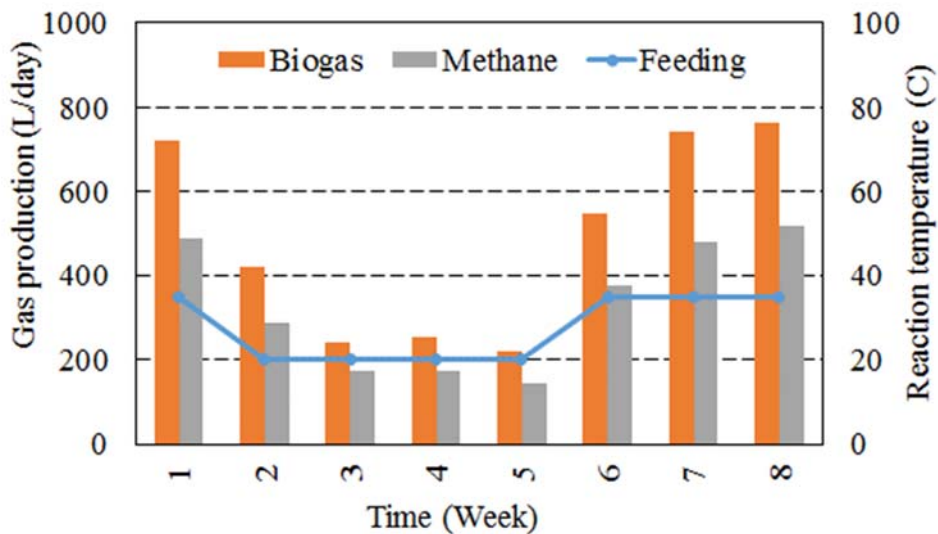Figure 53. The effect of feeding on digestion stability

Figure 54. The effect of temperature on digestion stability

4.5.2 Water reclamation

Even though the anaerobic digestion converts a significant portion of VS into biogas, the AD effluent from the digester still has very high nutrient contents. TS, COD, TN, and TP were 0.68%, 5,140 mg/L, 633 mg/L, and 340 mg/L, respectively (Table 31). Additional treatment is needed to generate potable water from the AD effluent. The EC and membrane filtration were combined to carry out the task. The bench-scale EC operation demonstrated that EC is effective on removing COD, TS, and TP. The pilot-scale EC used 20A DC to run the EC. The voltage stayed at ~10 V. The treatment time was 5 hours. After liquid/solid separation of the EC-treated effluent, TS, COD, TN and TP in the EC water (the supernatant) were reduced to 0.05%, 614 mg/L, 633 mg/L, and 0 mg/L, respectively. The pathogen indicators of total coliform, E.coli, Enterococci, and Coliphage were also significantly reduced (Table 31). With the removal of the nutrient and pathogens, the water was reclaimed. The NTU of the EC water is 60. However, the water quality still did not satisfy the standards of the potable water.

The three-unit membrane unit (one ultra-filtration, one nano-filtration, and one RO) was then used to treat the EC water and generate the potable water (the filtration unit was set up at the lab once the data was generated in this section). NTU, COD, TP, and TN were further reduced to 1, 3 mg/L, 0 mg/L, and 1.5 mg/L (Table 31). The removal of the pathogen indicators all exceeded 99.9999% (Table 31). The potable water has been achieved. However, the filtration unit was small (low pressure and slow flow). The water recovery was 50%, which is much lower than large, commercial scale filtration unit.

Parameters	AD effluent	EC-treated water	Potable water after filtration
Total solid (w/w %)	0.68	0.05	-
NTU	-	60	1
COD (mg/L)	5140	614	3
Total phosphorous (TP) (mg/L)	340	0	0
Total nitrogen (TN) (mg/L)	633	300	1.5
Reduction of total coliform (%)	-	99.8	> 99.9999
Reduction of E. coli (%)	-	99.6	> 99.9999
Reduction of Enterococci (%)	-	86.5	> 99.9999
Reduction of Coliphage (%)	-	67.9	> 99.9999

Table 31. Water quality data from integrated treatment facility.

4.5.3 Energy generation and consumption

The temperature profile of the digesters and heat storage demonstrates that the heat generated from solar and biogas energy can maintain the required digestion temperature (Figure 55). The hot water was maintained at 45±5°C, and the temperature of two reactors were maintained at 35±1°C. The solar and biogas thermal energy kept the temperature of the 160 L hot water storage tank in the range of 40 to 45°C, which holds enough thermal energy to maintain the digester at a temperature of 35°C. The temperature profile clearly indicates that the size of the solar and biogas production is sufficient to satisfy the thermal energy demand of two 300 L upflow fixed-film anaerobic digesters.
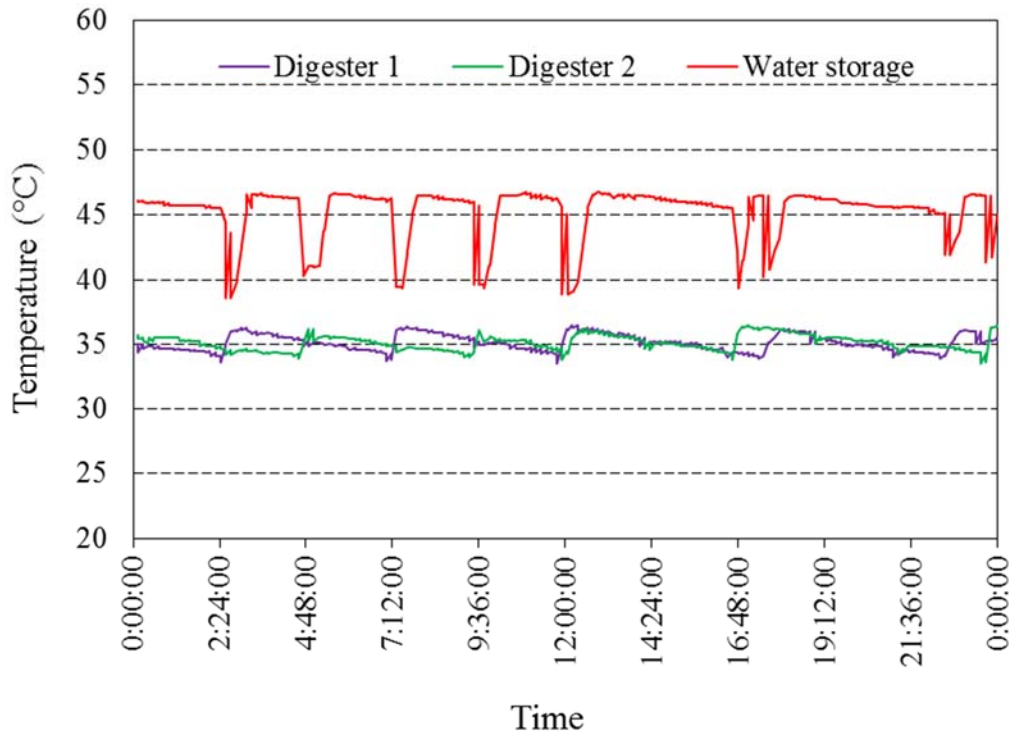
Figure 55. Temperature profile of the digesters and hot water storage tank of the pilot operation (the data were from February 24, 2017)

The overall energy consumption of the entire system is demonstrated in Figure 56. In a cold February, half of the month were raining, snowing, and cloudy days. The environmental temperature were changed dramatically between -10 to 15°C. The monthly energy demand of the pilot operation was 438 kWh. While, solar and bio energy generated 327 and 151 kWh/month, respectively. Neither of them alone was enough to cover the energy demand. Considering the advantages and disadvantages of solar and biogas energy (solar is instable but high generation, biogas is stable but less production), the pilot operation has proved that combining solar and biogas energy is a good solution to address this issue. The total energy generation from the combined solar and biogas unit operation was 479 kWh/month, which was more than the operation demand of 438 kWh. In addition, the unit also generated 41 kWh extra energy that could be used for other on-site applications.
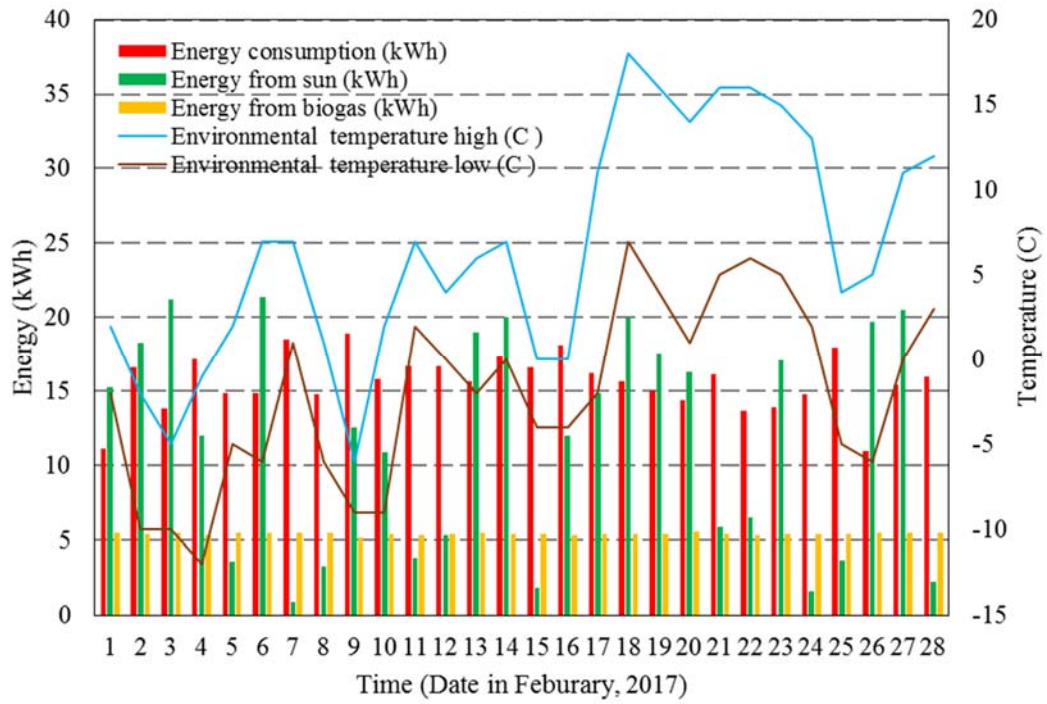
Figure 56. The energy profile of the pilot unit

## 4.6 Conducting a detailed technical and economic analysis on the system
4.6.1 Technical analysis

The mass and energy balance analysis was conducted on a 150 personnel expeditionary contingency base using the experimental data obtained from the pilot unit for two cases of 1) PV-AD-EC-aeration for non-potable water generation and 2) PV-AD-EC-filtration for potable water generation (Figure 57 and Table 32). The food wastes was mixed with black water. The amount of the mixed wastes is 3,160 kg per day (including 160 kg food wastes with 70% moisture content and 3,000 L black water). The TS and VS of the mixed feedstock are 1.5% and 1.27%, respectively. The system components of the PV-AD-EC-filtration case are described in Table 7. The system components of the PV-AD-EC-aeration case are similar with the case of the PV-AD-EC-Filtration one except the filtration unit was replaced by a simple aerobic treatment unit. A 12-hour aeration can remove majority of COD and TN in the EC solution and achieve a water with 62 mg/L COD, 30 mg/L TN, and 10 NTU. The treated water can be used for laundry and other non-portable uses. The energy consumption for 12-hour aeration was 1.73 kWh-e/m^3 solution [113].

With a HRT of 10 days, the AD reduces 76% and 71% of VS and TS, respectively. It generates 19,673 L/day methane from the mixed wastes. Biogas is stored in a biogas bag for electricity and heat generation. The AD effluent from the upflow fixed-film digesters is sent to the EC unit to remove the residual TS, and reclaim the water. 3,097 L/day reclaimed water is obtained from the EC operation. The EC unit also generates 2.5 kg sludge with 5% TS. After the EC treatment, the combination of PV-AD-EC-aeration uses the aeration to turn 3,097 L EC solution into 2,787 L non-potable water (Figure 57a). The combination of PV-AD-EC-filtration applies the ultra/nano/RO-filtration to produce 1,548 L potable water. Due to the fact that the filtration unit is a low pressure unit, the rejected water is high at 1,548 L.

(a)
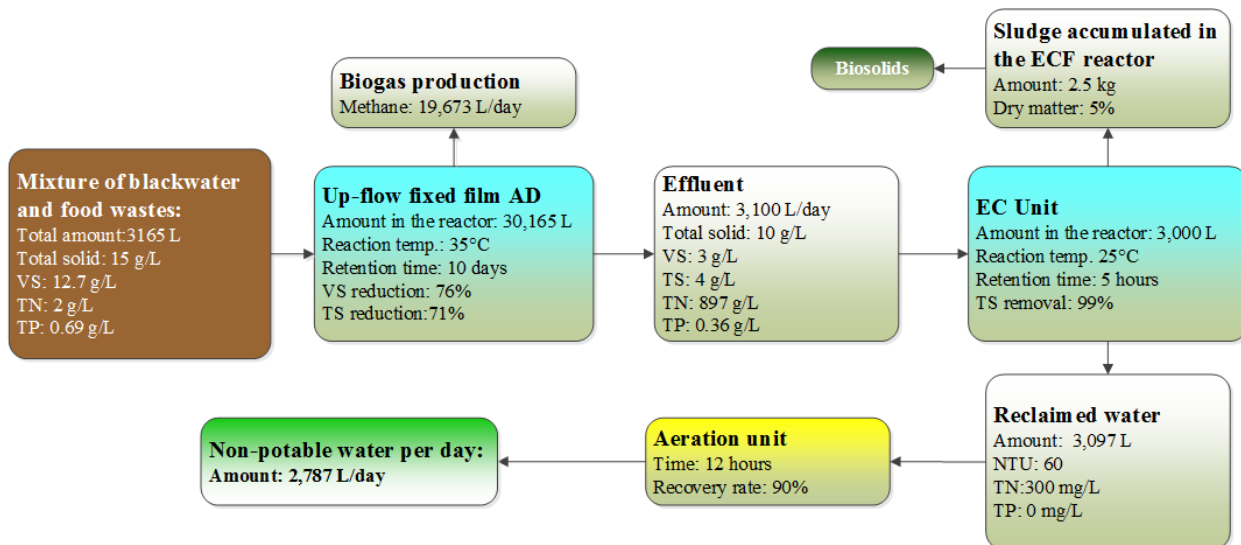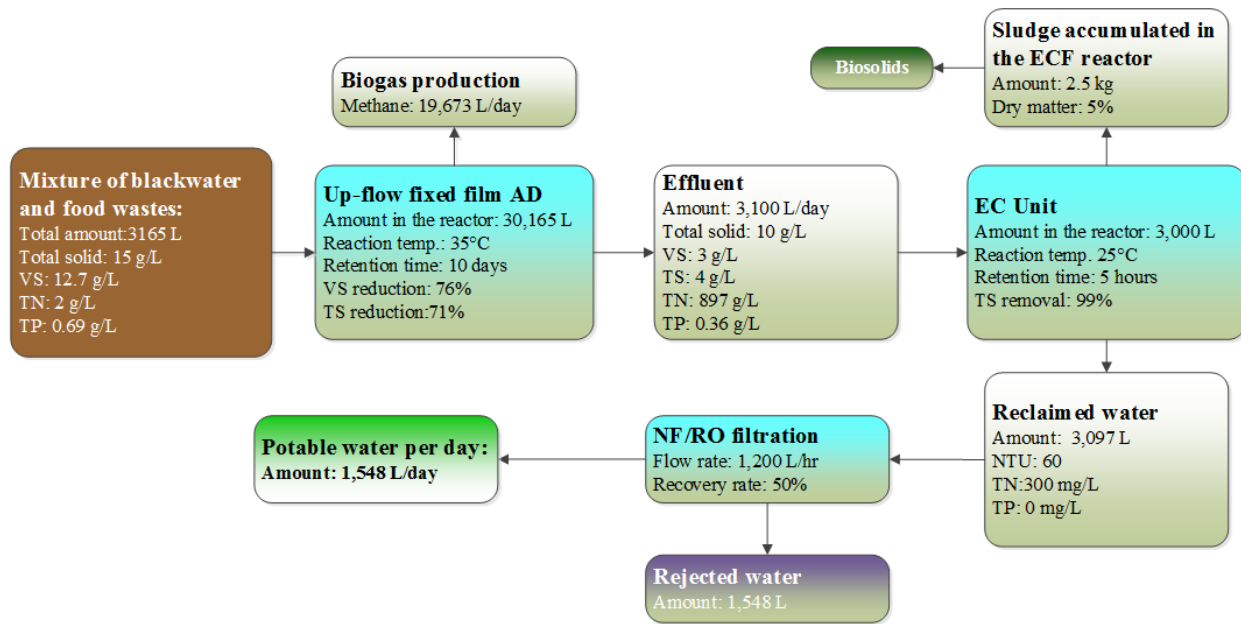
Figure 57. Predicted mass balance of the systems for a 150 personnel expeditionary contingency base *

a. The self-sustaining system with the aerobic treatment unit; b. The self-sustaining system with the filtration unit

*: The data for AD, EC, and filtration were based on the experimental results from the pilot unit. The aeration data were based on the reference.

The energy balance analysis further compared net energy outputs of these two combinations for the 150 personnel expeditionary contingency base (Table 32). 23 m² PV panels generate 12 kWh-e/day electricity (in a winter months at East Lansing, MI). The upflow fixed-film digester generates 52 and 104 kWh-e/day of electricity and heat, respectively. The heat requirement to heat the feed and maintain the digester temperature is 91 kWh-e/day. The electricity demands for AD, EC, and other uses are 10, 17, and 10 kWh-e/day, respectively. The filtration unit requires 22 kWh-e/day electricity to operate it. The aeration unit needs 5.2 kWh-e/day to power the aeration pump. In order to maintain a routine operation in cold and cloudy winter of northern climate, 59 and 91 kWh-e/day of electricity and heat are needed, respectively, by the PV-AD-EC-Filtration combination. The same heat (91 kWh-e/day) but much less electricity (32 kWh-e/day) are required by the PV-AD-EC-Aeration combination due to the fact that aeration demands much less electricity than membrane filtration unit (particularly RO unit). The net electricity and heat balances of both combinations are positive. However, without solar energy, the electricity balance of the PV-AD-EC-Filtration would be negative, which means that the system with solar panel cannot be self-sustained. With the implementation of PV panel, the PV-AD-EC-Aeration system has a much higher net electricity output (22 kWh-e/day) than the PV-Ad-EC-Filtration system (5 kWh-e/day), though, the potable water cannot be achieved by the PV-AD-EC-Aeration system. The energy balance clearly demonstrates an advantage of the integrated systems to self-sustainably treat the food wastes and black water for forward operating bases.

104

Table 32. Energy balance [a]

Unit operations		PV-AD-EC-Filtration		PV-AD-EC-aeration	
		Electricity (kWh-e/day)	Heat (kWh-e/day)	Electricity (kWh-e/day)	Heat (kWh-e/day)
Energy generation	Solar energy (kwh-e/day)	12	-	12	-
	Biogas energy (kwh-e/day)	52	104	52	104
Energy consumption	AD operation(kwh-e/day) [b]	-10	-91	-10	-91
	EC operation	-17	-	-17	-
	Membrane filtration	-22	-	-	-
	Aeration	-	-	-5	-
	Other electricity uses [c]	-10	-	-10	-
Net energy output		5	13	22	13

a: The positive numbers are energy generated. The negative numbers are energy consumed.
b: Electricity demand of the AD operation is for feedstock grinding, liquid transfer, and pump mixing. Heat demand of the AD operation is for maintaining the digester temperature.
c: Other uses include control panel, ventilation, control units, and computers.

4.6.2 Economic analysis

Economic feasibility is another critical factor that determines commercial applicability of a technology. Therefore, an economic assessment was carried out to examine CapEx, OpEx, and revenue of the solar-bio-nano-based wastewater treatment system. As it is presented in Table 33, the CapEx of PV-AD-EC-Filtration and PV-AD-EC-Aeration systems are $265,000 and $262,000, respectively. Among the units on the CapEx list, PLC and system installation are the most expensive ones ($70,000 and $50,000, respectively) due to the requirement of a compete automation. The OpEx of the systems are mainly for maintenance. The maintenance cost ($15,000) for the PV-AD-EC-Filtration includes oil changes of pumps, filters for engines, and membrane cleaning and replacements. The PV-AD-EC-Aeration system has less maintenance cost ($7,500) since it does not need high-pressure pumps and expensive membrane replacement. For both systems, the labor cost is not needed since the system is a fully automatic unit. Occasional check-up may be required, though, it is not a routine job. An alarm system is installed, so that messages will be sent to the responsible person if any event requires immediate attention.

As for the revenue, since the PV-AD-EC-Filtration system generates potable water, the revenue of the system considered the offsets from fully burdened cost of fuel and water. Under the simulated operation scale of 3,160 L feed with 1.5% TS per day, the system can generate $22,195 revenue per year from the energy and water savings. A net positive revenue of $7,195 per year is realized after considering the annual maintenance cost. The PV-AD-EC-Aeration system produces non-potable water. The half burdened cost of water is used to calculate the revenue from non-potable water. Under the same operation sale with the PV-AD-EC-Filtration, the system generates $16,950 revenue per year. A positive net revenue of 9,450 is also achieved, which is higher than the PV-AD-EC-Filtration system. The cash flow analysis further indicated that under the current operational conditions, the payback periods of the PV-AD-EC-Filtration and PV-AD-EC-Aeration systems for 150 personnel base are 30 and 24 years (Figure 58).

Table 33. Economic analysis

	The system with filtration unit	The system with aeration unit
Capital expenditure (CapEx)		
23 m^2 PV panel and battery	$25,000	$25,000
40 ft container	$25,000	$25,000
Feeding unit (grinder and housing)	$5,000	$5,000
15 m^3 Upflow fixed film digester (supportive platform, vessel, insulation, and Pall rings)	$25,000	$25,000
Biogas utilization unit (gas bag and engines)	$30,000	$30,000
3 m^3 EC unit	$10,000	$10,000
2 kW centrifuge	$20,000	$20,000
Filtration unit with water storage tank	$5,000	-
0.5 kW aeration fan with aeration vessel	-	$2,000
PLC with automatic valves, sensors, and flow meters	$70,000	$70,000
System installation [a]	$50,000	$50,000
Total CapEx cost	**$265,000**	**$262,000**
Revenue		
Energy saving [b]	$18,232	$14,974
Water saving [c]	$3,963	$1,976
Operational expenditure (OpEx)		
Maintenance	$15,000/year	$7,500
Labor cost [d]	$0/year	$0
Net Revenue		
Net revenue (only considering the revenue from the energy and water saving)	**$7,195 per year**	**$9,450 per year**

a. The cost of system installation is not included in the depreciation calculation.
b. The energy saving is based on the fully burdened cost of fuel ($0.333/kWh-e) to be delivered to the bases. The unit is changed to energy content (from gallon diesel fuel to kWh). It is based on $11.70/gallon diesel [2]. The energy consumption of the treatment is 163 kWh-e/day.
c. The potable water saving is based on the fully burdened cost ($2.64/L) of water to be delivered to the bases [2]. The non-potable water saving is based on the half burdened cost ($1,34/L) of water to be delivered to the bases.
d. It is fully automatic, and requires minimum routine operation.
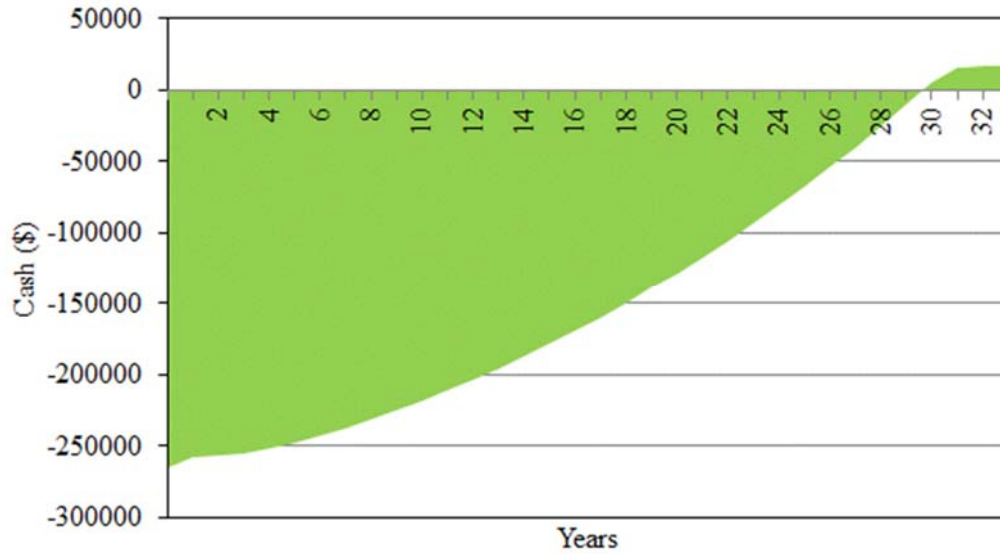
(a)
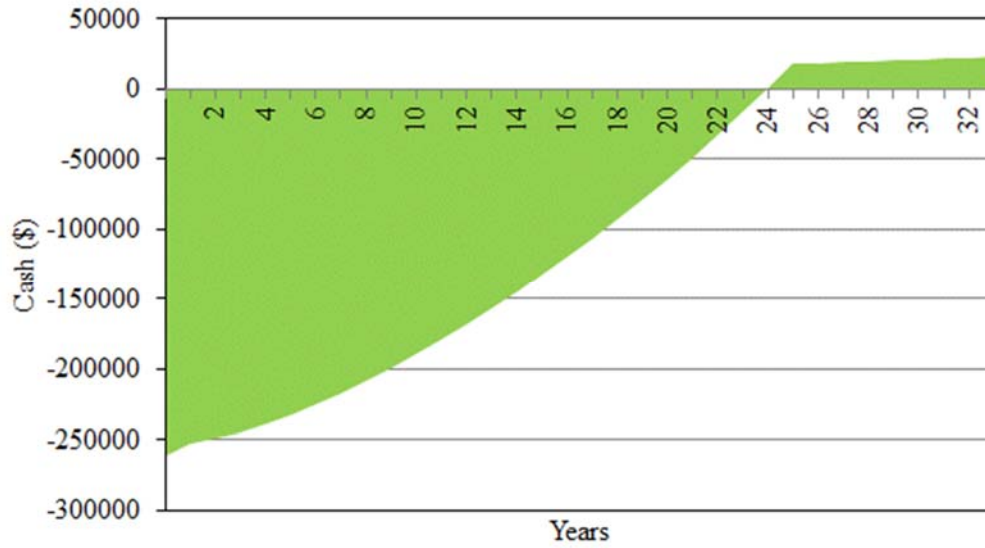
(b)

Figure 58. The cash flows of the integrated systems for a 150 personnel base
(a). The PV-AD-EC-Filtration system; (b) The PV-AD-EC-Aeration system

5. CONCLUSIONS AND IMPLICATIONS FOR FUTURE RESEARCH

5.1. Conclusions

The project conducted a comprehensive research on solar-bio-nano-based wastewater treatment system. The special efforts were given on solar-bio-hybrid energy generation and system integration. A self-sustaining solar-bio-nano-based wastewater concept has been achieved by this project. A pilot-scale unit integrating all components have been successfully demonstrated using the food wastes and black water. The results include that the self-sustaining system is scalable and robust under different feeding and operational conditions. The main conclusions from this research are listed as follow.

- A high-efficient, robust digestion to treat food wastes and black water has been concluded. Including both biofilm and concentrated anaerobic sludge in the digester significantly enhanced the digestion performance.
- A novel EC concept combined with biogas clean-up has been accomplished to improve biogas quality (reducing the burden on biogas engine) and enhance the efficiency of EC treatment.
- The solar-bio-hybrid energy solutions (PV/biogas and concentrated-solar-power/biogas) have been comprehensively studied. PV-bio-hybrid unit has been selected to be implemented at the pilot scale due to its simplicity and synergy with biogas regarding the demands on heat and electricity from the system.
- New solar thermal receivers using Fresnel lens have been developed and studied. It is a good solution to significantly reduce the weight and size of the currently available concentrated solar thermal technologies. It provides a possible route to be used in a small-scale CSP-bio-hybrid system. However, Efficiency and robustness of currently available small-scale steam and gas engines limit such applications.
- The detailed technical and economic analysis on two system configurations of PV-AD-EC-Filtration and PV-AD-EC-Aeration concluded that the PV-AD-EC-Filtration configuration can convert blackwater and food wastes into potable water with higher energy consumption and longer payback period, and the PV-AD-EC-Aeration has better performance on energy consumption and payback period, but generate low-quality non-potable water. Dependent on different applications, FOBs can choose different configurations to treat their wastewater and food wastes.

5.2. Potential applications for military operations

Besides system integration of blackwater and food waste treatment, the project studied three individual unit operations. Different combinations of these unit operations could satisfy the different needs of FOBs. For instances, if a FOB just needs energy generation to replace some diesel consumption, a system with PV and AD using blackwater and food wastes as the source could be implemented. If a FOB wants both renewable energy and potable water, they have to go with the configuration with PV, AD, EC, and filtration. Other case scenarios are listed in Table 34.

Table 34. Different system configurations for potential FOB applications [a]

Wastewater source	Application	Configuration				
		PV	AD	EC	Aeration	Filtration
	Energy generation only	X	X			
	Non-potable water production only		X	X	X	

Blackwater & food wastes	Potable water production only		X	X		X
	Energy & non-potable water production	X	X	X	X	
	Energy & potable water production	X	X	X		X
Graywater	Non-potable water production only			X	X	
	Potable water production only			X		X

a. "X" means the selected unit operation.

5.3. Future research and development

Built upon the foundation from this project, future research and development should be focused on the following topics.

- Small-scale steam engines (less than 30 kW) needs to be developed to accommodate the need of small-scale concentrated solar thermal power generation as well as small-scale biogas power generation.
- System optimization studies are needed to further refine the integrated process and improve system efficiency.
- Detailed microbial study on the microbial communities in fixed film, solution, and sludge need to be delineated, so that the digestion can be further optimized to have better solid/liquid separation performance.
- A deployable unit should be developed to study the effects of real operation and climate conditions on the system.

6. LITERATURE CITED

[1] R.J. Scholze, G.L. Gerdes, W.D. Goran, J. Hall, K. Preston, M. McLeod, D. Sheets, R. Sustich, Proceedings of the Military Applications for Emerging Water Use Technologies Workshop, Center for the Advancement of Sustainability Innovations (CASI), US Army Corps of Engineers, 2009.

[2] Noblis, Strategic Environmental Research and Development Program (SERDP) -- Sustainable Forward Oprating Bases, DOD SERDP, 2010.

[3] H. Harada, S. Uemura, A.C. Chen, J. Jayadevan, Anaerobic treatment of a recalcitrant distillery wastewater by a thermophilic UASB reactor, Bioresource Technology 55(3) (1996) 215-221.

[4] G. Lettinga, R. Roersma, P. Grin, ANAEROBIC TREATMENT OF RAW DOMESTIC SEWAGE AT AMBIENT-TEMPERATURES USING A GRANULAR BED UASB REACTOR, Biotechnology and Bioengineering 25(7) (1983) 1701-1723.

[5] B.K. Ahring, M. Sandberg, I. Angelidaki, VOLATILE FATTY-ACIDS AS INDICATORS OF PROCESS IMBALANCE IS ANAEROBIC DIGESTERS, Applied Microbiology and Biotechnology 43(3) (1995) 559-565.

[6] D. Mills, Advances in solar thermal electricity technology, Solar Energy 76(1-3) (2004) 19-31.

[7] H.M. El-Mashad, W.K.P. van Loon, G. Zeeman, G.P.A. Bot, G. Lettinga, Design of a solar thermophilic anaerobic reactor for small farms, Biosystems Engineering 87(3) (2004) 345-353.

[8] A.C. Yiannopoulos, I.D. Manariotis, C.V. Chrysikopoulos, Design and analysis of a solar reactor for anaerobic wastewater treatment, Bioresource Technology 99(16) (2008) 7742-7749.

[9] G. Kocar, A. Eryasar, An application of solar energy storage in the gas: Solar heated biogas plants, Energy Sources Part a-Recovery Utilization and Environmental Effects 29(16) (2007) 1513-1520.

[10] R.E. Aguilar Alvarez, M. Bustamante Roman, D. Kirk, J.A. Miranda Chavarria, D. Baudrit, J.F. Aguilar Pereira, W. Rodriguez Montero, D. Reinhold, W. Liao, Technical and economic feasibility of a solar-bio-powered waste utilization and treatment system in Central America, Journal of environmental management 184(Pt 2) (2016) 371-379.

[11] Y. Zhong, M.B. Roman, Y.K. Zhong, S. Archer, R. Chen, L. Deitz, D. Hochhalter, K. Balaze, M. Sperry, E. Werner, D. Kirk, W. Liao, Using anaerobic digestion of organic wastes to biochemically store solar thermal energy, Energy 83 (2015) 638-646.

[12] R.B. Dean, PROCESSES FOR WATER RECLAMATION, Waste Management & Research 9(5) (1991) 425-430.

[13] V.K. Tyagi, A.A. Khan, A.A. Kazmi, A.K. Chopra, Enhancement of Coagulation Flocculation Process Using Anionic Polymer for the Post Treatment of UASB Reactor Effluent, Separation Science and Technology 45(5) (2010) 626-634.

[14] M.Y.A. Mollah, R. Schennach, J.R. Parga, D.L. Cocke, Electrocoagulation (EC) - science and applications, Journal of Hazardous Materials 84(1) (2001) 29-41.

[15] G.H. Chen, Electrochemical technologies in wastewater treatment, Separation and Purification Technology 38(1) (2004) 11-41.

[16] E. Butler, Y.-T. Hung, R.Y.-L. Yeh, M.S. Al Ahmad, Electrocoagulation in Wastewater Treatment, Water 3 (2011) 495-525.

[17] S. Bellebia, S. Kacha, A.Z. Bouyakoub, Z. Derriche, Experimental investigation of chemical oxygen demand and turbidity removal from cardboard paper mill effluents using combined

electrocoagulation and adsorption processes, Environmental Progress & Sustainable Energy 31(3) (2012) 361-370.

[18] M.Y.A. Mollah, P. Morkovsky, J.A.G. Gomes, M. Kesmez, J. Parga, D.L. Cocke, Fundamentals, present and future perspectives of electrocoagulation, Journal of Hazardous Materials 114(1-3) (2004) 199-210.

[19] D.L.C. Hector A. Moreno-Casillas, Jewel A.G. Gomes,, J.R.P. Paul Morkovsky, Eric Peterson, Electrocoagulation mechanism for COD removal, Separation and Purification Technology 56(2) (2007) 7.

[20] M.Y. Mollah, P. Morkovsky, J.A. Gomes, M. Kesmez, J. Parga, D.L. Cocke, Fundamentals, present and future perspectives of electrocoagulation, Journal of hazardous materials 114(1-3) (2004) 199-210.

[21] M.-F.P. Nazih K. Shammas, and Alain Grasmick, Wastewater Treatment by Electrocoagulation–Flotation, Flotation Technology 12 (2010) 21.

[22] I.A. Sengil, M. Ozacar, Treatment of dairy wastewaters by electrocoagulation using mild steel electrodes, Journal of hazardous materials 137(2) (2006) 1197-205.

[23] M. Kobya, E. Senturk, M. Bayramoglu, Treatment of poultry slaughterhouse wastewaters by electrocoagulation, Journal of hazardous materials 133(1-3) (2006) 172-6.

[24] S.B. Nicolas Abatzoglou, A review of biogas purifi cation processes, Biofuel Bioproducts & Biorefining 3(1) (2009) 29.

[25] G.J.a.A. M, Process and apparatus for removal of H2S from gaseous streams using membrane purifi cation of recycle solution, The Dow Chemical Company, USA, 1992.

[26] R.R. Broekhuis, D.J. Koch, S. Lynn, A medium-temperature process for removal of hydrogen sulfide from sour gas streams with aqueous metal sulfate solutions, Industrial & Engineering Chemistry Research 31(12) (1992) 2635-2642.

[27] A. Dabrowski, P. Podkoscielny, Z. Hubicki, M. Barczak, Adsorption of phenolic compounds by activated carbon--a critical review, Chemosphere 58(8) (2005) 1049-70.

[28] F. Adib, A. Bagreev, T.J. Bandosz, Analysis of the Relationship between H2S Removal Capacity and Surface Properties of Unimpregnated Activated Carbons, Environmental Science & Technology 34(4) (2000) 686-692.

[29] A. Bagreev, T.J. Bandosz, A Role of Sodium Hydroxide in the Process of Hydrogen Sulfide Adsorption/Oxidation on Caustic-Impregnated Activated Carbons, Industrial & Engineering Chemistry Research 41(4) (2002) 672-679.

[30] M. Schweigkofler, R. Niessner, Removal of siloxanes in biogases, Journal of hazardous materials 83(3) (2001) 183-96.

[31] Y. Jin, M.C. Veiga, C. Kennes, Effects of pH, CO2, and flow pattern on the autotrophic degradation of hydrogen sulfide in a biotrickling filter, Biotechnol Bioeng 92(4) (2005) 462-71.

[32] J.L. Conde, L.E. Moro, L. Travieso, E.P. Sanchez, A. Leiva, R. Dupeirón, R. Escobedo, Biogas purification process using intensive microalgae cultures, Biotechnology Letters 15(3) (1993) 317-320.

[33] G.S. M. Syed, P. Falletta and M. Béland, Removal of hydrogen sulfide from gas streams using biological processes - a review, Canadian Biosystems Engineering 48 (2006) 14.

[34] J. Theron, J.A. Walker, T.E. Cloete, Nanotechnology and water treatment: Applications and emerging opportunities, Critical Reviews in Microbiology 34(1) (2008) 43-69.

[35] N. Savage, M.S. Diallo, Nanomaterials and water purification: Opportunities and challenges, Journal of Nanoparticle Research 7(4-5) (2005) 331-342.

[36] S.K. Brar, M. Verma, R.D. Tyagi, R.Y. Surampalli, Engineered nanoparticles in wastewater and wastewater sludge - Evidence and impacts, Waste Management 30(3) (2010) 504-520.

[37] T.H. Bae, T.M. Tak, Effect of TiO2 nanoparticles on fouling mitigation of ultrafiltration membranes for activated sludge filtration, Journal of Membrane Science 249(1-2) (2005) 1-8.

[38] T.H. Bae, I.C. Kim, T.M. Tak, Preparation and characterization of fouling-resistant TiO2 self-assembled nanocomposite membranes, Journal of Membrane Science 275(1-2) (2006) 1-5.

[39] L. Wu, M. Shamsuzzoha, S.M.C. Ritchie, Preparation of cellulose acetate supported zero-valent iron nanoparticles for the dechlorination of trichloroethylene in water, Journal of Nanoparticle Research 7(4-5) (2005) 469-476.

[40] L.F. Wu, S.M.C. Ritchie, Removal of trichloroethylene from water by cellulose acetate supported bimetallic Ni/Fe nanoparticles, Chemosphere 63(2) (2006) 285-292.

[41] J. Xu, D. Bhattacharyya, Fe/Pd nanoparticle immobilization in microfiltration membrane pores: Synthesis, characterization, and application in the dechlorination of polychlorinated biphenyls, Industrial & Engineering Chemistry Research 46(8) (2007) 2348-2359.

[42] D.G. Yu, M.Y. Teng, W.L. Chou, M.C. Yang, Characterization and inhibitory effect of antibacterial PAN-based hollow fiber loaded with silver nitrate, Journal of Membrane Science 225(1-2) (2003) 115-123.

[43] D.T. Schoen, A.P. Schoen, L.B. Hu, H.S. Kim, S.C. Heilshorn, Y. Cui, High Speed Water Sterilization Using One-Dimensional Nanostructures, Nano Letters 10(9) (2010) 3628-3632.

[44] J. Kim, B. Van der Bruggen, The use of nanoparticles in polymeric and ceramic membrane structures: Review of manufacturing procedures and performance improvement for water treatment, Environmental Pollution 158(7) (2010) 2335-2349.

[45] R. Molinari, M. Borgese, E. Drioli, L. Palmisano, M. Schiavello, Hybrid processes coupling photocatalysis and membranes for degradation of organic pollutants in water, Catalysis Today 75(1-4) (2002) 77-85.

[46] N. Her, G. Amy, A. Plottu-Pecheux, Y. Yoon, Identification of nanofiltration membrane foulants, Water Research 41(17) (2007) 3936-3947.

[47] B.S. Karnik, S.H.R. Davies, K.C. Chen, D.R. Jaglowski, M.J. Baumann, S.J. Masten, Effects of ozonation on the permeate flux of nanocrystalline ceramic membranes, Water Research 39(4) (2005) 728-734.

[48] S. Lee, R.M. Lueptow, Reverse osmosis filtration for space mission wastewater: membrane properties and operating conditions, Journal of Membrane Science 182(1-2) (2001) 77-90.

[49] Y. Yang, A. Gutsol, A. Fridman, Y.I. Cho, Removal of CaCO3 scales on a filter membrane using plasma discharge in water, International Journal of Heat and Mass Transfer 52(21-22) (2009) 4901-4906.

[50] T.H. Dang, A. Denat, O. Lesaint, G. Teissedre, Pulsed electrical discharges in water for removal of organic pollutants: a comparative study, European Physical Journal-Applied Physics 47(2) (2009).

[51] S. Lee, R.M. Lueptow, Rotating membrane filtration and rotating reverse osmosis, Journal of Chemical Engineering of Japan 37(4) (2004) 471-482.

[52] S. Lee, R.M. Lueptow, Rotating reverse osmosis for water recovery in space: influence of operational parameters on RO performance, Desalination 169(2) (2004) 109-120.

[53] I. Reda, A. Andreas, Solar Position Algorithm for Solar Radiation Applications, National Renewable Energy Laboratory, Golden, Colorado, 2008.

[54] L.M. Jiji, ebrary Inc., Heat conduction, Springer-Verlag,, Berlin ; Heidelberg, 2009, pp. xv, 418 p.

[55] M.F. Modest, Radiative heat transfer, Academic Press,, New York, 2013, pp. xxii, 882 pages.

[56] R. Chen, M.M. Roos, Y. Zhong, T. Marsh, M.B. Roman, W. Hernandez Ascencio, L. Uribe, L. Uribe Lorio, D. Kirk, D.M. Reinhold, J.A. Miranda Chavarria, D. Baudrit Ruiz, J.F.A. Pereira, W.R. Montero, A. Srivastava, W. Liao, Responses of anaerobic microorganisms to different culture conditions and corresponding effects on biogas production and solid digestate quality, Biomass and Bioenergy 85 (2016) 84-93.

[57] Q. Sun, H. Li, J. Yan, L. Liu, Z. Yu, X. Yu, Selection of appropriate biogas upgrading technology-a review of biogas cleaning, upgrading and utilisation, Renewable and Sustainable Energy Reviews 51 (2015) 521-532.

[58] Halotechnics, High temperature thermal fluids, 2013. http://www.halotechnics.com/products/. (Accessed 10/30/2015 2015).

[59] NextGrid, NextGrid CHP Models, 2014. http://www.gonextgrid.com/products/nextgrid-chp-models/. 2015).

[60] A. Liu, Y. Weng, Effects of Lower Heat Value Fuel on the Operations of Micro-Gas Turbine, Energy and Power Engineering 1(1) (2009) 28-37.

[61] NREL, Solar Prospector, http://maps.nrel.gov/prospector, 2015.

[62] U.S.ClimateData, Temperature-Precipitation-Sunchine-Snowfall, http://www.usclimatedata.com/, 2015.

[63] A.M.C. Jirka, M.J.,, Analytical Chemistry, 1975.

[64] E.P. Agency, TURBIDITY METHODS & MEASUREMENT, (1999).

[65] Z. Liu, D. Stromberg, X. Liu, W. Liao, Y. Liu, A new multiple-stage electrocoagulation process on anaerobic digestion effluent to simultaneously reclaim water and clean up biogas, Journal of hazardous materials 285 (2015) 483-490.

[66] A.M. Jirka, M.J. Carter, Analytical Chemistry 47(8) (1975) 1397.

[67] A. Haeggkvist, J. Sjostrom, U. Wickstrom, Using plate thermometer measurements to calculate incident heat radiation, Journal of Fire Sciences 31(2) (2013) 166-177.

[68] Autodesk, Simulation CFD, 2015.

[69] Y.A. Çengel, Heat transfer: a practical approach, WBC McGraw-Hill, Boston, Mass, 1998.

[70] Z. Yue, J. MacLellan, Y. Liu, W. Liao, Effects of corn stover as carbon supplement on an integrated anaerobic digestion and ethanol fermentation process, Journal of Renewable and Sustainable Energy 5(6) (2013) 063116-063116-9.

[71] L. Lijó, S. González-García, J. Bacenetti, M. Fiala, G. Feijoo, J.M. Lema, M.T. Moreira, Life Cycle Assessment of electricity production in Italy from anaerobic co-digestion of pig slurry and energy crops, Renewable Energy 68 (2014) 625-635.

[72] E. Ryckebosch, M. Drouillon, H. Vervaeren, Techniques for transformation of biogas to biomethane, Biomass and Bioenergy 35(5) (2011) 1633-1645.

[73] V. Siva Reddy, S.C. Kaushik, K.R. Ranjan, S.K. Tyagi, State-of-the-art of solar thermal power plants—A review, Renewable and Sustainable Energy Reviews 27(0) (2013) 258-273.

[74] D. Popov, Innovative solar augmentation of gas turbine combined cycle plants, Applied Thermal Engineering 64(1–2) (2014) 40-50.

[75] M.S. Jamel, A. Abd Rahman, A.H. Shamsuddin, Advances in the integration of solar thermal energy with conventional and non-conventional power plants, RENEWABLE & SUSTAINABLE ENERGY REVIEWS 20 (2013) 71-81.

[76] A. Giostri, M. Binotti, P. Silva, E. Macchi, G. Manzolini, Comparison of Two Linear Collectors in Solar Thermal Plants: Parabolic Trough Versus Fresnel, Journal of Solar Energy Engineering 135(1) (2013) 011001-9.

[77] S. Skouri, S. Bouadila, M. Ben Salah, S. Ben Nasrallah, Comparative study of different means of concentrated solar flux measurement of solar parabolic dish, Energy Conversion and Management 76 (2013) 1043-1052.

[78] NREL, System Advisor Model, National Renewable Laboratory, 2016, p. SSC Version 159: Windows 64 bit

Visual C++ Mar 14 2016 12:24:39.

[79] S. Kakaç, H. Liu, Heat exchangers: selection, rating, and thermal design, CRC Press, Boca Raton, Fla, 1998.

[80] T. Mancini, P. Heller, B. Butler, B. Osborn, W. Schiel, V. Goldberg, R. Buck, R. Diver, C. Andraka, J. Moreno, Dish-Stirling systems: An overview of development and status, Journal of Solar Energy Engineering-Transactions of the Asme 125(2) (2003) 135-151.

[81] D.A. Baharoon, H.A. Rahman, W.Z.W. Omar, S.O. Fadhl, Historical development of concentrating solar power technologies to generate clean electricity efficiently - A review, Renewable & Sustainable Energy Reviews 41 (2015) 996-1027.

[82] K. Yetilmezsoy, F. Ilhan, Z. Sapci-Zengin, S. Sakar, M.T. Gonullu, Decolorization and COD reduction of UASB pretreated poultry manure wastewater by electrocoagulation process: a post-treatment study, Journal of hazardous materials 162(1) (2009) 120-32.

[83] Q. Zuo, X. Chen, W. Li, G. Chen, Combined electrocoagulation and electroflotation for removal of fluoride from drinking water, Journal of hazardous materials 159(2-3) (2008) 452-7.

[84] N. Adhoum, L. Monser, N. Bellakhal, J.E. Belgaied, Treatment of electroplating wastewater containing Cu2+, Zn2+ and Cr(VI) by electrocoagulation, Journal of hazardous materials 112(3) (2004) 207-13.

[85] P.K. Holt, G.W. Barton, M. Wark, C.A. Mitchell, A quantitative comparison between chemical dosing and electrocoagulation, Colloids and Surfaces A: Physicochemical and Engineering Aspects 211(2–3) (2002) 233-248.

[86] Y. Avsar, U. Kurt, T. Gonullu, Comparison of classical chemical and electrochemical processes for treating rose processing wastewater, Journal of hazardous materials 148(1-2) (2007) 340-5.

[87] N. Adhoum, L. Monser, Decolourization and removal of phenolic compounds from olive mill wastewater by electrocoagulation, Chemical Engineering and Processing: Process Intensification 43(10) (2004) 1281-1287.

[88] X. Lei, T. Maekawa, Electrochemical treatment of anaerobic digestion effluent using a Ti/Pt-IrO2 electrode, Bioresource technology 98(18) (2007) 3521-5.

[89] K. Yetilmezsoy, F. Ilhan, Z. Sapci-Zengin, S. Sakar, M.T. Gonullu, Decolorization and COD reduction of UASB pretreated poultry manure wastewater by electrocoagulation process: A post-treatment study, Journal of Hazardous Materials 162(1) (2009) 120-132.

[90] Y. Avsar, U. Kurt, T. Gonullu, Comparison of classical chemical and electrochemical processes for treating rose processing wastewater, Journal of Hazardous Materials 148(1-2) (2007) 340-345.

[91] D.W. Shoesmith, P. Taylor, M.G. Bailey, D.G. Owen, THE FORMATION OF FERROUS MONOSULFIDE POLYMORPHS DURING THE CORROSION OF IRON BY AQUEOUS HYDROGEN-SULFIDE AT 21-DEGREES-C, Journal of the Electrochemical Society 127(5) (1980) 1007-1015.

[92] G. Capar, L. Yilmaz, U. Yetis, Reclamation of acid dye bath wastewater: effect of pH on nanofiltration performance, Journal of membrane science 281(1) (2006) 560-569.

[93] S. Hong, M. Elimelech, Chemical and physical aspects of natural organic matter (NOM) fouling of nanofiltration membranes, Journal of membrane science 132(2) (1997) 159-181.

[94] C.Y. Tang, Y.-N. Kwon, J.O. Leckie, Fouling of reverse osmosis and nanofiltration membranes by humic acids-Effects of solution composition and hydrodynamic conditions, Journal of membrane science 290(1) (2007) 86-94.

[95] W. Yuan, A.L. Zydney, Effects of solution environment on humic acid fouling during microfiltration, Desalination 122(1) (1999) 63-76.

[96] W. Yuan, A.L. Zydney, Humic acid fouling during microfiltration, Journal of membrane science 157(1) (1999) 1-12.

[97] L. Shao, T. Wang, T. Li, F. Lu, P. He, Comparison of sludge digestion under aerobic and anaerobic conditions with a focus on the degradation of proteins at mesophilic temperature, Bioresource technology 140 (2013) 131-137.

[98] B.W. Stanton, J.J. Harris, M.D. Miller, M.L. Bruening, Ultrathin, multilayered polyelectrolyte films as nanofiltration membranes, Langmuir 19(17) (2003) 7038-7042.

[99] S.S. Shiratori, M.F. Rubner, pH-dependent thickness behavior of sequentially adsorbed layers of weak polyelectrolytes, Macromolecules 33(11) (2000) 4213-4219.

[100] J. Park, J. Park, S.H. Kim, J. Cho, J. Bang, Desalination membranes from pH-controlled and thermally-crosslinked layer-by-layer assembled multilayers, Journal of Materials Chemistry 20(11) (2010) 2085-2091.

[101] P. Schuetz, F. Caruso, Copper-Assisted Weak Polyelectrolyte Multilayer Formation on Microspheres and Subsequent Film Crosslinking, Advanced Functional Materials 13(12) (2003) 929-937.

[102] W. Shan, P. Bacchin, P. Aimar, M.L. Bruening, V.V. Tarabara, Polyelectrolyte multilayer films as backflushable nanofiltration membranes with tunable hydrophilicity and surface charge, Journal of membrane science 349(1) (2010) 268-278.

[103] B.P. Tripathi, N.C. Dubey, M. Stamm, Functional polyelectrolyte multilayer membranes for water purification applications, Journal of hazardous materials 252–253(0) (2013) 401-412.

[104] T. Carroll, N.A. Booker, J. Meier-Haack, Polyelectrolyte-grafted microfiltration membranes to control fouling by natural organic matter in drinking water, Journal of membrane science 203(1–2) (2002) 3-13.

[105] F. Diagne, R. Malaisamy, V. Boddie, R.D. Holbrook, B. Eribo, K.L. Jones, Polyelectrolyte and Silver Nanoparticle Modification of Microfiltration Membranes To Mitigate Organic and Bacterial Fouling, Environmental Science & Technology 46(7) (2012) 4025-4033.

[106] H. Yamamura, K. Okimoto, K. Kimura, Y. Watanabe, Hydrophilic fraction of natural organic matter causing irreversible fouling of microfiltration and ultrafiltration membranes, Water Research 54(0) (2014) 123-136.

[107] A. Matin, Z. Khan, K.K. Gleason, M. Khaled, S.M.J. Zaidi, A. Khalil, P. Moni, R. Yang, Surface-modified reverse osmosis membranes applying a copolymer film to reduce adhesion of bacteria as a strategy for biofouling control, Separation and Purification Technology 124 (2014) 117-123.

[108] J.B. Schlenoff, Charge Balance and Transport in Ion-Paired Polyelectrolyte Multilayers, Multilayer Thin Films, Wiley-VCH Verlag GmbH & Co. KGaA2012, pp. 281-320.

[109] L. Ouyang, R. Malaisamy, M.L. Bruening, Multilayer polyelectrolyte films as nanofiltration membranes for separating monovalent and divalent cations, Journal of membrane science 310(1) (2008) 76-84.

[110] J. Choi, M.F. Rubner, Influence of the degree of ionization on weak polyelectrolyte multilayer assembly, Macromolecules 38(1) (2005) 116-124.

[111] W. Tong, C. Gao, H. Mohwald, Stable weak polyelectrolyte microcapsules with pH-responsive permeability, Macromolecules 39(1) (2006) 335-340.

[112] P. Bieker, M. Schonhoff, Linear and exponential growth regimes of multilayers of weak polyelectrolytes in dependence on pH, Macromolecules 43(11) (2010) 5052-5059.

[113] M. Bustamante, W. Liao, A self-sustaining high-strength wastewater treatment system using solar-bio-hybrid power generation, Bioresource technology 234 (2017) 415-423.

APPENDICES

A. List of published peer-reviewed Journal Articles (5 more are under review)

- Bustamante-Roman, M., Liao, W. 2017. A self-sustaining high-strength wastewater treatment system using solar-bio-hybrid power generation. Bioresource Technology 234, 415-423
- Song, A.; Ji, S.; Hong, J.; Ji, Y.; Gokhale, A.A.; Lee, I. "Encapsulation of hydrophobic or hydrophilic iron oxide nanoparticles into poly-(lactic acid) micro/nanoparticles via adaptable emulsion setup," Journal of Applied Polymer Science 133, 43749-43758, (2016).
- Yu, J.; Han, S.; Hong, J.; Sanyal, O.; Lee, I. "Synchronous Generation of Nano- and Micro-scaled Hierachical Porous Polyelectrolyte Multilayers for Superwettable Surfaces," Langmuir 32, 8494-8500, (2016).
- Sanyal, O.; Liu, Z.; Yu, J.; Meharg, B.M.; Hong, J.; Liao, W.; Lee, I. "Designing fouling-resistant clay-embedded polyelectrolyte multilayer membranes for wastewater effluent treatment," Journal of Membrane Science 512, 21-28, (2016).
- Sanyal, O.; Liu, Z.; Meharg, B. M.; Liao, W.; Lee, I. "Development of polyelectrolyte multilayer membranes to reduce the COD level of electrocoagulation treated high-strength wastewater," Journal of Membrane Science 496, 259-266, (2015).
- Sanyal, O.; Sommerfeld, A.N.; Lee, I. "Design of ultrathin nanostructured polyelectrolyte-based membranes with high perchlorate rejection and high permeability," Separation and Purification Technology 145, 113-119, (2015).
- Gokhale, A.A.; Lu, J.; Parker, N.J.; Izbicki, A.P.; Sanyal, O.; Lee, I. "Conductive oxygen barrier films using supramolecular assembly of graphene embedded polyelectrolyte multilayers," Journal of Colloid and Interface Science 409, 219-226, (2013).
- Paul, C. J.; Engeda, A. Modeling a Complete Stirling Engine, Energy, 2015, Vol.80:85 97
- Paul, C. J.; Engeda, A. Stirling Engine for Use With Lower Quality Fuels, Energy, 2015, Vol.84:152-160
- Tan, X., Engeda, A. Performance of centrifugal pumps running in reverse as turbine, Renewable Energy, 2015, Vol. 99. 188-197
- Yu, J.; Sanyal, O.; Izbicki, A.P.; Lee, I. "Development of Layered Multi-scale Porous Thin Films by Tuning Deposition Time and Molecular Weight of Polyelectrolytes," Macromolecular Rapid Communications 36, 1669-1674, (2015).
- Zhong, Y., Bustamante-Roman, M., Zhong, Y., Archer, S., Chen, R., Deitz, L., Hochhalter, D., Balaze, K., Sperry M., Werner, E., Kirk, D., Liao, W. Using anaerobic digestion of organic wastes to biochemically store solar thermal energy. Journal of Energy 2015, 83, 638-646
- Gokhale, A. A.; Lee, I. "Recent advances in the fabrication of nanostructured barrier films," Journal of Nanoscience and Nanotechnology 14, 2157-2177, (2014).
- Sanyal, O.; Lee, I. "Recent Progress in the Applications of Layer-By-Layer Assembly to the Preparation of Nanostructured Ion-Rejecting Water Purification Membranes," Journal of Nanoscience and Nanotechnology 14, 2178-2189, (2014)

B. Presentations at National and International Conferences

- Liao, W., Aguilar-Alvarez, R. E., Bustamante-Roman, M., Kirk, D., Reinhold, D., Chen, R., Murillo-Roos, M., Zhong, Y., Uribe, L., Uribe-Lorio, L., Miranda-Chavarria, J. A., Baudrit-Ruiz, D., Aguilar-Pereira, J. F., Rodriguez-Montero, W.. 2016. A self-sustaining concept to

convert organic wastes into valuable products. Oral presentation at the 8th ENCUENTRO RedBioLAC. San Jose, Costa Rica. November 10.

- Bustamante, M., Liao, W. 2016. Small-scale solar-bio-hybrid power generation using Brayton and Rankine cycles. Oral presentation at the 2016 ASABE Annual International Meeting, Orlando, FL. July 17-20.
- Liu, Z., Vanderberg, M., Sanyal, O., Lee, I., Liao, W., Liu, Y. 2016. A novel approach to simultaneously clean up biogas and reclaim water from anaerobic digestion. Oral presentation at the 2016 ASABE Annual International Meeting, Orlando, FL. July 17-20.
- Liao, W., Dana, K., Reinhold, D. 2016. Technical and economic analysis of integrated anaerobic digestion system for value-added utilization of organic wastes. Oral presentation at the 26th Annual Solid Waste Technical Conference, The Engineering Society of Detroit (ESD) Michigan Waste Industries Association (MWIA). East Lansing, MI. April 18-19.
- Liu, Z., Vanderberg, M., Liao, W., Liu, Y. 2015. An integrated process to clean up biogas, reclaim water and utilize solid residues – magnifying sustainability of anaerobic digestion. Oral presentation at the 2015 AICHE Annual International Meeting, Salt Lake City, UT. November 9-13.
- Sanyal, O., Liu, Z., Meharg, B., Liao, W., Lee, I. 2015. Evaluating the applicability of polyelectrolyte-based membranes to treating real wastewater effluents. Oral presentation at the 2015 AICHE Annual International Meeting, Salt Lake City, UT. November 9-13.
- Sanyal, O., Liu, Z., Meharg, B., Liao, W., Hong, J. S., Lee, I. 2015. Designing clay-polyeletrolyte based hybrid membranes for effluent treatment. Oral presentation at the 2015 AICHE Annual International Meeting, Salt Lake City, UT. November 9-13.
- Roman, M., Liao, W. 2015. Design of a Fresnel lens solar thermal collector for power generation. Oral presentation at the 2015 ASABE Annual International Meeting, New Orleans, LA. July 26-29.
- Liao, W., Chen, R., Roman, M., Liu, Z., Sanyal, O., Liu, Y., Lee. I. 2015. Integrating solar-bio-nano-technologies to develop a self-sustaining organic waste utilization system. Oral presentation at the 2015 ASABE Annual International Meeting, New Orleans, LA. July 26-29.
- Liu, Z., Liao, W., Liu. Y. 2015. Integrating electrocoagulation (EC) and biological routes to convert organic residues into value-added chemicals. Poster presentation at the 37th Symposium on Biotechnology for Fuels and Chemicals, Sand Diego, CA. April 27 – April 30.
- Liao, W. 2014. A self-sustaining solar-bio-nano-based concept to convert organic wastes into valuable products. Oral presentation at the 2014 Yangling International Agri-science Forum, Yangling, China. November 4-8.
- Chen, R., Murillo, M., Zhong, Y., Marsh, T., Uribe-Lorio, L., Uribe-Lorio, L., Kirk, D., Liao, W. 2014. Effects of climate region, reaction temperature and feed composition on microbial community and anaerobic digestion performance. Oral presentation at the 2014 ASABE Annual International Meeting, Montreal, Canada. July 13-17.
- Liao, W. 2013. A self-sustaining and scalable solar-bio-nano-based organic waste utilization concept. Oral presentation at the 13th Annual Conference on Renewable Energy from Organic Recycling, Columbus, OH. October 20-23.
- Zhong, Y., Bustanmante-Roman, M., Zhong, Y. K., Archer, S., Chen, R., Kirk, D., Liao, W. 2013. Using anaerobic digestion of organic wastes to biochemically store solar thermal

energy. Poster presentation at the 2013 ASABE Annual International Meeting, Kansas City, Missouri. July 21-24.

- Liu, Z. G., Stromberg, D., Liao, W., Liu, Y. 2013. Reclaiming water from anaerobic digestion effluent using electrocoagulation (EC) treatment – integration of EC and biogas purification. Oral presentation at the 2013 ASABE Annual International Meeting, Kansas City, Missouri. July 21-24.